UCLA
UCLA Electronic Theses and Dissertations

Title
Microstructural and Compositional Tunability in Sputter-Deposited Transition-Metal Carbide Thin Films using Ultra-Low Reactive Gas Pressures and 2D Layers

Permalink
https://escholarship.org/uc/item/0150r78b

Author
Tanaka, Koichi

Publication Date
2020

Peer reviewed|Thesis/dissertation

eScholarship.org Powered by the California Digital Library
University of California

UNIVERSITY OF CALIFORNIA

Los Angeles

Microstructural and Compositional Tunability in Sputter-Deposited Transition-Metal Carbide Thin Films using Ultra-Low Reactive Gas Pressures and 2D Layers

A dissertation submitted in partial satisfaction of the

requirements for the degree of Doctor of Philosophy

in Materials Science and Engineering

by

Koichi Tanaka

2020

© Copyright by

Koichi Tanaka

2020

ABSTRACT OF THE DISSERTATION

Microstructural and Compositional Tunability in Sputter-Deposited Transition-Metal Carbide Thin Films using Ultra-Low Reactive Gas Pressures and 2D Layers

by

Koichi Tanaka

Doctor of Philosophy in Materials Science and Engineering

University of California, Los Angeles, 2020

Professor Suneel Kodambaka, Chair

Tantalum carbides (Ta_2C, Ta_3C_2, Ta_4C_3, Ta_6C_5, and TaC) are refractory compounds with a mixture of covalent, ionic, and metallic bonding. Interest in these compounds stems from the fact that their structure and properties vary with their microstructure, composition, and orientation. In this dissertation, I investigated growth-related aspects of tantalum carbide (Ta-C) thin films grown on single-crystalline MgO(001) and Al_2O_3(0001) substrates via ultra-high vacuum direct current magnetron sputtering of a TaC compound target using pure Ar and Ar/C_2H_4 gas mixtures at substrate temperatures T_s between 1073 K and 1373 K. In particular, I focused on the effects of ultra-low pressures (p_c = 0.0025% ~ 2.5% of the total pressure) of C_2H_4 and the role of two-dimensional (2D) layers on compositional and microstructural evolution of Ta-C thin films.

I find that the Ta-C layers sputter-deposited on MgO(001) in pure Ar (i.e., $p_c = 0$) and Ar/C_2H_4 gas mixtures with $p_c = 5 \times 10^{-7}$ Torr are polycrystalline trigonal-structured α-Ta_2C (a = 0.310 nm and c = 0.492 nm). At $p_c = 5 \times 10^{-6}$ Torr, I obtain cubic rock salt (B1), 002-textured $TaC_{0.76}$ (a = 0.442 nm) porous thin film with facetted surface. Interestingly, I also observed 111-oriented twins due to four crystals rotated with respect to each other. Film grown at higher $p_c = 5 \times 10^{-4}$ Torr is relatively dense with smoother surface and composed of a two-phase mixture of nanocrystalline TaC and amorphous carbon.

Similar experiments carried out with $p_c = 0$ as a function of T_s resulted in 0001-oriented α-Ta_2C thin films on Al_2O_3(0001) at all T_s between 1073 K and 1373 K. With increasing T_s, I obtain smoother and thinner layers with enhanced out-of-plane coherency and decreasing unit cell volume. Interestingly, the Ta_2C 0001 texture improves with increasing T_s up to 1273 K above which the layers are relatively more polycrystalline. At T_s = 1373 K, during early stages of deposition, the Ta_2C layers grow heteroepitaxially on Al_2O_3(0001) with $(0001)_{Ta_2C} \parallel (0001)_{Al_2O_3}$ and $[10\bar{1}0]_{Ta_2C} \parallel [11\bar{2}0]_{Al_2O_3}$. With increasing deposition time t, I observed the formation of anti-phase domains and misoriented grains resulting in polycrystalline layers. I attribute the observed enhancement in 0001 texture to increased surface adatom mobilities and the development of polycrystallinity to reduced incorporation of C in the lattice with increasing T_s.

With the introduction of small amounts of ethylene (p_c = 0.1% to 1% of the total pressure), I obtain Ta-C layers with p_c-dependent composition and morphology. I find that the layers grown using lower p_c exhibit strongly facetted surfaces with columnar grains while those grown using higher p_c are rough with irregular features. Films deposited using higher p_c show primarily B1-TaC 111 reflections. At the lower T_s (= 1123 K) and lower p_c (= 5.0×10^{-6} Torr), I obtain a two-phase mixture of rhombohedral-Ta_3C_2(0001) and B1-TaC(111) oriented with

respect to the $Al_2O_3(0001)$ substrate as: $(111)_{TaC} \parallel (0001)_{Al_2O_3}$, $[\bar{2}11]_{TaC} \parallel [11\bar{2}0]_{Al_2O_3}$ and $(111)_{TaC} \parallel (0001)_{Al_2O_3}$, $[\bar{1}\bar{1}2]_{TaC} \parallel [11\bar{2}0]_{Al_2O_3}$ and $(0001)_{Ta_3C_2} \parallel (0001)_{Al_2O_3}$, $[10\bar{1}0]_{Ta_3C_2} \parallel [11\bar{2}0]_{Al_2O_3}$.

Finally, I investigated the effect of 2D hexagonal boron nitride (hBN) layer on the crystallinity of sputter-deposited $Ta_2C/Al_2O_3(0001)$ thin films. In these experiments, hBN is deposited via pyrolytic cracking of borazine at pressures $p_{borazine}$ up to 2.0×10^{-4} Torr, $T_s = 1373$ K for $t = 10$ min. I discovered that the Ta_2C film sputter-deposited on hBN-covered $Al_2O_3(0001)$ surface exhibits significantly higher crystallinity than the samples grown on bare $Al_2O_3(0001)$ substrates. Furthermore, I find that the crystallinity of thicker Ta_2C layers can be improved by inserting hBN layers at regular intervals.

My studies demonstrate compositional and microstructural tunability during sputter-deposition of transition-metal carbide thin films using small amounts of the reactive gas and 2D layered materials as buffer layers. I expect that these results open up the exciting possibility of growth of highly oriented cubic-TaC and/or layered-$Ta_{n+1}C_n$ phases, with n = 1, 2, 3, etc. with the appropriate choice of deposition parameters.

The dissertation of Koichi Tanaka is approved.

Xiaochun Li

Mark S. Goorsky

Jenn-Ming Yang

Suneel Kodambaka, Committee Chair

University of California, Los Angeles

2020

Dedicated to my grandfather Shigeo Takenaka

TABLE OF CONTENTS

ABSTRACT OF THE DISSERTATION ii

TABLE OF CONTENTS vii

LIST OF TABLE ix

LIST OF FIGURES x

ACKNOWLEDGEMENTS xiii

VITA xv

CHAPTER 1. Introduction 1
- Overview 1
- Brief summary of results 3

CHAPTER 2. Experimental Methods 6
- Sputter deposition of Ta-C thin films 6
- Chemical vapor deposition of hBN 9
- *In situ* Auger electron spectroscopy and low energy electron diffraction (AES/LEED) 9
- X-ray diffraction (XRD) 10
- Cross-sectional transmission electron microscopy (XTEM) 11
- Scanning electron microscopy (SEM) 11
- X-ray photoelectron spectroscopy (XPS) 12

CHAPTER 3. Effects of ultra-low ethylene partial pressure on microstructure and composition of reactively sputter-deposited Ta-C thin films 13
- Introduction 13
- Results and discussion 14
- Conclusion 21
- Figures 22

CHAPTER 4. Ultra-high vacuum dc magnetron sputter-deposition of 0001-textured trigonal α-$Ta_2C/Al_2O_3(0001)$ thin films 28
- Introduction 28

Results and discussion 29
Conclusion 36
Figures 37

CHAPTER 5. Ultrahigh vacuum dc magnetron sputter-deposition of [TaC(111) + $Ta_{n+1}C_n(000l)$]/Al_2O_3(0001) thin films 42
Introduction 42
Results and discussion 44
Conclusion 49
Table 51
Figures 52

CHAPTER 6. Van der Waals layer promoted heteroepitaxial growth of α-Ta_2C/Al_2O_3(0001) thin films 57
Introduction 57
Results and discussion 59
Conclusion 65
Figures 66

Summary and future work 69
Summary 69
Future work 71

References 73

LIST OF TABLE

Table 5.1: List of Ta-C structures, rocksalt (B1) TaC, trigonal α-Ta_2C,[76] rhombohedral Ta_3C_2,[8] and rhombohedral ζ-Ta_4C_3,[90] with in-plane and out-of-plane lattice parameters, a_o and c_o, respectively of bulk stoichiometric crystals. Third column shows the strongest intensity *hkil* and 000*l* reflections and the expected XRD peak positions (2Θ), calculated with the same λ (= 0.154056 nm) used in the experiments. Fourth column lists relative intensities (I_{hkil}) expected for those reflections in a powder XRD. Fifth column shows *c* values determined using experimentally-measured 2θ values (= 36.16^o and 76.89^o), assuming that they correspond to the 000*l* reflections. Sixth column lists percentage differences in *c* with respect to the bulk c_o values. 51

LIST OF FIGURES

Figure 3.1 Representative X-ray diffraction (XRD) 2θ-ω spectra obtained from Ta-C thin films sputter-deposited on MgO(001) at 1123 K using Ar/C_2H_4 gas mixtures with different C_2H_4 partial pressures, p_c. Solid circle in the spectra denotes 002 reflection of the single-crystalline MgO substrate. Dotted lines indicate the expected peak positions of stoichiometric B1-TaC and trigonal-Ta_2C phases. For comparison of the relative peak intensities across the samples, all the data within each of the spectra are normalized with respect to the MgO 002 reflection peak intensity in that spectrum. 22

Figure 3.2: (a and b) Typical cross-sectional transmission electron microscopy (XTEM) images acquired from the Ta_2C film sputter-deposited using pure Ar, i.e., $p_c = 0$. (b) Higher-resolution TEM (HRTEM) image of the region highlighted by a yellow square in (a). Inset is a Fourier transform (FT) of the image in (b). The spots within the FT are identified as reflections due to polycrystalline α-Ta_2C. 23

Figure 3.3: Characteristic XTEM images from the TaC_x layers sputter-deposited using $p_c = 5.0 \times 10^{-6}$ Torr, obtained along (a and b) [010] and (c and d) [011] zone axes. (b and d) HRTEM images of the regions highlighted by yellow squares in (a) and (c), respectively. Inset in (b) is a selected area electron diffraction pattern of the sample shown in (b). Arrows in (c) identify twin boundaries. Dotted lines in (d) highlight (100) and mirror (100)' planes in twinned crystals across a (111) plane shown by a dashed line with schematics of TaC lattice.[56] 24

Figure 3.4: XRD pole figures of (a) MgO 002, (b) MgO 111, (c) TaC 002, and (d) TaC 111 reflections obtained from the TaC_x film deposited using $p_c = 5.0 \times 10^{-6}$ Torr. (e and f) Simulated pole figures of (e) TaC 002 and (f) TaC 111 reflections from a hypothetical construct of multiply twinned 111-oriented TaC crystals rotated 90° with respect to each other. 25

Figure 3.5: (a and b) Characteristic XTEM images from the TaC_x layers sputter-deposited using $p_c = 5.0 \times 10^{-4}$ Torr. (b) HRTEM image of the area marked with yellow square in (a). Lattice fringes visible in the image are due to TaC crystallites (approximately 5 nm in size), three of which are highlighted by yellow lines. 26

Figure 3.6: X-ray photoelectron spectra (XPS) around C 1*s* and Ta 4*f* peaks obtained from the films sputter-deposited using p_c = (a) 0, (b) 5.0×10^{-6} Torr, and (c) 5.0×10^{-4} Torr. Open circles and squares are spectra acquired after Ar^+ etching of the sample for 600 and 1800 s, respectively. Solid lines are Gaussian fits to the raw data. Dashed line is background. Vertical dashed lines in C 1*s* spectra indicate binding energies characteristic of graphitic carbon and stoichiometric TaC, while those in Ta 4f correspond to Ta $4f_{5/2}$ and $4f_{7/2}$ of stoichiometric TaC. 27

Figure 4.1: (a) Representative 2θ-ω XRD scans, color coded for clarity, from $Ta_2C/Al_2O_3(0001)$ thin films sputter-deposited for times t = 30 min. at different T_s. Intensities in each of the curves are normalized to that of the Al_2O_3 00012 reflection and are plotted on a logarithmic scale. Labels **s** indicate the peaks due to Al_2O_3 000*l* reflections with l = 6, 9, and 12 at progressively increasing 2θ values. Unidentified peaks are assigned asterisks and are discussed in the text. (b) Plots of full width at half maxima, $\Gamma_{10\bar{1}1}$ (open circles) and Γ_{0002} (open squares) of $10\bar{1}1$ and 0002 reflection peaks respectively, and their relative intensity ratios [$I_{0002}/I_{10\bar{1}1}$ (filled triangles)] as a function of T_s. (c) Plots of ε_a (solid circles), ε_c (solid squares), and ε_V (open triangles) vs. T_s, where a (c) is the in-plane (out-of-plane) lattice parameter of α-Ta_2C, extracted from the XRD

scans in (a), V [= (332)$a2c$] is the unit cell volume, and $\varepsilon_i = [(i-i_o)/i_o]\times 100$, with $i = a$, c, and V. a_o (= 0.3103 nm), c_o (= 0.4938 nm), and V_o (= 0.1235 nm^3) correspond to bulk α-Ta_2C (P3m1).[76] 37

Figure 4.2: (top) XTEM and (bottom) high-angle annular dark field scanning TEM (HAADF STEM) images obtained from $Ta_2C/Al_2O_3(0001)$ films sputter-deposited for t = 30 min. at T_s = (a,d) 1073 K, (b,e) 1173 K, and (c,f) 1373 K. 38

Figure 4.3: (a) 2θ-ω XRD data obtained from $Ta_2C/Al_2O_3(0001)$ layers sputter-deposited at T_s = 1373 K for t = 3, 5, 10, and 30 min. are plotted on logarithmic scale with intensities in each of the curves normalized to that of the Al_2O_3 00012 reflections. (Please note that the time axis is not to scale.) Peaks due to α-Ta_2C reflections are labeled as shown. **s** refers to $Al_2O_3(0001)$ single-crystal substrate reflections 0006, 0009, and 00012. **h** indicates background scattering from the sample holder. (b, c) XRD pole figures of (b) Ta_2C $10\bar{1}1$ and (c) Al_2O_3 $11\bar{2}6$ reflections obtained from the sample deposited at 1373 K for t = 3 min. 39

Figure 4.4: (a) Representative XTEM image of the $Ta_2C/Al_2O_3(0001)$ film deposited at T_s = 1373 K for t = 5 min. (b and c) FTs of (b) yellow (Ta_2C) and (c) red (Al_2O_3) dotted square regions, respectively in (a). In (b) and (c), two of the film and substrate reflections are highlighted, respectively using cyan and purple circles, and ZA refers to zone axis. (d) HRTEM image of the green dotted square labeled **d** in (b). Arrow in (d) shows incoherency in layer stacking. 40

Figure 4.5: (a) Typical XTEM image of the $Ta_2C/Al_2O_3(0001)$ film deposited at T_s = 1373 K for t = 30 min. (b) HRTEM image with inset showing FT of the region bounded by a cyan dotted square labeled b in (a). (c - f) FTs of the (c) red, (d) green, (e) pink, and (f) yellow dotted square areas in (a). In the FTs, ZA refers to zone axis. 41

Figure 5.1: Typical SEM images obtained from Ta-C/$Al_2O_3(0001)$ thin films sputter-deposited for 2 h using 5 mTorr total Ar/C_2H_4 gas mixtures with: (a-d) $p_c = 5.0 \times 10^{-6}$ Torr at (a, b) T_s = 1273 K and (c, d) T_s = 1123 K and (e-h) with $p_c = 5.0 \times 10^{-5}$ Torr at (e, f) T_s = 1273 K and (g, h) T_s = 1123 K. 52

Figure 5.2: (a) Typical 2θ-ω XRD data, with intensities plotted on logarithmic scale, obtained from the same set of Ta-C/$Al_2O_3(0001)$ samples as in Fig. 5.1 grown at T_s = 1123 K and 1273 K with $p_c = 5.0 \times 10^{-5}$ Torr (blue and green curves) and 5.0×10^{-6} Torr (black and red curves). For direct comparison across the samples, intensities in each of the curves are normalized with respect to those of Al_2O_3 00012 reflections. Labels **s** indicate the peaks due to Al_2O_3 000l (l = 3, 6, 9, and 12) reflections. Peaks due to B1-TaC 111 and 222 reflections are labeled as shown. Peaks with asterisks are likely due to $Ta_{n+1}C_n$ 000l' reflections. XRD pole figures of (b) TaC 111, (c) $Ta_{n+1}C_n$ with 2θ = 38.08°, and (d) Al_2O_3 $11\bar{2}6$ reflections obtained from the Ta-C/$Al_2O_3(0001)$ layer sputter-deposited for 2 h with $p_c = 5.0 \times 10^{-6}$ Torr and T_s = 1123 K. 53

Figure 5.3: (a) Representative XTEM image obtained from Ta-C/$Al_2O_3(0001)$ film deposited at T_s = 1123 K and $p_c = 5.0 \times 10^{-6}$ Torr. (b) Higher magnification TEM images of regions bounded by white dotted square in (a). (c and d) FTs of the regions bounded by (c) yellow and (d) cyan dotted squares in (a), respectively. In the FT of (c), indices refer to B1-TaC with zone axis [110]. 54

Figure 5.4: (a) Representative XTEM image obtained from Ta-C/$Al_2O_3(0001)$ film deposited at T_s = 1273 K and $p_c = 5.0 \times 10^{-6}$ Torr. (b and c) Higher magnification TEM images of regions

bounded by dotted squares labeled b and c, respectively in (a). (d-f) HRTEM images of (d) black, (e) green, and (f) red dotted square regions in (b) and (c). White arrows in (f) highlight lamellar structures. Insets in (d-f) are FTs of the images (d), (e), and (f), respectively. In the FT of (f), yellow indices refer to B1-TaC with zone axis [110]. Pink and cyan arrows indicate orientations of the lamellar structures with respect to B1-TaC 111 and 111 reflections, respectively. 55

Figure 5.5: Schematics of Ta-C unit cells[56]: B1-TaC, trigonal α-Ta_2C (P3m1, a = 0.3103 nm, c = 0.4938 nm),[76] rhombohedral Ta_3C_2 (R3m, a = 0.314 nm, c = 2.245 nm),[8] and rhombohedral ζ-Ta_4C_3 (R3m, a = 0.3116 nm, c = 3.000 nm).[90] SF_C stands for stacking faults formed via removal of carbon layers. 56

Figure 6.1: (a) *In situ* Auger electron spectra (AES) obtained from a 'clean' $Al_2O_3(0001)$ substrate before (black curve) and after (red curve) exposure to 120000 L of borazine with pressure $p_{borazine} = 2.0 \times 10^{-4}$ Torr for t = 10 min. at T_s = 1373 K. Auger peaks due to boron (KVV), nitrogen (KVV), and oxygen (KVV) at 172, 381, and 503 eV, respectively, are labeled as B, N, and O. I do not detect Al in our system, which is observed at 66 eV. Corresponding low energy electron diffraction (LEED) patterns obtained *in situ* from (b) the bare $Al_2O_3(0001)$ and (c) after borazine exposure. Incident beam energy E_0 is set to 274 eV and 250 eV for (b) and (c), respectively. Reflections due to unreconstructed $Al_2O_3(0001)$-(1 × 1) and hBN(0001) are labeled as shown. 66

Figure 6.2: (a and b) *In situ* LEED patterns obtained from Ta_2C films sputter-deposited for t = 2 min. on (a) on hBN-covered and (b) bare $Al_2O_3(0001)$ substrates at T_s = 1373 K. Typical (c) bright field XTEM and (d) HAADF STEM images acquired from the same $Ta_2C/hBN/Al_2O_3(0001)$ sample as in (b). Inset in (c) is an FT of the cyan square region in (c). (e and f) 2θ-ω XRD scans obtained from (red curve) $Ta_2C/hBN/Al_2O_3(0001)$ and (black curve) $Ta_2C/Al_2O_3(0001)$ samples grown for t = (e) 2 min. and (f) 5 min. at T_s = 1373 K. Curve intensities are normalized with respect to those of Al_2O_3 0006 reflections and plotted on a logarithmic scale. Inset in (e) shows the same data in (e) plotted with intensities on linear scale. Inset in (f) shows higher-resolution 2θ-ω XRD scan of the $Ta_2C/hBN/Al_2O_3(0001)$ sample acquired with 0.5 mm size slits for 2θ and the detector, 0.05^o step size, and 20 s dwell time per step. Laue oscillations around Ta_2C 0002 reflection are visible in this plot. hBN layers for the t = 2 and 5 min. samples are grown with $p_{borazine} = 2.0 \times 10^{-4}$ Torr and 1.0×10^{-6} Torr, respectively for t = 10 min. at 1373 K. s indicates peaks due to Al_2O_3 000l reflections. The Ta_2C film reflections are labeled as shown. 67

Figure 6.3: (a) XRD 2θ-ω scans, with intensities normalized to that of the Al_2O_3 0006 reflection and plotted on a logarithmic scale, obtained from a (A, green curve) nanolaminate made of 6 Ta_2C/hBN bilayer stacks, (B, red curve) Ta_2C film grown continuously for t = 30 min., and (C, blue curve) Ta_2C film deposited with six 15 min. interruptions, during which the sample is annealed in Ar. All the samples are grown on hBN-covered $Al_2O_3(0001)$. In A and C, each of the 6 Ta_2C layers is sputter-deposited for t = 5 min., with the total time = 30 min., the same as in B. The interruption time in C is the same as the time taken to grow hBN layers in A. The hBN layers are grown with $p_{borazine} = 1.0 \times 10^{-6}$ Torr for t = 10 min. **s** denotes Al_2O_3 0006 and 00012 reflections. Asterisk indicates an unidentified peak, likely due to α-Ta_2C 0003 reflection. (b) Schematics of the A, B, and C. (c) XRD pole figure of Ta_2C $10\bar{1}1$ reflection obtained from A. 68

ACKNOWLEDGEMENTS

Here I would like to sincerely emphasize that this thesis could not have been done without extensive collaboration, support, advice, and encouragement from a number of individuals whom I have been fortunate to have met during my time as a PhD student at UCLA.

All of the works presented here are facilitated by my advisor Professor Suneel Kodambaka. I give my sincerest gratitude for giving me an opportunity to work in his group, for being a patient advisor, and for being supportive of my academic and career goals. I would also like to thank my thesis committee members: Professors Xiaochun Li, Mark S. Goorsky, and Jenn-Ming Yang, for taking their precious time to review this works. I would like to thank Ms. Lili Bulhoes and for her kind support throughout my Ph.D. life in MSE department.

I gratefully acknowledge that all the research projects presented here was supported by the Air Force Office of Scientific Research (AFOSR, Dr. Ali Sayir) under Grant # FA9550-14-1-0106 and # FA9550-18-1-0050. I would also like to thank the UCLA graduate division fellowships the Japan Student Service Organization (L16111111026) for the support. I acknowledge the use of instruments at the Electron Imaging Center for NanoMachines supported by NIH (1S10RR23057), the California NanoSystems Institute, and the Molecular Instrumentation Center at UCLA. I thank Mr. Noah Bodzin and the Nanoelectronics Research Facility in the UCLA Henry Samueli School of Engineering for assistance with focused ion beam milling. I am also thankful for Dr. Jian-Guo Zheng, Dr. Toshihiro Aoki, and Dr. Mingjie Xu at the Irvine Materials Research Institute (IMRI), part of the University of California Irvine, for their technical assistance with high-resolution scanning/transmission electron microscopy (S/TEM) analysis presented in Chapter 4 and 6.

I am grateful to my colleagues who have been always helpful, supportive, and encouraging throughout the years: Dr. Pedro Arias, Angel Aleman, Dr. Hicham Zaid, Aditya Deshpande. I thank Sidney Tran, Akshara Aditya, Jae Seung Hwang, Sean Hensarling, Yu-An Chung, Koki Hojo, Tomoyasu Watanabe, and Salma Irfan for all the insightful discussions and collaborations. I would like to thank my friends, with whom I survived through the hard course work and exams; Chao-Yueh Lo, Chris Yeung, Alex Fang, Linda Chitayapuntagul. I gratefully acknowledge Michael E. Liao, Dr. Chao Li, and Yekan Wang for their deep knowledge and practical skills on X-ray diffraction, which led me into a wonderful world of crystallography.

I would not have accomplished this work without support from my family and friends. I thank my father and mother for being supportive and patient living apart from their lovely grandkids for many years. I gratefully appreciate endless encouragement from Masako, Kanako, and Akiko. I thank David, Amber and Hannah, who saved me from the dilemma of parenting and academic work for many times.

Finally, I would like to express my sincerest gratitude to my beloved family, Natsuko, Sana, and Ray, for understanding my challenge, for joining the long journey, and most importantly, for enjoying this mess. We are right off to the next one.

VITA

EDUCATION

Tokyo Institute of Technology 2006 - 2008
Master of Engineering

Tokyo Institute of Technology 2002 - 2006
Bachelor of Engineering

RESEARCH AND PROFESSIONAL EXPERIENCE

Graduate Student Researcher 2016 - 2020
Kodambaka *In Situ* Mircroscoby Lab at UCLA, Los Angeles, CA, USA

Affiliate Researcher 2014 - 2015
Plasma Applications Group at Lawrence Berkeley National Laboratory, Berkeley, CA, USA

Research Scientist 2008 - 2016
Mitsubishi Materials Corporation Central Research Institute, Ibaraki, Japan

PUBLICATIONS/MANUSCRIPTS

1. **K. Tanaka**, A. Aleman, M. E. Liao, Y. Wang, M. S. Goorsky, S. Kodambaka, "Effects of ultra-low ethylene partial pressure on microstructure and composition of reactively sputter-deposited Ta-C thin films", *Thin Solid Films*, 688, 137440 (2019)
2. **K. Tanaka**, J. Fankhauser, H. Zaid, M. Sato, D. Yu, A. Aleman, A. Ebnonnasir, M. Kobashi, C. Li, M. S. Goorsky, S. Kodambaka, "Kinetics of Zr-Al intermetallic compound formation during ultra-high vacuum magnetron sputter-deposition of Zr/Al2O3(0001) thin films", *Acta Materialia*, 152, 34-40 (2018)
3. **K. Tanaka**, A. Anders, "Temporal evolution of ion energy distribution functions and ion charge states of Cr and Cr-Al pulsed arc plasmas", *J. Vac. Sci. Technol. A*, 33 [6], 061301 (2015)
4. **K. Tanaka**, L. Han, X. Zhou, A. Anders, "Adding high time resolution to charge-state-specific ion energy measurements for pulsed copper vacuum arc plasmas" *Plasma Sources Sci. and Technol.*, 24 [4], 045010 (2015)
5. **K. Tanaka**, A. Aleman, H. Zaid, M. E. Liao, K. Hojo, Y. Wang, M. S. Goorsky, S. Kodambaka, "Ultra-high vacuum dc magnetron sputter-deposition of 0001-textured trigonal α-Ta_2C/Al_2O_3(0001) thin films" (*Manuscript*)
6. **K. Tanaka**, M. E. Liao, A. Aleman, H. Zaid, M. S. Goorsky, S. Kodambaka "Ultrahigh vacuum dc magnetron sputter-deposition of [TaC(111) + $Ta_{n+1}C_n$(000l)]/Al_2O_3(0001) thin films" (*Manuscript*)

7. **K. Tanaka**, P. Arias, K. Hojo, M. E. Liao, T. Aoki, T. Watanabe, A. Aleman, H. Zaid, M. S. Goorsky, S. Kodambaka "Van der Waals layer promoted growth of highly crystalline and oriented thin films on single crystal Al_2O_3(0001) via direct current magnetron sputter-deposition" (*Manuscript*)

SELECTED CONFERENCE PRESENTATIONS

1. **K. Tanaka**, K. Hojo, A. Deshpande, P. Arias, A. Aleman, H. Zaid, M. E. Liao, M. S. Goorsky, S. Kodambaka, "Van der Waals Promoted Heteroepitaxy in Sputter-deposited Transition Metal Carbide and Sulfide Thin Films", ***American Vacuum Society 66th Annual Symposium and Exhibition*** (2019), Columbus, Ohio, USA
2. **K. Tanaka**, J. Fankhauser M. Sato, D. Yu, A. Aleman, A. Ebnonnasir, M. Kobashi, C. Li, M. S. Goorsky, S. Kodambaka, "Temperature-dependent Interfacial Layer Formation during Sputter-deposition of Zr Thin Films on Al_2O_3(0001)", ***44th International Conference on Metallurgical Coatings and Thin Films*** (2017), San Diego, California, USA

SEMINAR TALK

"**Van der Waals layer promoted heteroepitaxy in reactively sputter-deposited thin films**", *Japan Advanced Institute of Science and Technology*, Kanazawa, Japan (June 25, 2019)

AWARDS/FELLOWSHIPS

1. **National Student Award: *Dorothy M. and Earl S. Hoffman Scholarship***

   66th Annual Symposium of American Vacuum Society (2019), Ohio, United States
2. **Best Student Presentation Award**

   7th International Symposium on Organic and Inorganic Electronic Materials and Related Nanotechnologies (2019), Nagano, Japan
3. **Poster Award**

   15th International Symposium on Sputtering and Plasma Processes (2019), Kanazawa, Japan
4. **Dissertation Year Fellowship** (University of California, Los Angeles) 2019 - 2020
5. **Graduate Division Award** (University of California, Los Angeles) 2016 - 2019

CHAPTER 1. Introduction

Overview

Transition-metal carbides (TMCs) possess good thermomechanical properties, owing to a combination of strong ionic, covalent, and metallic bonds, along with good resistance to ablation, corrosion, and wear.[1, 2] TMCs are also known to be ductile at elevated temperatures T, typically above $0.5T_m$,[3] where T_m is the melting point in K. TMCs are attractive for applications in cutting tools, as wear- and oxidation-resistant coatings, as structural components in hypersonic vehicles, as electrical conductors, as optical thin films,[4] and potentially of interest in micro and nano electromechanical systems (MEMS and NEMS) used in harsh environments, e.g. for thermal sensing at $T > 1000$ K,[5, 6] in aerospace industry, in gas and oil drilling sites, and in nuclear fusion reactors. In these MEMS and NEMS applications, the use of submicrometer- or nanometer-thick TMC films are desirable since they can potentially increase the operation temperature of the devices. Therefore, growth of TMCs as thin films with desired composition, microstructure, and hence properties is important.

Among the TMCs, tantalum carbides (Ta_2C, Ta_3C_2, Ta_4C_3, Ta_6C_5, and TaC)[7, 8] are refractory compounds whose structure and properties vary with carbon concentration. The rocksalt (B1) structured TaC_x is stable over a wide phase field, $0.74 \leq x \leq 1$ at temperatures up to 2123 K,[9] with composition-dependent thermomechanical, thermal, and electrical properties.[9] Functionalized layered carbides of the form $Ta_{n+1}C_n$ are part of the "MXene" family[10] with interesting properties and potentially new applications.[10-13] Among the Ta-C compounds, B1-TaC and trigonal-structured α-Ta_2C exhibit the highest $T_m \sim 4250$ K and 3600 K, respectively,[7] with exceptional mechanical properties of interest in aerospace structures, cutting tools, and wear-resistant coatings.[1, 14] In addition to structural applications, TaC is a promising candidate as an

Ohmic contact in high-temperature electronics[15] and as a catalyst in fuel cells.[16] Previous studies have shown localized plastic deformation during microindentation of TaC single-crystals at temperatures as low as 77 K.[9] More recent nanomechanical tests conducted on refractory carbides[4, 17-19] suggest the possibility of enhanced room-temperature ductility and potentially superior toughness at smaller length scales as in thin films. Ta-C thin films have been grown using a variety of methods, including but not limited to evaporation,[20] pulsed laser ablation,[21] chemical vapor deposition,[22] and magnetron sputter deposition,[14, 21, 23] with the latter being the most commonly employed approach in the hard coatings community.

Two-dimensional (2D) layered materials, such as graphene, hexagonal boron nitride (hBN), MXenes, and transition-metal dichalcogenides (TMDCs), have attracted considerable attention for a variety of applications, primarily in nanoelectronics and optoelectronics. An exciting but relatively little explored application of 2D layers is their use as templates for crystal growth. It is generally assumed, and often true, that homoepitaxy yields higher crystalline quality thin films than heteroepitaxy. Studies[24, 25] conducted nearly three decades ago have shown that layered materials, owing to weak van der Waals (vdW) bonding across the layers, can aid in heteroepitaxial growth of layered as well as non-layered materials. For example, Ohuchi *et al.*[24] demonstrated that deposition of a vdW layered material ($NbSe_2$) onto another vdW material (MoS_2) results in heteroepitaxial growth without lattice strain despite the large mismatch of 9%. In the recent years, 2D layered materials have been shown to promote 'remote epitaxy', where the 2D layer present at the substrate-film interface does not hinder the epitaxial registry between the film and the substrate.[26-28] This unique feature of 2D materials can aid the crystal growth of sputter-deposited films by decoupling the deposited species from the substrate surface thus enhancing surface mass transport.

In this dissertation, I aim to develop methods to grow highly crystalline and highly oriented Ta-C thin films through fundamental understanding of the factors influencing the morphology, composition, and microstructure of Ta-Cs deposited via ultra-high vacuum direct current (dc) magnetron sputtering. Through a systematic investigation of the effects of the deposition parameters, I identified the role of ultra-low reactive gas pressure and 2D layered materials on the composition and crystallinity of Ta-C films. In Chapter 2, I present all the experimental details related to sputter-deposition, chemical vapor deposition of hBN, and characterization of thin films. Chapters 3-6 contain details of my experimental results, analysis, and discussion. Each chapter contains an introduction section in which I provide the literature background and motivation pertaining to the experiments described in the results and discussion sections.

Brief summary of results

In Chapter 3, I present results from growth and characterization of Ta-C thin films sputter-deposited using a TaC target in 20 mTorr Ar/C_2H_4 gas mixtures as a function of C_2H_4 partial pressures (5.0×10^{-7} Torr $\leq p_c \leq 5.0 \times 10^{-4}$ Torr) at 1123 K. This work is published in *Thin Solid Films*, **688**, 137440 (2019). Using a combination of X-ray diffraction (XRD), X-ray photoelectron spectroscopy (XPS), and transmission electron microscopy (TEM) equipped with X-ray energy dispersive spectroscopy (EDS), I determined the crystallinity, composition, and microstructure of the as-deposited samples. I find that sputter-deposition in pure Ar atmosphere results in α-Ta_2C layers. Introducing small amounts of C_2H_4 ($p_c = 5.0 \times 10^{-6}$ Torr, 0.025% of total pressure) during sputter-deposition results in single-phase, substoichiometric $TaC_{0.76}$ films. With $p_c \geq 5.0 \times 10^{-5}$ Torr, two-phase TaC + C nanocomposites are obtained. The results suggest

that the Ta-C composition and structure are highly sensitive to ethylene pressure during sputter-deposition using compound TaC target.

In Chapter 4, I report on the deposition temperature and time dependent evolution of microstructure of α-Ta_2C thin films sputter-deposited in pure Ar (i.e., p_c = 0) on single-crystalline $Al_2O_3(0001)$ substrates. XRD and TEM characterization of the as-deposited layers reveal the growth of α-Ta_2C thin films with 0002 preferred orientation at all T_s. I find that both crystallinity and surface smoothness of the films improve monotonically with increasing T_s. However, I observe enhancement in 0002 texture with increasing T_s up to 1273 K, after which the layers are relatively more polycrystalline. Ta_2C layers deposited at the highest T_s (= 1373 K) begin to grow heteroepitaxially on $Al_2O_3(0001)$ with the following crystallographic relationship $(0001)_{Ta_2C} \parallel (0001)_{Al_2O_3}$ and $[10\bar{1}0]_{Ta_2C} \parallel [11\bar{2}0]_{Al_2O_3}$ and transition to polycrystalline growth with increasing deposition time.

In Chapter 5, I present the effects of small amounts of C_2H_4 (p_c = 0.1 to 1% of total pressure) on the composition and microstructure of Ta-C thin films grown on $Al_2O_3(0001)$. XRD, scanning electron microscopy (SEM), and TEM characterizations are carried out to reveal the phase, orientation, and microstructure of the as-deposited TaC_x films. I find that the layers grown using lower p_c exhibit strongly facetted surfaces with columnar grains while those grown using higher p_c are rough with irregular features. Films deposited using higher p_c show primarily B1-TaC 111 reflections. At the lower T_s (= 1123 K) and lower p_c (= 5.0×10^{-6} Torr), I obtain a two-phase mixture of rhombohedral-$Ta_3C_2(0001)$ and B1-TaC(111) oriented with respect to the $Al_2O_3(0001)$ substrate as: $(111)_{TaC} \parallel (0001)_{Al_2O_3}$, $[\bar{2}11]_{TaC} \parallel [11\bar{2}0]_{Al_2O_3}$ and

$(111)_{TaC} \parallel (0001)_{Al_2O_3}$, $[\bar{1}\bar{1}2]_{TaC} \parallel [11\bar{2}0]_{Al_2O_3}$ and $(0001)_{Ta_3C_2} \parallel (0001)_{Al_2O_3}$, $[10\bar{1}0]_{Ta_3C_2} \parallel [11\bar{2}0]_{Al_2O_3}$.

In Chapter 6, I demonstrate the improvement of crystallinity and orientation of sputter-deposited Ta_2C thin films grown on $Al_2O_3(0001)$ using 2D hBN layers. The hBN layers are deposited via pyrolytic cracking of borazine. Using a combination of *in situ* Auger electron spectroscopy (AES) and low energy electron diffraction (LEED) techniques, I characterized the hBN layer. I find that the Ta_2C films deposited on hBN-covered $Al_2O_3(0001)$ surfaces exhibit significantly higher crystallinity than the samples grown on bare $Al_2O_3(0001)$ substrates. I discovered that inserting hBN layers at regular intervals improves the crystallinity of thicker Ta_2C layers, suggesting that the deposition on 2D layer yields better crystals than on bare Ta_2C surfaces.

CHAPTER 2. Experimental Methods

Sputter deposition of Ta-C thin films

Deposition system: All of my deposition experiments are carried out in a load-locked ultra-high vacuum (UHV) deposition system (base pressure < 7×10^{-10} Torr, as measured by an ion gauge with emission current set to 1 mA) equipped with a 2" (50.8 mm) diameter magnetron (from Kurt J. Lesker) for sputter-deposition, multiple gas inlets for reactive sputter-deposition and chemical vapor deposition (CVD), and low-energy electron diffraction/Auger electron spectroscopy (LEED/AES) system for *in situ* characterization of the sample surfaces.[29, 30] The chamber is evacuated using a combination of a 685 l/s turbomolecular pump and a mechanical rotary pump. For the experiments carried out in this dissertation, the typical base pressure in the deposition chamber prior to loading the samples is < 2×10^{-9} Torr.

Substrate preparation: All the Ta-C samples are grown on single-side polished, $5 \times 10 \times 0.5$ mm^3 MgO(001) or ~$2 \times 10 \times 0.5$ mm^3 Al_2O_3(0001) rectangular strips. The MgO(001) and Al_2O_3(0001) substrates are first cut from $10 \times 10 \times 0.5$ mm^3 MgO(001) (MGa101005S1 from MTI Corp.) and Al_2O_3(0001) (ACL101005S1 MTI Corp.) single-crystals, respectively. They are cleaned sequentially via sonication in acetone, isopropyl alcohol, and deionized water, blown dry with compressed nitrogen. The substrates are oven-baked in air at 473 K for 45 min. Then the samples are mounted on a 0.05-mm-thick Mo foil covered heating stage made of pyrolytic boron nitride with a $5 \times 15 \times 0.15$ mm^3 carbon nanotube tape as the heating element. (The Mo foil serves as a reference for measuring substrate temperatures T_s before deposition.) Typical resistance of the tape is 2 ~ 3 Ω. The stage is capable of resistively heating substrates to T_s up to 1673 K. The sample-heater assembly is introduced into the load-lock chamber and held until the chamber pressure is reduced to < 8×10^{-8} Torr using a 50 l/s turbo molecular pump. Then the

sample holder is transferred into the UHV deposition chamber and thermally degassed at $T_s = T_d$ until the base pressure is below 6×10^{-9} Torr with the sample at T_d. T_d is set to 1123 K for MgO(001) substrates (Chapter 3), and 1373 K (Chapters 4 and 6) or 1273 K (Chapter 5) for Al_2O_3(0001) substrates. T_s is measured using a pyrometer (IMPAK IS 8-GS) placed outside the deposition chamber approximately 0.4 m away from the substrate. The pyrometer emissivity is set to 0.15 ± 0.02, the emissivity of Mo, and the associated measurement uncertainty is ± 20 K. At the desired T_s = 1123 K, I measure spatial variations in T_s between 1106 K and 1143 K along the length of the substrates. After degassing, the substrate surface structure is determined *in situ* using LEED at room temperature. LEED patterns reveal spots characteristic of clean and unreconstructed MgO(001)-(1×1) and Al_2O_3(0001)-(1×1) surfaces.

DC magnetron sputtering: All the Ta-C films are deposited by direct current (dc) magnetron sputtering of a 2" (50.8 mm) diameter and 0.125" (3.18 mm) thick TaC compound target (99.5 wt.% purity, from Plasmaterials, Inc.). First, C_2H_4 gas (99.999%, Matheson) is introduced via a UHV leak valve and the ethylene pressure p_c adjusted to the desired value. Then, Ar gas (99.999%, Airgas Co.) is let in and the total pressure adjusted to 5×10^{-3} Torr (Chapter 5) and 2×10^{-2} Torr (Chapters 3, 4, and 6), as measured by a convection gauge. The sputtering power is set to 50 W. The target is pre-sputtered for 30 s ~ 2 min. with the substrate turned out of sight from the target. After pre-sputtering, the substrate is rotated to be in the line of sight with the target and the film deposited for desired deposition times t between 2 and 120 min. After deposition, the gases are shut off immediately and the samples cooled passively to room temperature in UHV.

For the results presented in Chapter 3, Ta-C films are grown using $p_c = 0$, 5.0×10^{-7}, 5.0×10^{-6}, 5.0×10^{-5}, and 5.0×10^{-4} Torr with total pressure set to 2.0×10^{-2} Torr for t = 30 min. The

target is pre-sputtered for 2 min. Using these deposition parameters, I measure output current of 0.15 A during sputtering at all p_c, while the target voltage varies with p_c from 309 V at $p_c = 0$ to 307 V at 5.0×10^{-7} Torr and 5.0×10^{-6} Torr, 309 V at 5.0×10^{-5} Torr, and 315 V at 5.0×10^{-4} Torr. The deposition rate in these experiments is between 0.08 nm/s and 0.11 nm/s.

For the results presented in Chapter 4, Ta-C films are sputter-deposited in pure 2.0×10^{-2} Torr Ar (99.999%, Airgas Co.) at T_s = 1073 K, 1173 K, 1223 K, 1273 K, and 1373 K. The layers are deposited for t = 3, 10, and 30 min. (The deposition rate, as I show later, depends on the T_s and is between 0.04 and 0.05 nm/s.) Prior to deposition, the target is pre-sputtered for 2 min. for all the samples except the t = 3 min. sample, for which the pre-sputter time is set to 1 min. The discharge current and voltage during sputter-deposition are 0.16 A and 297~302 V, respectively for all but the t = 3 min. samples deposited at T_s = 1373 K, for which I observe 0.18 A and 268 V.

For the results presented in Chapter 5, Ta-C films are grown using 5.0×10^{-3} Torr Ar/C_2H_4 gas mixtures with $p_c = 5.0 \times 10^{-6}$ Torr and 5.0×10^{-5} Torr, T_s = 1123 K and 1273 K, and t = 2 h. For these samples, the pre-sputter time is set to 30 s. The discharge current and voltage during sputter-deposition are 0.15~0.16 A and 297~307 V, respectively. The deposition rate at $p_c = 5.0 \times 10^{-6}$ Torr is approximately 0.03 nm/s.

For the results presented in Chapter 6, Ta-C films are sputter-deposited in pure 2.0×10^{-2} Torr Ar at T_s = 1373 K and the layers are deposited for t = 2, 5, 10, and 30 min. Prior to deposition, the target is pre-sputtered for 1 min. for all the samples except the t = 5 min. sample, for which the pre-sputter time is set to 2 min. The discharge current and voltage during sputter-deposition are 0.16 A and 295~298 V, respectively, for all but the t = 5 min. samples, for which I measure 0.17 A and 276~277 V.

Chemical vapor deposition of hBN

The chemical vapor deposition (CVD) of hBN on bare Al_2O_3(0001) and sputter-deposited Ta_2C surfaces is carried out using purified borazine vapor supplied through a UHV leak valve connected to a 20 ml UHV-compatible domed glass tube (Accu-Glass Products, Inc) filled with ~ 5 ml of liquid borazine (from Gelest, Inc.). Prior to hBN deposition, the liquid borazine is purified using a freeze-pump-thaw cycle following the procedure described in Refs. 31-33. Briefly, during a typical freeze-pump-thaw cycle, the borazine is first frozen by submerging the glass tube in a reservoir containing liquid N_2 ($T_{boiling}$ = 77 K). Next, with the borazine kept frozen, the bottle is evacuated with the aid of a 50 l/s turbomolecular pump for 5 min. to remove molecular hydrogen and other residual gases with boiling point below 77 K present in the glass tube. Finally, the liquid N_2 reservoir is removed and the borazine in the tube is allowed to passively thaw. The sample is heated in UHV to T_s = 1373 K and the purified borazine is introduced into the deposition chamber and borazine pressure $p_{borazine}$ adjusted to a desired value $p_{borazine} = 1.0 \times 10^{-6}$ Torr ~ 2.0×10^{-4} Torr (as measured with an ion gauge), and the borazine pressure is maintained for t = 5 ~ 10 min.

***In situ* Auger electron spectroscopy and low energy electron diffraction (AES/LEED)**

Surface composition and structure of the samples, including bare MgO(001) and Al_2O_3(0001) substrates, hBN-covered Al_2O_3(0001), and sputter-deposited Ta_2C, are determined *in situ* after each deposition step using a UHV-compatible, reverse-view, AES/LEED system with four-grid optics.[29, 34] The Auger electron spectra are acquired in derivative mode using a 1.5 keV primary beam up to 50 μA and at kinetic energies between 20 and 700 eV with a step size of 1 eV and a dwell time of 1 s. LEED patterns are obtained at incident electron energies between 200 and 250 eV with up to 2 μA beam current using a screen voltage of 4 kV.

X-ray diffraction (XRD)

XRD 2θ-ω and pole figure measurements are carried out using a Bede D1 high-resolution diffractometer with monochromatic Cu $K_{\alpha 1}$ radiation (wavelength λ is 0.154056 nm) and a Bede D1 rotary stage diffractometer with non-monochromatic Cu X-rays, respectively, following the procedures described in Refs. 30, 34, 35. First, the samples are mounted on a miscut Si(100) wafer to eliminate background signal from the diffractometer stage. The optics of the detector and X-ray incident beam are calibrated to achieve maximum straight-through intensity. For detector slits, I used 2-mm-wide slits (angular aperture $\delta_{2\theta} = 0.382^{o}$) for all 2θ-ω scans except for the data shown in inset Fig. 6.2(b), for which 0.5-mm-side slits ($\delta_{2\theta} = 0.096^{o}$) are used. For all pole figure measurements, a Soller slit is used.

For the data presented in Chapter 3, the position and inclination of the Ta-C/MgO(001) samples are calibrated with respect to ω and χ (out-of-plane rotation perpendicular to ω) of the MgO 002 reflection, 2θ = 42.94^{o}.[36] 2θ-ω scans for 2θ values between 20° and 100° are acquired with a step size of 0.02^{o} and a dwell time of 1 s. XRD pole figures of MgO 111, MgO 002, TaC 111, and TaC 002 reflections are obtained with 2θ fixed at 36.96^{o}, 42.94^{o}, 34.87^{o}, and 40.49^{o}, respectively. These 2θ values are calculated using lattice constants of stoichiometric B1-structured MgO and TaC.[37, 38] The intensities of each reflection are measured along χ between 0° and 90° with a step size of 2.0^{o} and φ (in-plane rotation angle) between 0° to 360° with a step size of 1.0^{o}. The dwell time is 0.4 s per step.

The inclination of the Ta-C/Al_2O_3(0001) samples are calibrated with respect to ω and χ of Al_2O_3 0006 reflection at 2θ = 41.68^{o} (JCPDS-ICDD No. 46-1212). 2θ-ω scans are obtained for 2θ values between 20° and 100° with a step size of 0.02^{o} and a dwell time of 1 s. XRD pole figures of Al_2O_3 $11\bar{2}6$, Ta_2C $10\bar{1}1$, and TaC 111 reflections are acquired with 2θ fixed at 57.50^{o},

38.08^o, and 34.84^o, respectively, and the desired reflection peak intensities measured along χ between 0° and 90° with a step size of 2.0^o and φ between 0° and 360° with a step size of 1.0^o. The dwell time is 1 s (Chapters 4 and 6) and 0.5 s (Chapter 5) per step for these measurements.

Cross-sectional transmission electron microscopy (XTEM)

Cross-sectional transmission electron microscopy (XTEM) characterization is carried out on electron-transparent specimens prepared via focused ion beam (FIB) milling of the Ta-C thin films with 30 keV Ga^+ ions in an FEI Nova NanoLab™ 600 DualBeam FIB scanning electron microscope (FIB/SEM) system. Prior to milling, the film surface is protected by electron-beam-assisted deposition of ~100-nm-thick layer of platinum (Pt) from trimethyl platinum ($C_9H_{16}Pt$) using 30 kV and 0.1 nA electron beams. Although the deposition of Pt layer helps minimize Ga^+ implantation during milling, it results in unintentional deposition of carbon from the precursor.[39, 40] XTEM images of the films and the film/substrate interfaces are acquired using an FEI Titan scanning TEM (S/TEM) (Chapters 3-6), a JEOL JEM-2800 TEM (S/TEM) (Chapter 4), and a JEOL JEM-ARM300F S/TEM (Chapter 6), operated at 300 kV, 200 kV, and 300 kV, respectively. Prior to loading the TEM samples into JEOL JEM-ARM300F, they are etched using Fischione's Model 1040 NanoMill®.

Scanning electron microscopy (SEM)

Scanning electron microscopy (SEM) characterization of the Ta-C/Al_2O_3(0001) film morphologies is carried out using an FEI Nova NanoLab™ 600 DualBeam FIB scanning electron microscope (FIB/SEM) system with an acceleration voltage of 10 kV and a working distance of 5 mm.

X-ray photoelectron spectroscopy (XPS)

XPS data are collected from air-exposed and surface-etched samples using Kratos Analytical AXIS Ultra DLD. The sample surfaces are etched as a means to minimize contribution of surface-adsorbed carbon, an unintentional consequence of air-exposure, to the total amount of carbon detected using XPS. Etching is carried out using 3.8 keV Ar^+ ion beams (with Ar gas pressure at 3×10^{-7} Torr) rastered across 1.7×1.7 mm^2 using an extractor current of 100 μA. (With these parameters, I measure an etch rate of ~ 0.02 nm/s for $Ta_2C/Al_2O_3(0001)$ thin films sputter-deposited using p_c = 0 Torr. I assume that the etch rates are similar in all our TaC_x/MgO(001) samples deposited using different P_c.) After every 600 s of etching, XPS data are obtained and checked for physisorbed hydrocarbons and adventitious carbon, expected around 260 eV and 284.4 eV, respectively. Any peaks due to hydrocarbons after the first 600 s of etching is not observed, based on which I assume that any C 1*s* signals detected in the spectra are due to carbon incorporated in the film during deposition. And the etch-XPS cycles are repeated until the appearance of the Mg and O peaks, indicative of near-complete removal of the Ta-C film. Higher resolution C 1*s* and Ta 4*f* spectra are acquired with a step size of 0.1 eV and dwell time of 1 s per step. The binding energies in each of the spectra are calibrated with O 1*s* peak set to 530.60 eV.

CHAPTER 3. Effects of ultra-low ethylene partial pressure on microstructure and composition of reactively sputter-deposited Ta-C thin films

Introduction

TaC_x thin films have been grown using a variety of methods, including but not limited to evaporation,[20] pulsed laser ablation,[21] chemical vapor deposition,[22] and magnetron sputter deposition,[14, 21, 23] with the latter being the most commonly employed approach in the hard coatings community. In the literature, only a few reported heteroepitaxial growth of 001- and 111-oriented TaC thin films, via electron-beam evaporation[20] and pulsed laser deposition,[15] respectively, on single-crystalline MgO(001) and SiC(0001) substrates. Relatively more number of studies exist on dc magnetron or radio-frequency sputter-deposition of polycrystalline TaC_x thin films.[14, 15, 21, 23, 41, 42] Hakansson *et al.*[14] carried out reactive sputtering of elemental Ta target in Ar/CH_4 and Xe/CH_4 gas mixtures with CH_4 partial pressures between 0.3 and 1.8 mTorr (i.e., 10 to 60% of the total pressure) and reported the growth of polycrystalline B1-TaC_x films on high speed steel substrates. Evans *et al.*[42] varied C_2H_4 gas flow rates during reactive sputtering of Ta on Si(001) in Ar/C_2H_4 gas mixtures and observed the growth of nanocomposite films with TaC and amorphous hydrogenated carbon phases. Nilsson *et al.*[43] reported the formation of B1-TaC in carbon films with 12 to 36 at.% Ta grown on Si(111) via co-sputtering of pure C and Ta targets. Lasfargues *et al.*[44] investigated the effects of substrate bias and temperature T_s on the phase composition of Ta-C films deposited on Si(001) via sputtering of a nearly stoichiometric TaC target in Ar gas discharge and found that the phase fraction of TaC vs. Ta_2C increased with increasing bias voltage. All these reports indicate that the Ta-C film composition depends on the sputter-deposition parameters. Here, I focus on understanding the influence of ultra-low (0.0025 to 2.5% of total pressure) amounts of ethylene (C_2H_4) on compositional and microstructural evolution of sputter-deposited Ta-C thin films.

In this chapter, I present results from growth and characterization of Ta-C thin films sputter-deposited using a TaC target in 20 mTorr Ar/C_2H_4 gas mixtures as a function of C_2H_4 partial pressures ($5.0 \times 10^{-7} \leq p_c \leq 5.0 \times 10^{-4}$ Torr) at 1123 K. Using a combination of XRD, XPS, and TEM equipped with X-ray energy dispersive spectroscopy (EDS), I determined the crystallinity, composition, and microstructure of the as-deposited samples. I find that sputter-deposition in pure Ar atmosphere results in trigonal-structured Ta_2C layers. Introducing small amounts of C_2H_4 ($p_c = 5.0 \times 10^{-6}$ Torr, 0.025% of total pressure) during sputter-deposition results in single-phase, substoichiometric $TaC_{0.76}$ films. With $p_c \geq 5.0 \times 10^{-5}$ Torr, we obtain two-phase TaC + C nanocomposites. My results suggest that the Ta-C composition and structure are highly sensitive to ethylene pressure during sputter-deposition using compound TaC target.

Results and discussion

Figure 3.1 shows typical 2θ-ω XRD scans obtained from Ta-C/MgO(001) thin films sputter-deposited at T_s = 1123 K using 20 mTorr pure Ar (i.e., $p_c = 0$) and Ar/C_2H_4 gas mixtures with P_c increased in ten-fold increments from 5.0×10^{-7} Torr to 5.0×10^{-4} Torr. In the plot, the highest intensity peaks at 2θ = 42.94° are due to 002 reflections of the MgO single-crystal substrate. In the 2θ-ω data from the Ta-C sample deposited with $p_c = 0$, we find higher intensity film peaks at 2θ = 36.48° and 38.14°, which I identify as 0002 and $10\bar{1}1$ reflections, respectively of trigonal α-Ta_2C ($P\bar{3}m1$).[9] From these 2θ values, I determine the in-plane *a* and out-of-plane *c* lattice constants as *a* = 0.310 nm and *c* = 0.492 nm. The measured *a* value is, within the experimental uncertainties, the same as that (0.3103 nm) reported for the bulk Ta_2C, while *c* is slightly smaller (~ 0.2%) than the corresponding bulk value (0.4938 nm).[9] The XRD data from the sample grown using $p_c = 5.0 \times 10^{-7}$ Torr also reveals peaks corresponding to α-Ta_2C. From the measured 2θ values, I determine lattice constants *a* = 0.311 nm and *c* = 0.493 nm. Both *a* and

c are ~ 0.2% larger than those measured from the XRD data of Ta_2C film deposited in pure Ar (p_c = 0). I attribute the ~0.85% volume increase in the Ta_2C crystal lattice to increased incorporation of carbon, presumably as interstitials.

The XRD data from the samples deposited using higher $p_c \geq 5.0 \times 10^{-6}$ Torr reveal peaks at 2θ values around 35° and 41°, different from those observed in Ta_2C films grown at lower p_c. I identify these peaks as the reflections in polycrystalline B1-TaC.[45] For the TaC films grown with $p_c = 5.0 \times 10^{-6}$ Torr, we find two higher intensity peaks due to 111 and 002 reflections at 2θ = 34.71° and 40.77°, respectively. The corresponding 111 and 002 interplanar spacings, $d_{111} = a/\sqrt{3}$ and $d_{002} = a/2$, yield the same lattice constant a = 0.442 nm, about 0.6% smaller than the value (0.4456 nm) reported for bulk $TaC_{0.99}$.[9] While residual stresses can influence the lattice constants,[46] since TaC is elastically isotropic[47] and given that I measure the same a values in both 111 and 002 oriented grains, I suggest that the observed smaller lattice constant is due to C-vacancies rather than lattice strain. Bowman *et al.*[45] suggested that the lattice parameter $a(x)$, measured in Ångstroms, changes linearly with carbon content x in TaC_x as $a(x) = 4.3007 + 0.1563x$. Using this relation, I determined that x = 0.76, i.e., $TaC_{0.76}$ layers are grown with $p_c = 5.0 \times 10^{-6}$ Torr. In contrast, for the film deposited with $p_c = 5.0 \times 10^{-4}$ Torr, I obtain a = 0.446 and 0.445 nm using 111 (2θ = 34.78°) and 002 (2θ = 40.55°) reflections, respectively. Both these a values are nearly the same as that of the bulk stoichiometric TaC, indicating the growth of stoichiometric TaC crystals.

I used TEM coupled with EDS to determine the microstructural and compositional evolution of the films as a function of the ethylene partial pressure. Figs. 3.2(a) and (b) are representative cross-sectional TEM images obtained from the Ta-C film sputter-deposited in pure Ar (p_c = 0) at T_s = 1123 K. The TEM image in Fig. 3.2(a) shows dense columnar

microstructure and I measure a film thickness of 148 ± 3 nm. The high-resolution TEM (HRTEM) image in Fig. 3.2(b) shows layered structure and associated Fourier transform (inset in Fig. 3.2(b)) indicates that the film is polycrystalline. The spots observed in the Fourier transform correspond to α-Ta_2C. With the introduction of small amounts of ethylene ($p_c = 5.0 \times 10^{-6}$ Torr), we obtain slightly thicker (154 ± 15 nm) and porous film with highly facetted surfaces and columnar grains (see Fig. 3.3(a)), compared to the layers deposited at $p_c = 0$. Lattice-resolution TEM image (Fig. 3.3(b)) and selected area electron diffraction (SAED) pattern (inset in Fig. 3.3(b)) with four-fold symmetric spots acquired along [010] zone axis from near the film/substrate interface of the sample reveal cube-on-cube heteroepitaxy of $TaC_x(001)$ on MgO(001). The lattice-resolved TEM image seems to suggest coherent growth of the film for up to 20 nm near the film-substrate interface. However, in the SAED pattern, we observe two sets of diffraction spots indicating that the film is not lattice-matched with the substrate. From the $h00$ reflections, I measure $a = hd_{h00} = 0.442$ nm for the TaC_x film, which is in good agreement with the a values extracted from XRD measurements of both d_{002} and d_{111}. That is, the film lattice is fully relaxed at the film-substrate interface. This is reasonable since lattice mismatch ($[a-a_{MgO}]/a_{MgO}$) is rather large (~ 5%). I do not observe (either due to limited resolution in the TEM images or otherwise) any misfit dislocations at the interface even though the critical thickness h_c for the onset of dislocations in films[48, 49] with 5% mismatch is $h_c = 0.8$ nm. (In calculating h_c, I use the relation,[48] $h_c = \left(\frac{b}{f}\right)\left[\frac{1}{4\pi(1+v)}\right]\left[\ln\left(\frac{h_c}{b}\right)+1\right]$ with the Burgers vector $b = \frac{1}{2}[110] = a/\sqrt{2} = 0.3125$ nm and Poisson ratio $\nu = 0.22$.[50]) In addition to dislocations, twinning has been shown to relieve stresses and the critical thickness associated with twinning is expected to be larger, from $12b$ to $30b$,[51] which yields h_c values between 4.7 ~ 9.4 nm for TaC. These predictions seem to be consistent with our experimental observations, see Figs. 3.3(c) and (d). The TEM image in Fig.

3.3(c) obtained from the same sample along [110] zone axis reveals twins at ~20 nm away from the substrate. Higher resolution TEM image (Fig. 3.3(d)) from the region bounded by a square in Fig. 3.3(c) shows 111 twins. While twinning has been observed in bulk TaC subjected to high pressures (>7.7 GPa),[52] I believe that this is the first report of growth twins in TaC.

To validate the TEM results and to better understand the orientation relations in the TaC_x/MgO(001) film, I collected TaC 002 and TaC 111 XRD pole figures from the sample deposited at $p_c = 5.0 \times 10^{-6}$ Torr and the data are presented as polar plots in Fig. 3.4. Figs. 3.4(a) and (b) are the MgO substrate 002 and 111 XRD pole figures, respectively, which serve as the reference for the data presented in Figs. 3.4(c) and (d). In the TaC 002 pole figure (Fig. 3.4(c)), the highest intensity peaks are observed at $(\chi,\phi) = (0^o,0^o)$ and $(90^o,0^o)$, $(90^o,90^o)$, $(90^o,180^o)$, and $(90^o,270^o)$ not visible in this plot, while in the TaC 111 pole figure (Fig. 3.4(d)), the highest intensity peaks are at $(\chi,\phi) = (54^o,45^o)$, $(54^o,135^o)$, $(54^o,225^o)$, and $(54^o,315^o)$. In both the TaC 002 and 111 pole figures, the highest intensity peaks are at the same (χ,ϕ) values as those of the MgO substrate 002 and 111 reflections, respectively. These results imply the existence of TaC grains on the MgO(001) substrate with the following cube-on-cube orientational relationship: $(100)_{TaC} \parallel (100)_{MgO}$ and $[001]_{TaC} \parallel [001]_{MgO}$. Interestingly, we also observe twelve additional peaks with four-fold symmetry in both the TaC 002 and 111 pole figures. I attribute these peaks to the presence of four 111-oriented TaC crystals formed by twinning with respect to 111. I test my hypothesis by simulating the XRD pole figures of 002 and 111 reflections (see Figs. 3.4(e) and (f)) for multiply twinned TaC. In the simulation, I start with a B1-TaC(001) single crystal and superpose three more crystals such that twins form across (111), $(\bar{1}11)$, $(1\bar{1}1)$, and $(\bar{1}\bar{1}1)$. The simulated patterns match the experimental data, thus validating the existence of twins in the as-deposited TaC_x/MgO(001) film.

TEM image in Fig. 3.5(a) obtained from the sample grown using the highest ethylene partial pressure, $p_c = 5.0 \times 10^{-4}$ Torr shows uniform contrast indicative of homogeneous composition and/or microstructure. The film is relatively smooth and considerably thicker (204 ± 2 nm) than those deposited at lower p_c, likely due to increased incorporation of carbon at higher p_c. Higher resolution TEM image of the sample (Fig. 3.5(b)) reveals that the film is composed of nanoscale (~ 5 nm size) crystallites embedded in an amorphous matrix.

I acquired EDS data (not shown) along the thickness of the Ta-C thin films sputter-deposited using different p_c as a means to determine spatial variations (if any) in Ta and C contents within the films. While C content in the film grown using $p_c = 0$ is not accurately determined, I find that the C/Ta ratios in all the other samples are fairly uniform across the films. The estimated C/Ta ratios increase as expected with increasing p_c from 0.8 ± 0.13 at $p_c = 5.0 \times 10^{-6}$ Torr to 2.9 ± 0.54 at $p_c = 5.0 \times 10^{-4}$ Torr. In addition to Ta and C, I find non-negligible amounts of O up to 28 at.%, 26 at.%, and 37 at.% in the films deposited using pure Ar, $p_c = 5.0 \times 10^{-6}$ Torr, and 5.0×10^{-4} Torr, respectively. Prior sputter-deposition experiments carried out in the same UHV system,[29, 30, 34] residual gas analyses of gas compositions in UHV and in Ar/C_2H_4 gas mixtures with different p_c, and *in situ* AES measurements of surface compositions of Ta-C films sputter-deposited using the same TaC target indicate that the deposition chamber, Ar and C_2H_4 gases, and the as-deposited Ta-C samples are all free of oxygen. Therefore, I attribute the O signal detected in EDS to oxygen incorporation in the samples upon air-exposure and/or during the TEM sample preparation.

I complement the EDS measurements, which provide estimates of the total C content, with XPS to determine p_c-dependent changes in the relative fractions of bonded vs. free C contents in the Ta-C films. Figs. 3.6(a-c) are representative XPS spectra around C 1*s* and Ta 4*f*

obtained from the Ta-C films grown with p_c = (a) 0, (b) 5.0×10^{-6} Torr, and (c) $p_c = 5.0 \times 10^{-4}$ Torr. In these spectra, peaks associated with Ta-O bonds, if present, would appear at binding energies 29.3 eV ($4f_{5/2}$) and 27.4 eV ($4f_{7/2}$). The open circles and squares are XPS data acquired from the samples after 600 s and 1800 s of Ar^+ etching, respectively. In Fig. 3.6(a) right panel, we observe two Ta 4*f* peaks at 21.7 eV ($4f_{7/2}$) and 23.5 eV ($4f_{5/2}$), irrespective of the etching time. In the left panel, we observe two C 1*s* peaks at 282.4 eV and 284.2 eV in the XPS spectra obtained after 600 s of etching (the open circles in Fig. 3.6(a)), which I attribute to Ta-C and C-C bonds, respectively. The C-C peak disappears after 1800 s of etching (open squares in Fig. 3.6(a)). These results suggest the existence of free-C in the top region, closer to the surface, of the sample. At higher $p_c = 5.0 \times 10^{-6}$ Torr, I find only one C 1*s* peak at 282.7 eV due to Ta-C bonds (see Fig. 3.6(b)); the absence of peaks due to C-C bonds imply that the thin film does not have any free carbon. However, I cannot rule out the possibility of free-C because these XPS data are acquired after Ar^+ etching, which is known to preferentially remove C from the samples.[53] I also observe ~ 1.1-1.2 eV shift in Ta 4*f* peaks to higher energies, 22.8 eV ($4f_{7/2}$) and 24.7 eV ($4f_{5/2}$), compared to those in Fig. 3.6(a) and are associated with Ta-C bonds in B1-TaC_x.[54] XPS data (Fig. 3.6(c)) from the sample grown using the highest $p_c = 5.0 \times 10^{-4}$ Torr show two C 1*s* peaks, corresponding to Ta-C and C-C bonds. That is, the film is composed of free-carbon and TaC_x. (In contrast with the C 1*s* spectra in Fig. 3.6(a), the C-C peak in Fig. 3.6(c) does not disappear after 1800 s of etching, presumably due to higher and uniform carbon concentration in the sample.) Since the position of the C-C peak corresponds to that of *sp*2 bonding (284.2 eV) rather than *sp*3 (285.0 eV), I expect that the free-carbon in the film is likely to be graphitic. However, HRTEM images and associated Fourier transforms did not provide any evidence of graphite in the film. I note that the peaks associated with Ta-C bonds in C 1*s*

spectrum are all shifted to higher binding energies, by ~ 2.0 eV and both the peaks in Ta 4*f* spectrum by 0.4 eV with respect to those observed (see Fig. 3.6(b)) in the sample deposited using $p_c = 5.0 \times 10^{-6}$ Torr. I attribute this increase in binding energies to increased carbon content in the carbide. In this particular sample, I also find a relatively stronger signal at energies around 26 and 28 eV, associated with Ta-O bonds. As mentioned in the previous section, my EDS measurements have also revealed the presence of oxygen across the film and is likely a result of air exposure of the as-deposited films.

My XPS results are consistent with both the XRD (Fig. 3.1) and the TEM (Figs. 3.2-3.3) data, all of which show that the Ta-C film composition changes with p_c. The observation of Ta_2C phase in the samples deposited with $p_c = 0$ (and $p_c = 5.0 \times 10^{-7}$ Torr) using TaC target is unexpected. This can occur if (1) B1-structured TaC_x is energetically unstable compared to Ta_2C + C two-phase mixtures and/or (2) some amount of carbon released from the TaC target is lost to the ambient during sputter-deposition. The former is plausible,[7] however, my XPS data (see Fig. 3.6(a)) is inconclusive regarding the presence of free-C in the film deposited with $p_c = 0$. The absence of C-C peak in the spectra (Fig. 3.6(b)) obtained from the sample grown using Ar/C_2H_4 gas mixtures with $P_c = 5.0 \times 10^{-6}$ Torr supports the latter possibility. Given that the sputtering efficiencies and the mean free paths of the sputtered species depend on their atomic masses relative to the gas (Ar) and gas pressure,[55] respectively, it is likely that not all carbon from the TaC target is incorporated into the film, resulting in the formation of Ta_2C. The introduction of C_2H_4 gas supplements the carbon lost during sputter-deposition and results in the growth of B1-TaC_x; with increasing p_c, the carbon concentration x in the B1 phase and the free-C content increase as more carbon is deposited from C_2H_4. As a result, I observe the transition from trigonal-structured Ta_2C (with $p_c = 0$) to a single-phase cubic $TaC_{0.76}$ (with $p_c = 5.0 \times 10^{-6}$ Torr)

and to a two-phase nanocomposite film of TaC crystallites embedded in C matrix (with $p_c = 5.0 \times 10^{-4}$ Torr).

Conclusion

In summary, I investigated the effects of small-amounts of ethylene gas (0.0025 to 2.5% of total pressure) on the compositional and microstructural evolution of sputter-deposited Ta-C/MgO(001) thin films. We obtain trigonal-structured Ta_2C using pure Ar and Ar/C_2H_4 gas mixtures with $p_c = 5.0 \times 10^{-7}$ Torr C_2H_4 (0.0025% of total pressure), B1-$TaC_{0.76}$ at higher C_2H_4 pressure ($p_c = 5.0 \times 10^{-6}$ Torr), and B1-TaC + free-C two-phase mixture at $p_c = 5.0 \times 10^{-4}$ Torr C_2H_4. All the films are polycrystalline with C_2H_4 pressure dependent microstructures and surface morphologies. The Ta_2C layers and the TaC + C are relatively smooth while the sub-stoichiometric TaC_x films deposited are porous with highly facetted surfaces. In the TaC_x/MgO(001) sample, we observe cube-on-cube heteroepitaxy with orientational relationships $(100)_{TaC} \parallel (100)_{MgO}$ and $<010>_{TaC} \parallel <010>_{MgO}$ near the film-substrate interface and the development of 111 twins and polycrystallinity away from the interface. In contrast, the film deposited using higher C_2H_4 partial pressure ($p_c = 5.0 \times 10^{-4}$ Torr) consists of nanoscale TaC crystallites embedded in free carbon. My results indicate that the sputter-deposited Ta-C film composition and microstructure are highly sensitive to the reactive gas fraction. The ability to reduce the reactive gas pressures down to a few ppm during sputter-deposition can open up opportunities for designing materials with potentially new properties. I expect that a similar approach can be used to controllably tune the growth characteristics of other reactively deposited thin films.

Figures

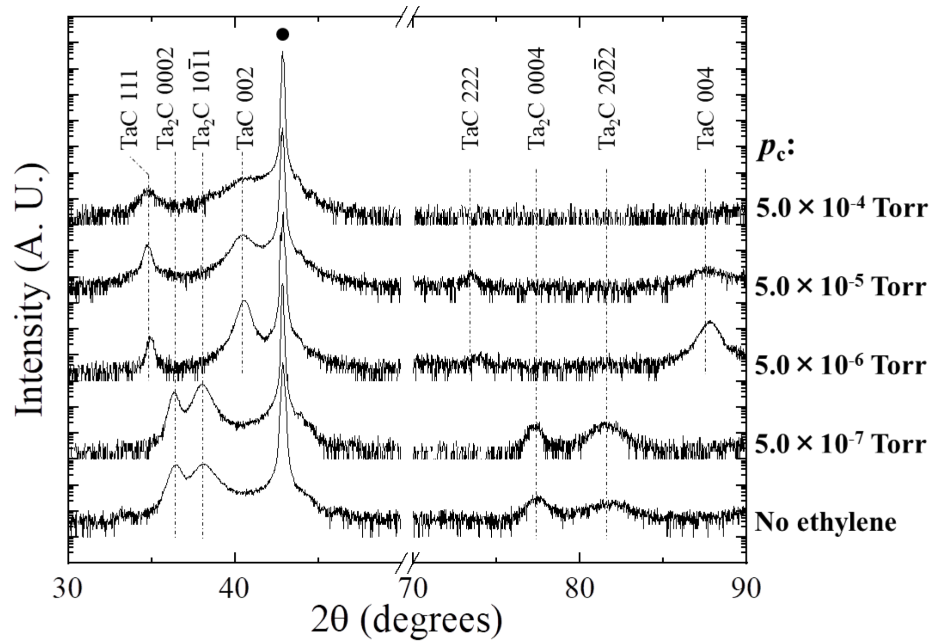

Figure 3.1 Representative X-ray diffraction (XRD) 2θ-ω spectra obtained from Ta-C thin films sputter-deposited on MgO(001) at 1123 K using Ar/C_2H_4 gas mixtures with different C_2H_4 partial pressures, p_c. Solid circle in the spectra denotes 002 reflection of the single-crystalline MgO substrate. Dotted lines indicate the expected peak positions of stoichiometric B1-TaC and trigonal-Ta_2C phases. For comparison of the relative peak intensities across the samples, all the data within each of the spectra are normalized with respect to the MgO 002 reflection peak intensity in that spectrum.

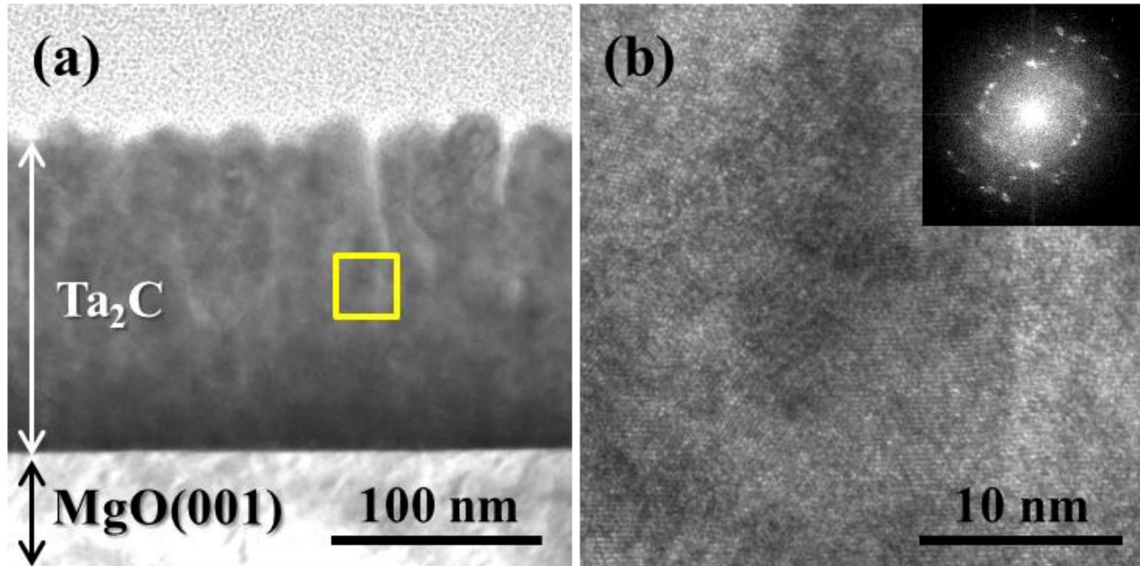

Figure 3.2: (a and b) Typical cross-sectional transmission electron microscopy (XTEM) images acquired from the Ta_2C film sputter-deposited using pure Ar, i.e., $p_c = 0$. (b) Higher-resolution TEM (HRTEM) image of the region highlighted by a yellow square in (a). Inset is a Fourier transform (FT) of the image in (b). The spots within the FT are identified as reflections due to polycrystalline α-Ta_2C.

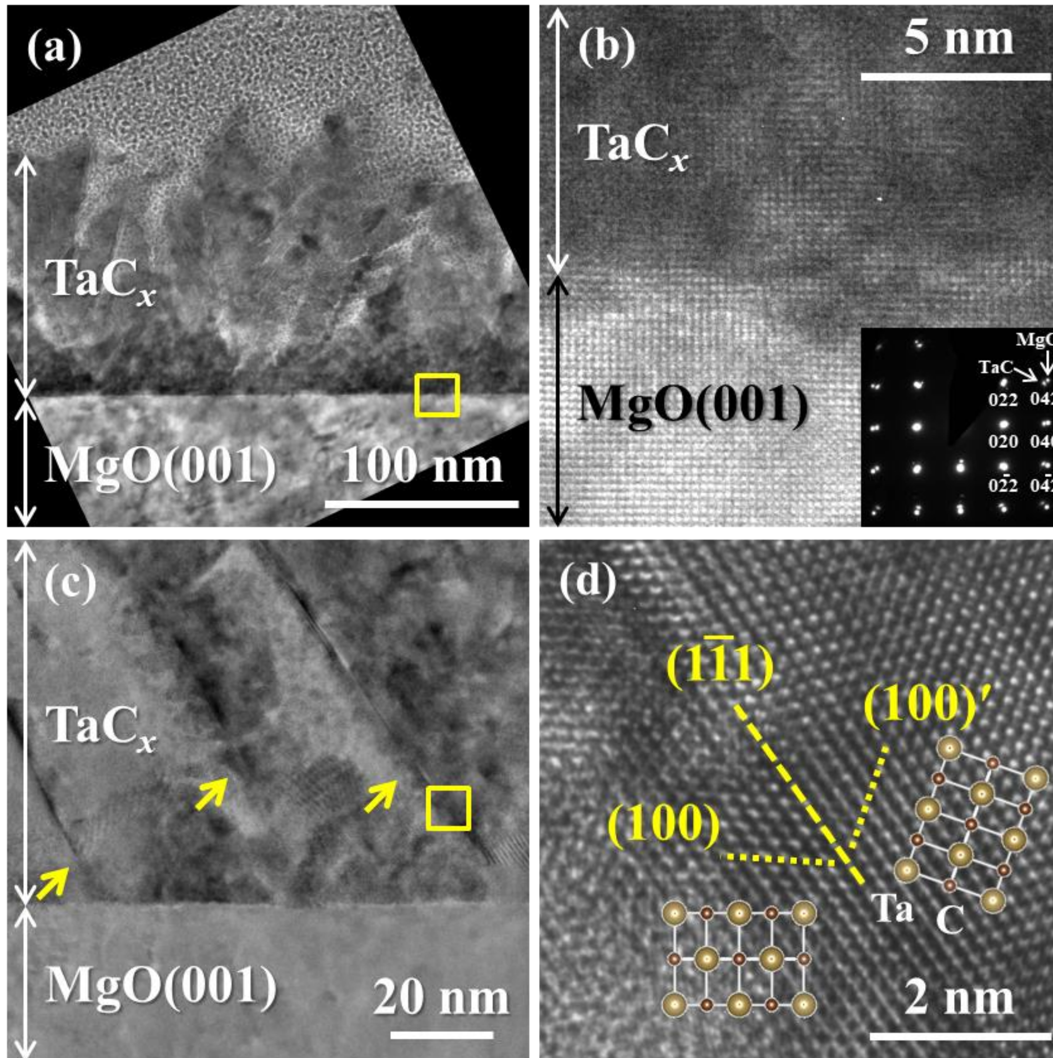

Figure 3.3: Characteristic XTEM images from the TaC_x layers sputter-deposited using $p_c = 5.0 \times 10^{-6}$ Torr, obtained along (a and b) [010] and (c and d) [011] zone axes. (b and d) HRTEM images of the regions highlighted by yellow squares in (a) and (c), respectively. Inset in (b) is a selected area electron diffraction pattern of the sample shown in (b). Arrows in (c) identify twin boundaries. Dotted lines in (d) highlight (100) and mirror (100)' planes in twinned crystals across a $(1\bar{1}1)$ plane shown by a dashed line with schematics of TaC lattice.[56]

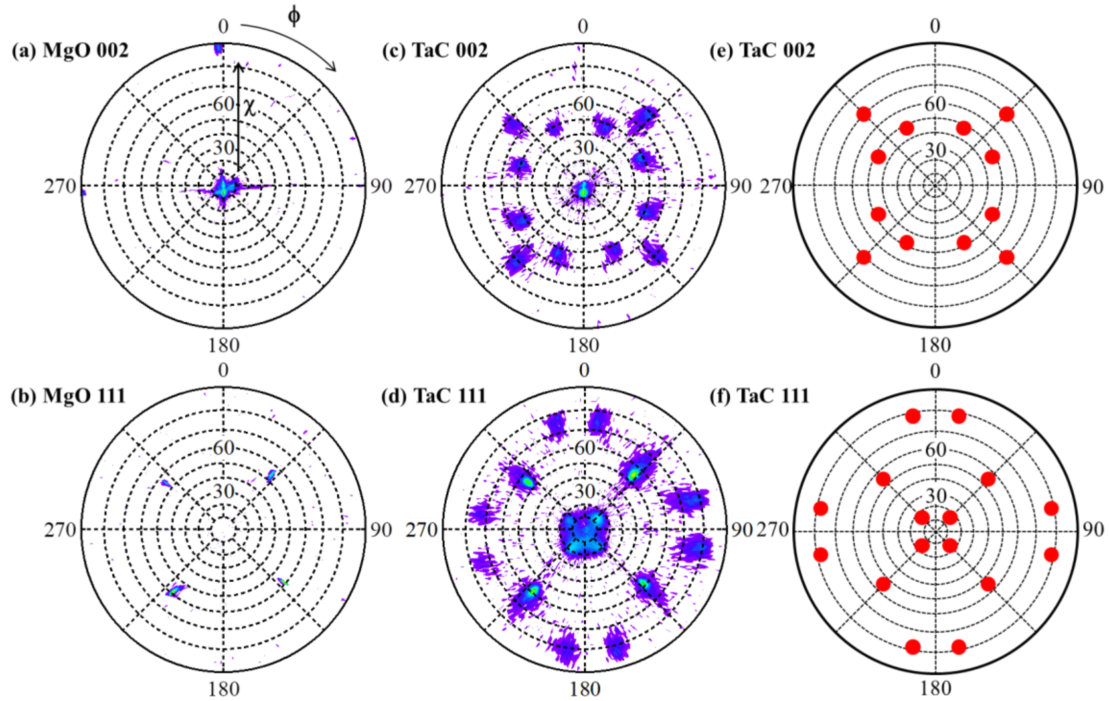

Figure 3.4: XRD pole figures of (a) MgO 002, (b) MgO 111, (c) TaC 002, and (d) TaC 111 reflections obtained from the TaC_x film deposited using $p_c = 5.0 \times 10^{-6}$ Torr. (e and f) Simulated pole figures of (e) TaC 002 and (f) TaC 111 reflections from a hypothetical construct of multiply twinned 111-oriented TaC crystals rotated 90° with respect to each other.

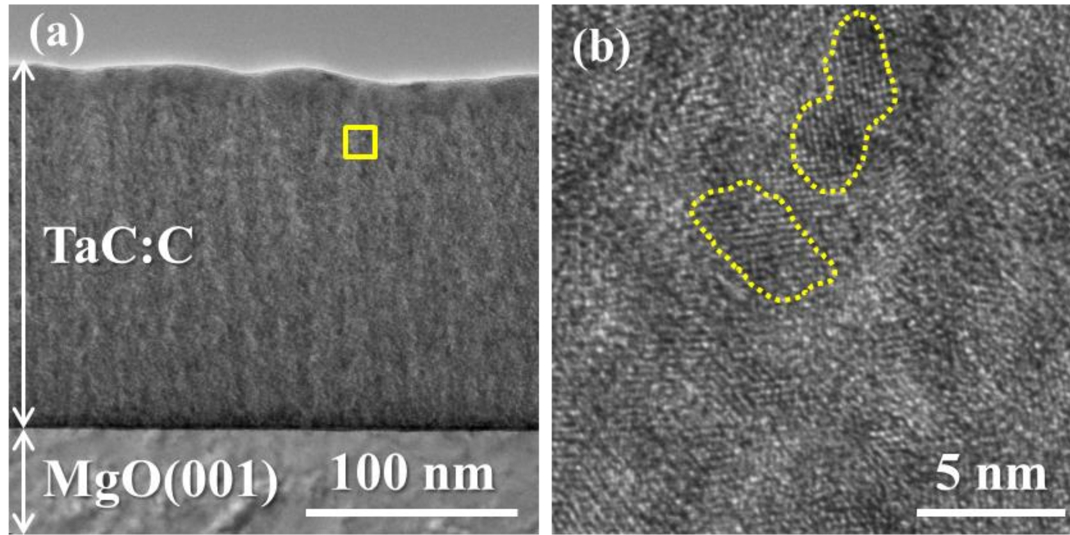

Figure 3.5: (a and b) Characteristic XTEM images from the TaC_x layers sputter-deposited using $p_c = 5.0 \times 10^{-4}$ Torr. (b) HRTEM image of the area marked with yellow square in (a). Lattice fringes visible in the image are due to TaC crystallites (approximately 5 nm in size), three of which are highlighted by yellow lines.

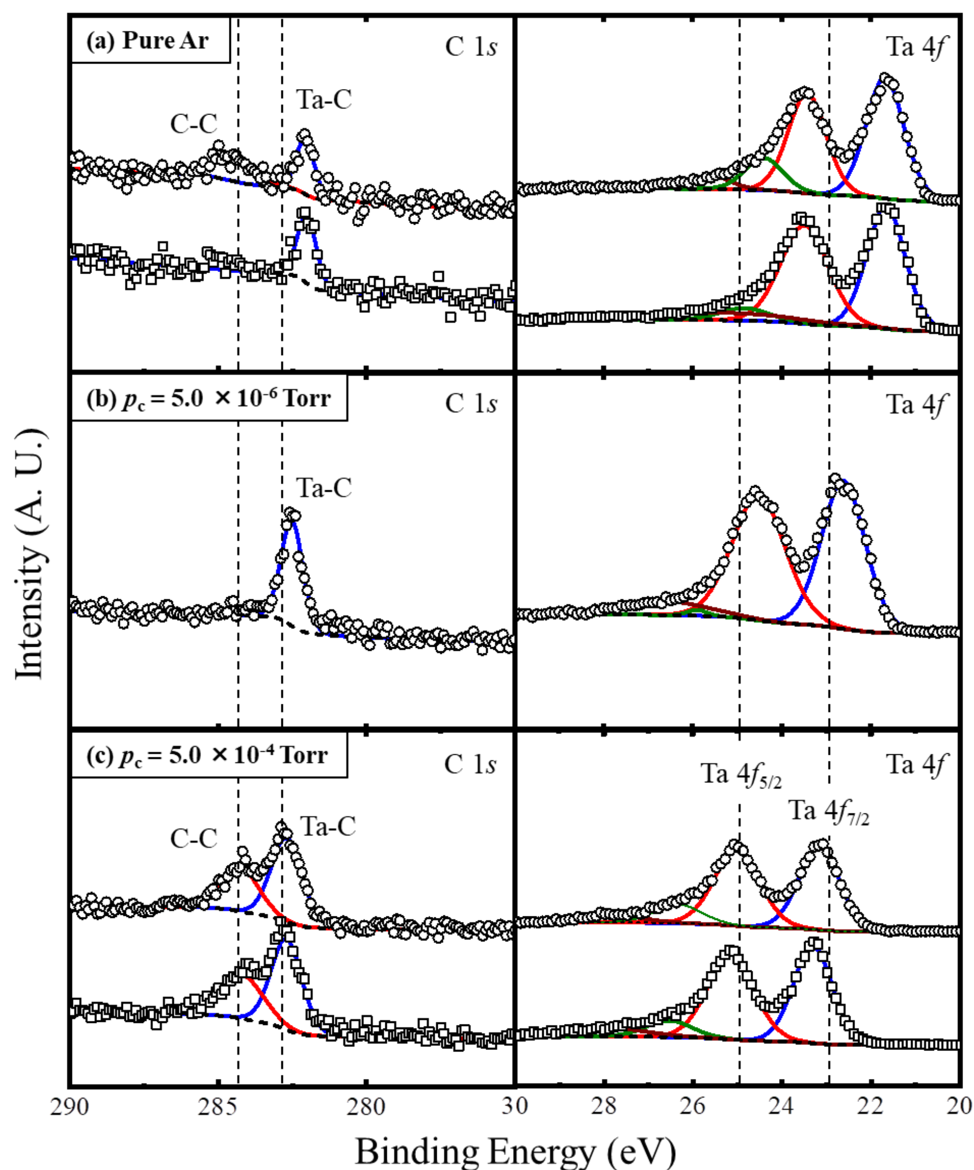

Figure 3.6: X-ray photoelectron spectra (XPS) around C 1*s* and Ta 4*f* peaks obtained from the films sputter-deposited using p_c = (a) 0, (b) 5.0 × 10^{-6} Torr, and (c) 5.0 × 10^{-4} Torr. Open circles and squares are spectra acquired after Ar^+ etching of the sample for 600 and 1800 s, respectively. Solid lines are Gaussian fits to the raw data. Dashed line is background. Vertical dashed lines in C 1*s* spectra indicate binding energies characteristic of graphitic carbon and stoichiometric TaC, while those in Ta 4f correspond to Ta $4f_{5/2}$ and $4f_{7/2}$ of stoichiometric TaC.

CHAPTER 4. Ultra-high vacuum dc magnetron sputter-deposition of 0001-textured trigonal α-Ta_2C/Al_2O_3(0001) thin films

Introduction

Among the tantalum carbides (Ta-Cs), B1-TaC has by far received the most attention. Relatively little is known concerning the other Ta-C compounds (e.g., Ta_2C, Ta_3C_2, Ta_4C_3, and Ta_6C_5), which are also known for their ultra-high melting points (for example, ~ 3600 K for trigonal α-Ta_2C)[7] and their thermomechanical and electrical properties.[8, 57-65] α-Ta_2C is relatively softer with superior ductility compared to B1-TaC at elevated temperatures[58] due to the operation of multiple slip systems.[58, 66, 67]

As mentioned in the previous chapters, Ta-C thin films are most commonly grown via magnetron sputter-deposition.[14, 23, 35, 44, 68-72] While most of the existing literature is aimed at obtaining B1-TaC thin films, relatively few reported the growth of Ta_2C thin films;[70-73] other studies observed the unintentional formation of the Ta_2C phase.[35, 44, 69] Given the potential applications of Ta_2C in high-temperature structural applications, it is surprising that very little is known concerning the synthesis and microstructural evolution of Ta_2C. Here, I focus on understanding the growth-related aspects of sputter-deposited Ta_2C thin films.

In this chapter, I report on the microstructural evolution in Ta_2C thin films deposited on single-crystalline Al_2O_3(0001) substrates via UHV dc magnetron sputtering of a TaC target in pure Ar discharges at T_s between 1073 K and 1373 K for times t up to 30 min. XRD and TEM characterization of the as-deposited layers reveal the growth of α-Ta_2C thin films with 0001 preferred orientation at all T_s. I find that thickness decreases while both crystallinity and surface smoothness of the films improve monotonically with increasing T_s. I observe enhancement in 0001 texture with increasing T_s from 1073 K up to 1273 K. At higher T_s (= 1373 K), the thinner Ta_2C layers grow heteroepitaxially on Al_2O_3(0001) with the following crystallographic

relationship $(0001)_{Ta_2C} \parallel (0001)_{Al_2O_3}$ and $[10\bar{1}0]_{Ta_2C} \parallel [11\bar{2}0]_{Al_2O_3}$ and develop polycrystallinity with increasing thickness. Based on these results, I suggest that the competition between enhanced surface mass transport and reduced carbon incorporation during deposition at elevated temperatures determine the morphology and texture of the Ta_2C thin films

Results and discussion

Figure 4.1(a) shows typical 2θ-ω XRD scans obtained from Ta-C/Al_2O_3(0001) thin films sputter-deposited for t = 30 min. at T_s = 1073, 1173, 1223, 1273, and 1373 K. In the data, the peaks labeled **s** at 2θ = 41.68° and 90.76° are due to 0006 and 00012 reflections, respectively of the single-crystalline, corundum-structured Al_2O_3(0001) substrates (JCPDS-ICDD No. 46-1212) and the other peak at 2θ = 64.54° is a forbidden Al_2O_3 0009 reflection that is likely due to defects in the Al_2O_3(0001) crystals.[74, 75] To facilitate direct comparison of the XRD data across the samples, intensities in each of the curves are normalized to the highest intensities associated with Al_2O_3 00012 peak. The XRD data of the film deposited at the lowest T_s = 1073 K reveal broad overlapping peaks at 2θ values around 36°, 38°, 78°, and 82°. In comparison, the XRD data obtained from the films deposited at $T_s \geq$ 1173 K show peaks at or close to 2θ = 36.32°, 38.24°, 59.46°, 77.16°, 82.02°, and 97.94°; I index these peaks as 0002, $10\bar{1}1$, $2\bar{1}\bar{1}0$, 0004, $20\bar{2}2$, and $3\bar{1}\bar{2}0$ reflections, respectively, of trigonal α-Ta_2C ($P\bar{3}m1$).[76] (For reference, Cu $K_{\alpha 1}$ XRD peaks of high-intensity reflections 111 and 002 of stoichiometric B1-TaC are expected at 2θ = 34.78° and 40.55°, respectively.[35]) The observation of multiple reflections is indicative of polycrystallinity. The XRD data of the samples grown at the higher T_s = 1273 and 1373 K show weaker intensity peaks labeled with asterisks at 2θ = 25.40° and 55.76°. While I am unable to attribute the peak at 25.40° to any of the possible Ta-C compounds or graphite (JCPDS-ICDD

No. 41-1487), I suggest that the peak at 55.76° is likely due to α-Ta_2C 0003 reflection, expected at 2θ = 55.82°.

From the XRD data in Fig. 4.1(a), I measure full width at half maxima, Γ_{0002} and $\Gamma_{10\bar{1}1}$, respectively of 0002 and $10\bar{1}1$ peaks, the two primary reflections in α-Ta_2C, and their relative intensities $I_{0002}/I_{10\bar{1}1}$ at all T_s. Fig. 4.1(b) shows the T_s-dependent variations in Γ_{0002}, $\Gamma_{10\bar{1}1}$, and $I_{0002}/I_{10\bar{1}1}$. I find that the Γ values of both 0002 and $10\bar{1}1$ peaks decrease monotonically, indicative of increase in out-of-plane coherence length[77] and hence improved overall crystallinity, with increasing T_s. $I_{0002}/I_{10\bar{1}1}$ increases from 2.2 at T_s = 1073 K to 13.1 at T_s = 1273 K and decreases to 3.0 at T_s = 1373 K. Given that the strongest intensity reflection is $10\bar{1}1$ and $I_{0002}/I_{10\bar{1}1}$ is 0.253 in powder XRD of α-Ta_2C,[76] the fact that $I_{0002}/I_{10\bar{1}1} > 2$ for the films deposited at all $T_s \geq 1023$ K implies that the Ta_2C films are highly 0001-oriented at all T_s. In my experiments, the strongest 0001 texture is obtained in the films deposited at 1273 K. The observed decrease in $I_{0002}/I_{10\bar{1}1}$ upon further increase in T_s to 1373 K is suggestive of a disruption in 0001-oriented crystal growth, presumably due to change in the film composition.

I measure out-of-plane lattice parameters c from the peak positions of Ta_2C 0002 and 0004 reflections in Fig. 4.1(a) and use them as input to extract in-plane lattice parameters a from the 2θ values of $10\bar{1}1$, $20\bar{2}2$, and $3\bar{1}\bar{2}0$ reflections. Fig. 4.1(c) shows T_s-dependent variations in relative changes, ε_a [= $(a-a_o)/a_o$], ε_c [= $(c-c_o)/c_o$], and ε_V [= $(V-V_o)/V_o$] in a, c, and unit cell volume V (= $3\sqrt{3}a^2c/2$) respectively, compared to the corresponding values a_o (= 0.3103 nm), c_o (= 0.4938 nm), and V_o (= 0.1235 nm^3) of bulk α-Ta_2C.[76] Errors associated with ε_a, ε_c, and ε_V are calculated from the measurement uncertainties associated with the a and c values extracted from the XRD data. I find that the a and c values of Ta_2C layers deposited at T_s = 1073 K are 1.5% larger and 0.6% smaller, respectively than the a_o and c_o values, yielding a 2.5% larger V

compared to V_o. At $T_s \geq 1173$ K, the c values are, within the measurement uncertainties, the same as c_o and seemingly independent of T_s, whereas the a, and hence V, values decrease with increasing T_s. Given that the in-plane lattice mismatch is at least 13%, at 30° in-plane orientation, between α-Ta_2C(0001) and Al_2O_3(0001), significantly higher than the measured ε_a values, I suggest that the films are relaxed and attribute the observed T_s-dependent changes in a (and V) to variations in carbon content within the lattice.[35]

In order to better understand the effect of T_s on the development of microstructure within the Ta_2C layers, I carried out TEM characterization of the Ta_2C films. The top and bottom panels in Fig. 4.2 show typical (a-c) bright field and (d-f) high-angle annular dark field (HAADF) scanning TEM (STEM) images, respectively of the layers deposited at T_s = (a, d) 1073 K, (b, e) 1173 K, and (c, f) 1373 K. I find that the films deposited at lower T_s (= 1073 K) are relatively rough while those grown at higher T_s (= 1373 K) exhibit smoother surfaces. All the films, irrespective of the T_s, appear dense. From the XTEM images, I measure thicknesses of 91 ± 2.4 nm at 1073 K to 81 ± 1.6 nm at 1173 K, and 72.8 ± 0.9 nm at 1373 K, indicating that film thickness and hence R decrease with increasing T_s. Given that the substrate-film interfaces appear sharp irrespective of the T_s, I rule out interfacial reactions[30] and suggest that a reduction in sticking coefficient of the deposited species (most likely C) with increasing T_s as a possible reason for the observed decrease in film thickness. This is plausible since I observe the formation of C-deficient Ta_2C, rather than TaC, during sputter-deposition using nearly stoichiometric TaC target and consistent with previous results.[35] HAADF STEM images in Figs. 4.2(d) and (e) show fairly uniform contrast, suggestive of compositional homogeneity, across the films. However, Fig. 4.2(f) reveals distinctively darker contrast, characteristic of lighter atoms, with increasing thickness of the Ta_2C layer grown at higher T_s = 1373 K). Since the film is deposited *via*

sputtering of TaC target in pure Ar atmosphere, I attribute the observed darker contrast in the upper portion of the film to increased carbon concentration, presumably due to surface segregation of C atoms during deposition.

In order to understand the spatial variations in composition and the suppression of 0001-texture at the highest T_s = 1373 K, I investigated the effect of thickness on the crystallinity of films grown at T_s = 1373 K. Fig. 4.3(a) shows 2θ-ω XRD scans obtained from the $Ta_2C/Al_2O_3(0001)$ layers deposited for t = 3 and 10 min. along with the data from t = 30 min. sample shown in Fig. 4.1(a). I find primarily α-Ta_2C 0002 reflections for t = 3 min., 0002 and $10\bar{1}1$ reflections for t = 10 min., and multiple reflections for t = 30 min. The thinnest film (t = 3 min. sample) shows fringes (Laue oscillations) around 0002 peak, indicative of abrupt and/or high-quality substrate-film interfaces. With further increase in t, we observe a well-defined $10\bar{1}1$ reflection and $I_{0002}/I_{10\bar{1}1}$ decreases from 4.0 to 3.0 with increasing t from 10 to 30 min., indicative of reduced 0001-texture with increasing film thickness. Although 0001-texture is suppressed in thicker films, I find that Γ_{0002} decreases monotonically from 1.08° to 0.43° with increasing t from 3 to 30 min.; I attribute this result to increase in out-of-plane coherent length with increasing thickness. From the peak positions of Ta_2C 0002 and 0004 reflections, I measure c values of 0.4938 ± 0.0001 nm, 0.4940 ± 0.0001, and 0.4941 ± 0.0001 nm for t = 3, 10, and 30 min. samples, respectively. The observed increase in c with t, although small, is suggestive of lattice distortion in the thicker films.

To identify the in-plane crystallographic relationship between $Ta_2C(0001)$ and $Al_2O_3(0001)$ at the onset of growth, I acquired XRD pole figures of Ta_2C $10\bar{1}1$ and Al_2O_3 $11\bar{2}6$ reflections from the $Ta_2C/Al_2O_3(0001)$ film deposited for t = 3 min. at T_s = 1373 K and are presented as polar plots in Figs. 4.3(b) and 4.3(c), respectively. In obtaining the pole figures,

since the Ta_2C film is highly 0001-oriented and the substrate is 0001-oriented Al_2O_3 single-crystal, I use 2θ values of 38.08° and 57.50°, respectively, corresponding to the bulk α-Ta_2C $10\bar{1}1$ and corundum-structured Al_2O_3 $11\bar{2}6$. I would like to point out that the 4-fold symmetric set of spots at $\chi = 20^o$ in Fig. 4.3(c) are due to Si 222 reflections ($2\theta = 58.85^o$) from a miscut Si(100) wafer that is used to mount the samples. (In Fig. 4.3(b), I also find 3-fold symmetric spots at $\chi = 32^o$, origin of which is unknown.) In Figs. 4.3(b) and (c), we observe 6-fold symmetric Ta_2C $10\bar{1}1$ reflections at $\chi = 59 \pm 1^o$ and Al_2O_3 $11\bar{2}6$ reflections at $\chi = 39 \pm 1^o$, respectively, at the same in-plane rotation angles $\varphi = 0^o$, 60°, 120°, 180°, 240°, and 300°, indicating that $Ta_2C(10\bar{1}1)$ planes bear the same in-plane orientation as $Al_2O_3(11\bar{2}6)$. I note that the measured angles $\chi = 59 \pm 1^o$ in Fig. 4.3(b) and 39 ± 1° in Fig. 4.3(c) are nearly the same as the calculated interplanar angles, 61.4° and 42.3°, respectively, between (0001) and $(10\bar{1}1)$ of α-Ta_2C and between (0001) and $(11\bar{2}6)$ of Al_2O_3. From these results, which are consistent with the φ scans (not shown), I conclude that the orientation relationships for ultra-thin Ta_2C film with respect to the $Al_2O_3(0001)$ substrate are: $(0001)_{Ta_2C} \parallel (0001)_{Al_2O_3}$ and $[10\bar{1}0]_{Ta_2C} \parallel [11\bar{2}0]_{Al_2O_3}$. These results show that the Ta_2C layers begin to grow heteroepitaxially on $Al_2O_3(0001)$ during early stages of sputter-deposition and become polycrystalline with increasing thickness.

In order to understand the transition from heteroepitaxial to polycrystalline growth, I carried out XTEM characterization of the thinner and thicker $Ta_2C/Al_2O_3(0001)$ films deposited at $T_s = 1373$ K and the data are presented in Figs. 4.4 and 4.5, respectively. Fig. 4.4(a) is a representative lattice-resolution XTEM image of the Ta_2C layer deposited for $t = 5$ min. From the image, I measure the thickness of the film as ~ 16 nm, i.e. $R = 0.05$ nm/s. (In comparison, Ta_2C layer grown for $t = 30$ min. at the same T_s using the same deposition parameters is ≈ 73 nm

thick, see Figs. 4.2(c) and 4.5(a), corresponding to $R \approx 0.04$ nm/s, suggestive of t-dependent R.) I find wavy features aligned nearly parallel to the substrate, which I attribute to stacking of basal planes in Ta_2C, consistent with the observation of high-intensity 0002 reflection in XRD data in Fig. 4.3(a). Figs. 4.4(b) and (c) are representative Fourier transforms (FT) obtained, respectively from the regions bounded by yellow (Ta_2C film) and red (Al_2O_3 substrate) dotted squares in Fig. 4.4(a). I do not observe $10\bar{1}1$ spots in Fig. 4.4(b). From the observed symmetry of the reflections in Figs. 4.4(b) and (c), I identify the orientation relationship between the Ta_2C film and the substrate as $(0001)_{Ta_2C} \parallel (0001)_{Al_2O_3}$ and $[10\bar{1}0]_{Ta_2C} \parallel [11\bar{2}0]_{Al_2O_3}$. These results indicate that the film is highly 0001-oriented and exhibits the same orientation relationship with the substrate as the thinner (t = 3 min.) sample. Fig. 4.4(d) is a higher magnification TEM image of a portion of Fig. 4.4(a), highlighted by a green dotted square, showing layer stacking and a defect indicated by an arrow. In α-Ta_2C, along 0001, individual layers of C and Ta atoms are stacked on top of each other as αBCαBCα…, analogous to ABCABCA... stacking in 111-oriented face-centered cubic lattice, with capital and Greek letters corresponding to Ta and C layers, respectively.[8, 78] Defects in stacking may occur as a result of C-vacancies and result in the formation of anti-phase domains, i.e. domains with AβCAβCA… or ABγABγA… stacking instead of the ideal αBCαBCα…stacking. However, additional high-resolution TEM characterization is required to accurately determine the structure of these features.

Fig. 4.5(a) is a representative bright-field XTEM image of the thicker Ta_2C film deposited for t = 30 min. I find contrast undulations that appear as parallel 'stripes', most of which are oriented along the growth direction. A HRTEM image of the region bounded by a cyan dotted square in Fig. 4.5(a) is shown in Fig. 4.5(b). The image shows a portion of the substrate-film interface, where we observe atomic columns in the film aligned with those in the

substrate, suggestive of coherent growth of Ta_2C film on $Al_2O_3(0001)$ substrate. Inset in Fig. 4.5(b) is a FT of the entire field of view, in which I find only one set of reflections, consistent with my conclusion above. Figs. 4.5(c)-(f) are FTs of four regions from near the substrate-film interface up to the top of the film. Near the interface [Fig. 4.5(c)], the Ta_2C film exhibits 0001 orientation along the growth direction. At film thicknesses ~10 nm and farther from the interface [Figs. 4.5(d) and (e)], we observe 17° ~ 29° tilt in the 0001-oriented grains. Eventually, near the top of the film [Fig. 4.5(f)], I find grains with $1\bar{1}02$ orientation. These results, which show the transition from fully coherent 0001-oriented growth to a different orientation with increasing thickness, are consistent with the XRD results in Fig. 4.3(a).

To consistently explain the observed T_s and t dependent evolution of crystallinity in sputter-deposited Ta_2C thin films, I propose the following: crystallinity of the Ta-C layers deposited via sputtering of TaC target in inert Ar gas discharges depends on the carbon content in the lattice. Under my experimental conditions, I know that not all C released during sputtering of the TaC target is incorporated into the films deposited on oxide substrates at high T_s, a result of which is the growth of Ta_2C instead of TaC.[35] Since the adatom mobilities on refractory transition-metal compound surfaces are generally associated with high activation barriers,[79, 80] I expect that increasing T_s leads to enhanced surface mass transport and favors the formation of lower-energy {0001} surfaces, resulting in 0001-oriented films with smoother surfaces (see Figs. 4.1 and 4.2). An unintended consequence of increasing T_s, however, is the disproportionate reduction in the sticking coefficient of the incident C atoms compared to that of Ta atoms; here, I assume that the sticking coefficient of the lighter element C decreases more than that of the heavier Ta at the T_s (1073 ~ 1373 K) used in my experiments. As a result, the C content in the film decreases with increasing both T_s and t, consistent with the observed decrease in R with T_s

(Fig. 4.2) and t (compare the thicknesses of layers in Figs. 4.4 and 4.5). The change in C-content leads to lattice distortion [see for example Fig. 4.1(c)] during early stages of deposition followed by the formation of anti-phase domains [e.g., Fig. 4.4(d)] and eventually result in the growth of grains with other orientations as observed in Figs. 4.3 and 4.5.

Conclusion

In summary, I investigated the effects of substrate temperature (1073 K $\leq T_s \leq$ 1373 K) and deposition time on microstructural evolution of $Ta_2C/Al_2O_3(0001)$ thin films grown via UHV dc magnetron sputtering of TaC target in pure Ar atmospheres. We obtain 0001-oriented, α-Ta_2C films that are increasingly smoother and thinner with increasing T_s. The 0001-texture improves with increasing T_s up to 1273 K. At T_s = 1373 K, we observe highly coherent 0001-oriented growth with the following orientation relationship: $(0001)_{Ta_2C} \parallel (0001)_{Al_2O_3}$ and $[10\bar{1}0]_{Ta_2C} \parallel [11\bar{2}0]_{Al_2O_3}$ during the early stages of deposition followed by the formation of anti-phase domains and misoriented grains at the later times yielding polycrystalline layers with reduced 0001-texture. I attribute the improvement in film smoothness, crystallinity, and the 0001-texture with increasing T_s to increased surface adatom mobilities and the decrease in film thickness and the disruption in heteroepitaxial growth to the reduced incorporation of C leading to the formation of structural defects. I expect that these results provide new insights into the factors influencing the crystallinity of sputter-deposited α-Ta_2C thin films.

Figures

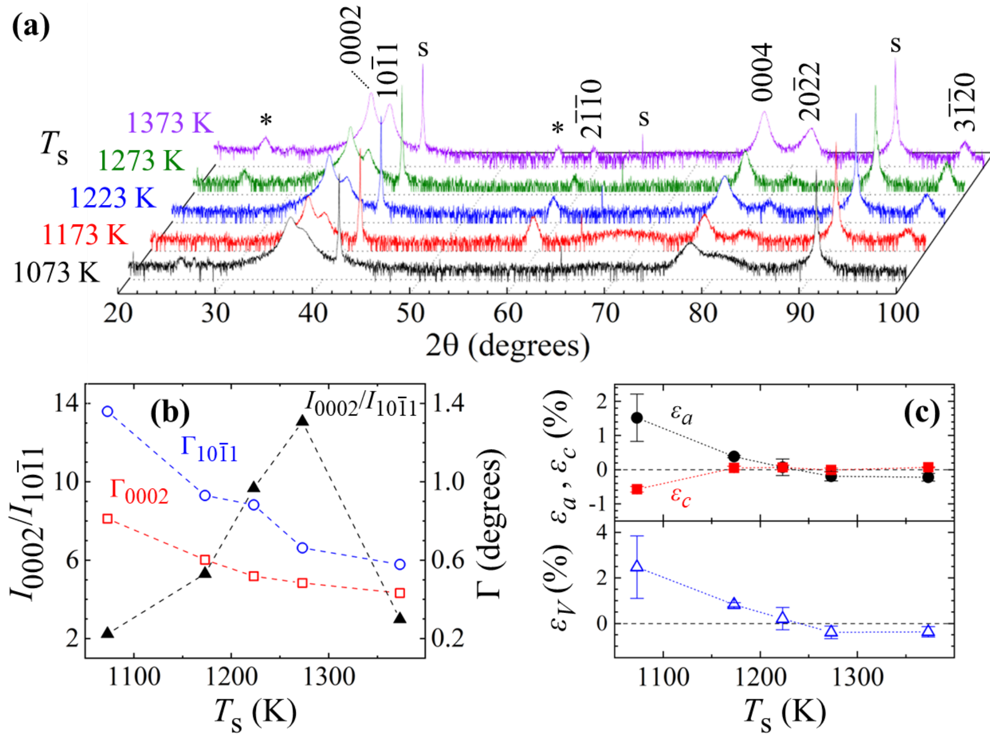

Figure 4.1: (a) Representative 2θ-ω XRD scans, color coded for clarity, from $Ta_2C/Al_2O_3(0001)$ thin films sputter-deposited for times t = 30 min. at different T_s. Intensities in each of the curves are normalized to that of the Al_2O_3 00012 reflection and are plotted on a logarithmic scale. Labels **s** indicate the peaks due to Al_2O_3 000l reflections with l = 6, 9, and 12 at progressively increasing 2θ values. Unidentified peaks are assigned asterisks and are discussed in the text. (b) Plots of full width at half maxima, $\Gamma_{10\bar{1}1}$ (open circles) and Γ_{0002} (open squares) of $10\bar{1}1$ and 0002 reflection peaks respectively, and their relative intensity ratios [$I_{0002}/I_{10\bar{1}1}$ (filled triangles)] as a function of T_s. (c) Plots of ε_a (solid circles), ε_c (solid squares), and ε_V (open triangles) vs. T_s, where a (c) is the in-plane (out-of-plane) lattice parameter of α-Ta_2C, extracted from the XRD scans in (a), V [= $(3\sqrt{3}/2)a^2c$] is the unit cell volume, and $\varepsilon_i = [(i-i_o)/i_o]\times100$, with i = a, c, and V. a_o (= 0.3103 nm), c_o (= 0.4938 nm), and V_o (= 0.1235 nm^3) correspond to bulk α-Ta_2C ($P\bar{3}m1$).[76]

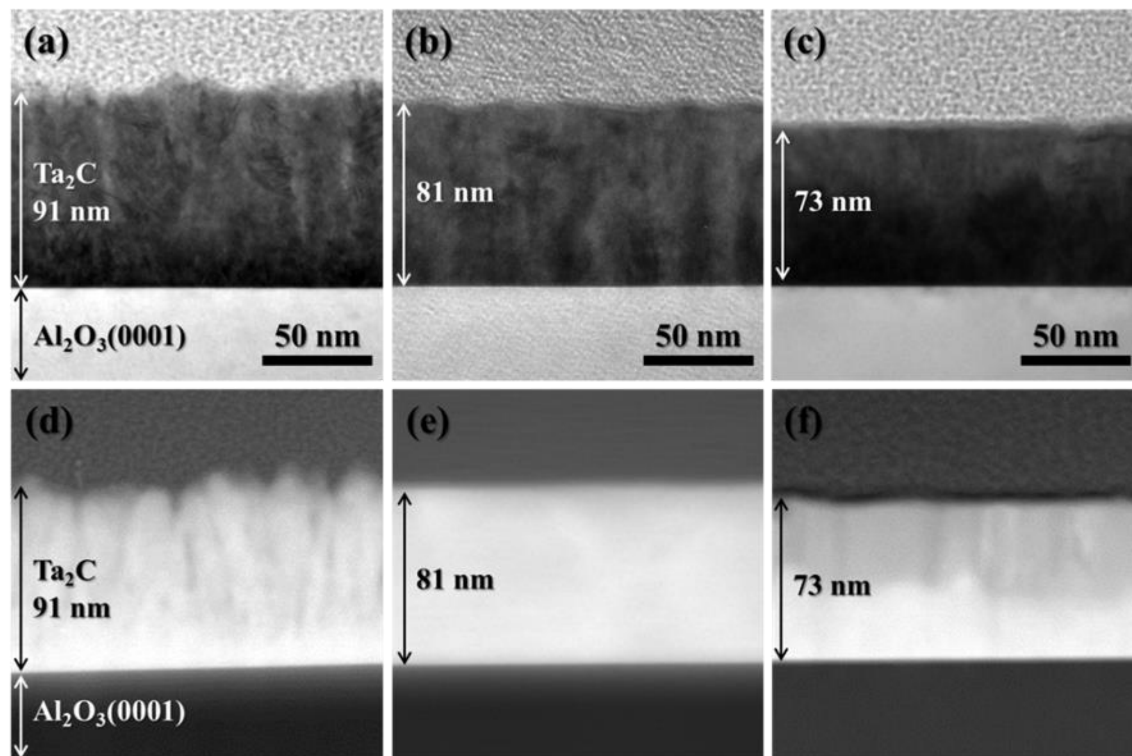

Figure 4.2: (top) XTEM and (bottom) high-angle annular dark field scanning TEM (HAADF STEM) images obtained from $Ta_2C/Al_2O_3(0001)$ films sputter-deposited for t = 30 min. at T_s = (a,d) 1073 K, (b,e) 1173 K, and (c,f) 1373 K.

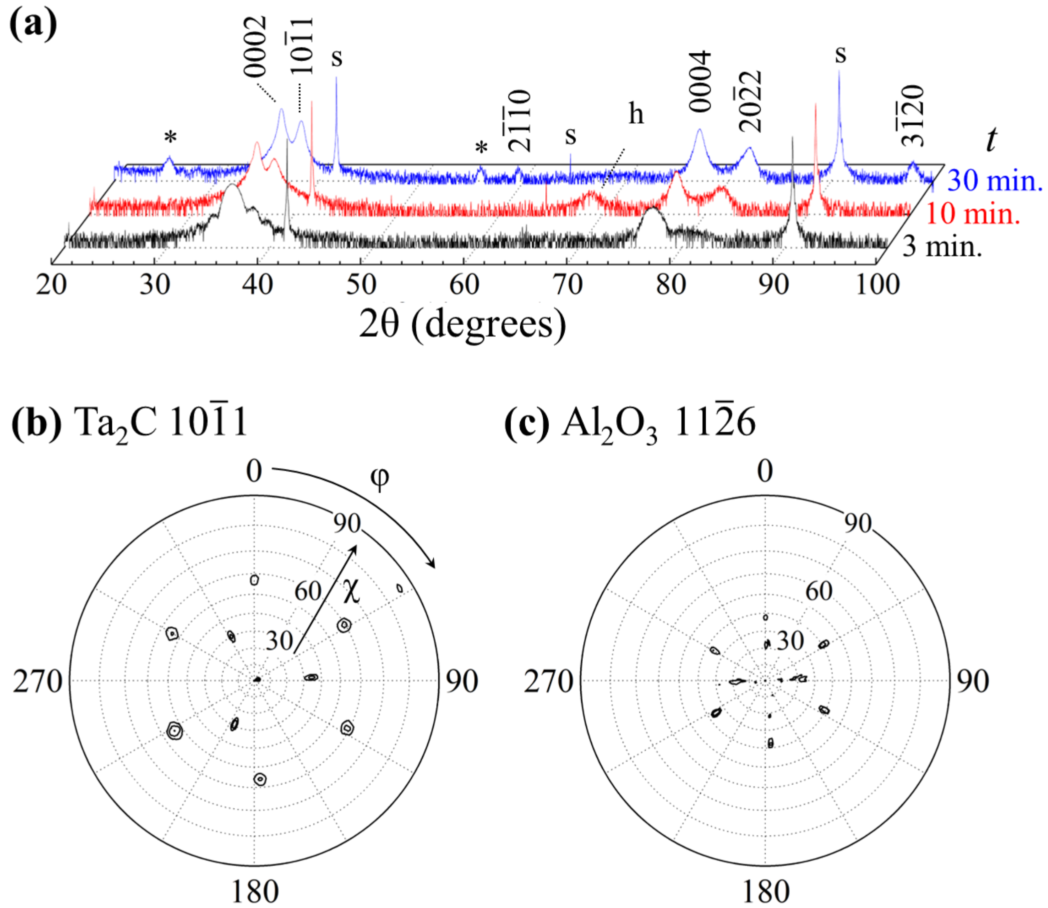

Figure 4.3: (a) 2θ-ω XRD data obtained from $Ta_2C/Al_2O_3(0001)$ layers sputter-deposited at T_s = 1373 K for t = 3, 5, 10, and 30 min. are plotted on logarithmic scale with intensities in each of the curves normalized to that of the Al_2O_3 00012 reflections. (Please note that the time axis is not to scale.) Peaks due to α-Ta_2C reflections are labeled as shown. **s** refers to $Al_2O_3(0001)$ single-crystal substrate reflections 0006, 0009, and 00012. **h** indicates background scattering from the sample holder. (b, c) XRD pole figures of (b) Ta_2C $10\bar{1}1$ and (c) Al_2O_3 $11\bar{2}6$ reflections obtained from the sample deposited at 1373 K for t = 3 min.

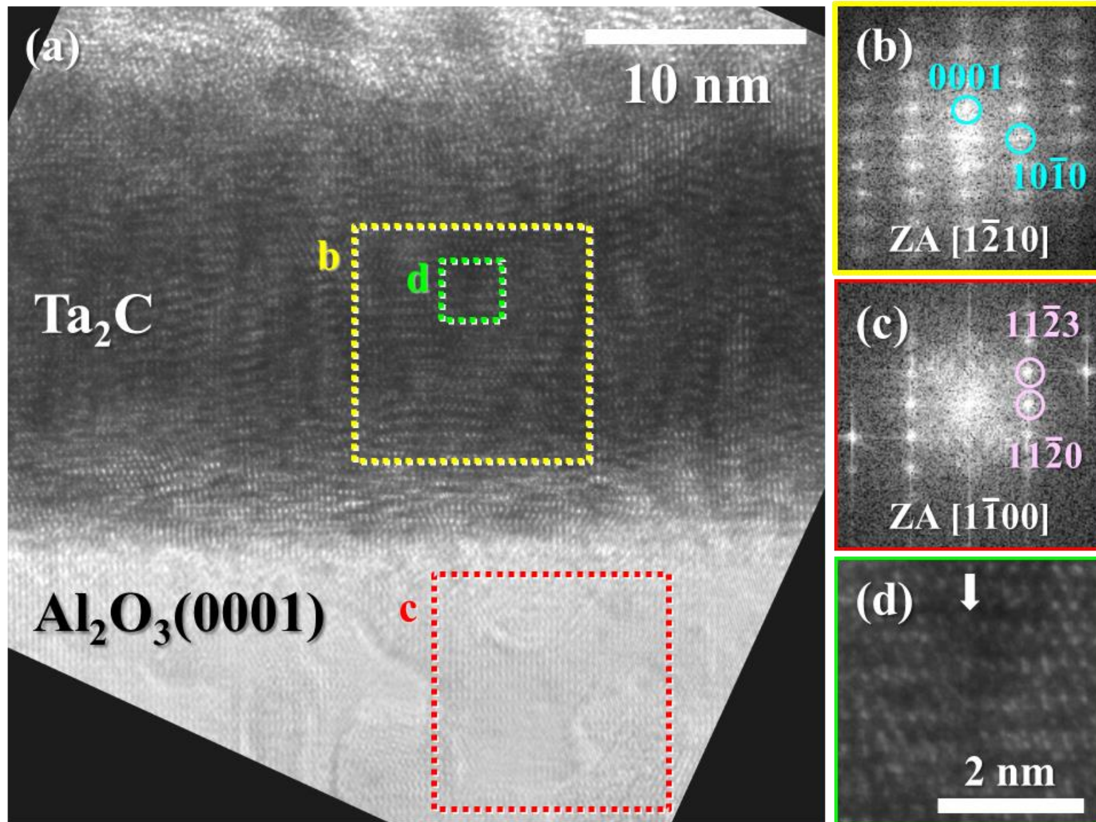

Figure 4.4: (a) Representative XTEM image of the $Ta_2C/Al_2O_3(0001)$ film deposited at T_s = 1373 K for t = 5 min. (b and c) FTs of (b) yellow (Ta_2C) and (c) red (Al_2O_3) dotted square regions, respectively in (a). In (b) and (c), two of the film and substrate reflections are highlighted, respectively using cyan and purple circles, and ZA refers to zone axis. (d) HRTEM image of the green dotted square labeled **d** in (b). Arrow in (d) shows incoherency in layer stacking.

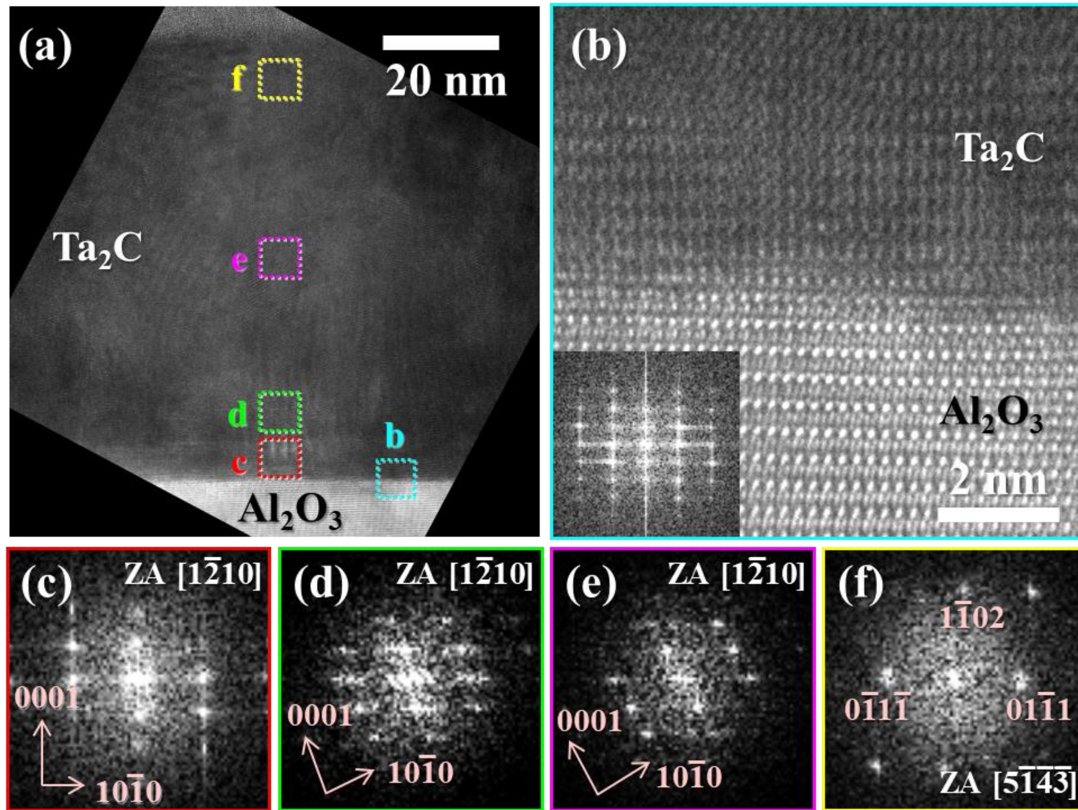

Figure 4.5: (a) Typical XTEM image of the $Ta_2C/Al_2O_3(0001)$ film deposited at T_s = 1373 K for t = 30 min. (b) HRTEM image with inset showing FT of the region bounded by a cyan dotted square labeled b in (a). (c - f) FTs of the (c) red, (d) green, (e) pink, and (f) yellow dotted square areas in (a). In the FTs, ZA refers to zone axis.

CHAPTER 5. Ultrahigh vacuum dc magnetron sputter-deposition of [TaC(111) + $Ta_{n+1}C_n$(000*l*)]/Al_2O_3(0001) thin films

Introduction

Non-cubic tantalum carbides ($Ta_{n+1}C_n$, with n = 1, 2, 3 and 5)[7, 81] are also refractory compounds with exceptionally high melting points (e.g., 3600 K for trigonal α-Ta_2C),[7] high hardnesses (e.g., 12 GPa for α-Ta_2C),[82, 83] high moduli (e.g., 493 GPa for α-Ta_2C),[50, 83-85] and superior mechanical properties[9, 62] with potential applications in aerospace and hard coatings industries.[14] Over the past decade, following the discovery of two-dimensional (2D) layered materials such as graphene,[86] surface-functionalized, atomically-thin layered transition-metal carbides (and other compounds) of the form, $Ta_{n+1}C_n$ with a functional group, generally referred to as "MXenes" have generated considerable interest.[10-13] Experimental studies[58, 83, 87] have revealed differences in mechanical properties of bulk $Ta_{n+1}C_n$ compounds and their composites. *Ab initio* investigations[8] showed elastic moduli and hardnesses of $Ta_{n+1}C_n$ compounds increase monotonically with increasing n. Recent nanomechanical tests conducted on refractory carbides[4, 17, 19, 88] suggest the possibility of leveraging anisotropic room-temperature ductility observed at small length scales to create potentially ultra-tough carbides, for example, as in thin films. Given the seemingly vast application potential of the family of carbides, and since their properties and hence functionalities depend sensitively on the carbon concentrations, it is necessary to develop methods for the synthesis of carbides and their composites with desired phases, compositions, and orientation.

To-date, Ta-C thin films have been grown, with the intent of obtaining B1-structured TaC, using a variety of methods, including but not limited to evaporation,[20] pulsed laser ablation,[15, 21] chemical vapor deposition,[22] and magnetron sputter-deposition.[14, 23, 35, 42-44, 69] Experimental observation of $Ta_{n+1}C_n$ phases in thin films has been limited to one compound, Ta_2C. Lasfargues

et al.[44] reported the presence of α-Ta_2C phase in Ta–C/Si(001) films deposited via sputtering of a nearly stoichiometric TaC target in Ar gas discharges. Tanaka *et al.*[35] demonstrated tunability of Ta-C phases, from B1-TaC to pure α-Ta_2C, in Ta-C/MgO(001) thin films deposited via sputtering of TaC target using ultra-low partial pressures (0.0025 to 2.5% of total pressure) of ethylene (C_2H_4) gas. Recently, Tanaka *et al.*[89] investigated the effect of T_s and deposition time on the 0001-texture evolution in sputter-deposited α-Ta_2C/Al_2O_3(0001) layers. Both these studies revealed that with the appropriate choice of deposition parameters one can, in principle, deposit cubic-TaC and/or layered $Ta_{n+1}C_n$ phases of desired composition, structure, and hence functionality. Achieving this goal, however, requires detailed knowledge of the role of sputtering parameters on the microstructural and compositional evolution of sputter-deposited Ta-C layers. Here, I focus on identifying the growth parameters controlling the phases in reactively sputter-deposited Ta-C thin films on Al_2O_3(0001) substrates.

In this chapter, I present results from microstructural characterization of Ta-C/Al_2O_3(0001) thin films grown via UHV dc magnetron sputtering of a TaC target in 5 mTorr Ar + C_2H_4 gas mixtures with C_2H_4 partial pressures $p_c = 5.0 \times 10^{-5}$ Torr (1% of total pressure) and 5.0×10^{-6} Torr (0.1% of total pressure) at T_s = 1123 K and 1273 K. XRD, SEM, and TEM characterizations are carried out to reveal the phase, orientation, morphology, and microstructure of the as-deposited layers. We obtain rough films with p_c-dependent morphologies: strongly facetted at lower p_c and highly irregular features at higher p_c. XRD data suggests that the films grown using higher p_c (= 1% of total pressure) are primarily 111-oriented B1-TaC. XRD and TEM characterization reveal that the layers deposited with lower p_c (= 0.1% of total pressure) are composed of a two-phase mixture of B1-TaC(111) and rhombohedral-Ta_3C_2(0001). Interestingly, in the layer grown at T_s = 1123 K, both these phases are oriented out-of-plane and in-plane with

respect to the $Al_2O_3(0001)$ substrate as: $(111)_{TaC} \parallel (0001)_{Al_2O_3}$, $[\bar{2}11]_{TaC} \parallel [11\bar{2}0]_{Al_2O_3}$ and $(111)_{TaC} \parallel (0001)_{Al_2O_3}$, $[\bar{1}\bar{1}2]_{TaC} \parallel [11\bar{2}0]_{Al_2O_3}$ and $(0001)_{Ta_3C_2} \parallel (0001)_{Al_2O_3}$, $[10\bar{1}0]_{Ta_3C_2} \parallel [11\bar{2}0]_{Al_2O_3}$.

Results and discussion

Figure 5.1 shows representative SEM images of the Ta-C/$Al_2O_3(0001)$ layers sputter-deposited using p_c = (a-d) 5.0×10^{-6} Torr and (e-h) 5.0×10^{-5} Torr at T_s = (a, b, e, and f) 1273 K and (c, d, g, and h) 1123 K. Lower magnification SEM images (a and c) obtained from the thin films grown using $p_c = 5.0 \times 10^{-6}$ Torr reveal qualitatively similar morphologies over micrometer length scales even though T_s is different: 1273 K and 1123 K for samples in (a) and (c), respectively. Higher magnification SEM images (b and d) of these two samples show pyramidal facetted structures, suggesting that T_s has little influence on the surface morphology. In comparison, the samples deposited with higher $p_c = 5.0 \times 10^{-5}$ Torr exhibit T_s-dependent morphologies: relatively smoother and homogenous surface features at T_s = 1273 K [Figs. 5.1(e) and (f)] and more irregular and non-uniform size features at lower T_s = 1123 K, see Figs. 5.1(g) and (h).

Figure 5.2(a) shows typical 2θ-ω XRD scans obtained from the same set of Ta-C/$Al_2O_3(0001)$ thin films shown in Fig. 5.1. In the data, we observe Al_2O_3 000l, l = 3, 6, 9, and 12, reflections at 2θ = 21.50°, 41.68°, 64.54°, and 90.76°, respectively, characteristic of corundum-structured $Al_2O_3(0001)$ substrate. Note that the 0003 and 0009 reflections are forbidden, but have been observed in XRD scans, likely due to defects in the Al_2O_3 single crystal.[74, 75] The intensities in each of the curves are normalized with respect to the highest intensity peak due to Al_2O_3 00012 reflection so as to facilitate direct comparison of the XRD data across the samples. XRD scans of all but one sample (deposited at T_s = 1123 K with p_c = 5.0

$\times$ 10^{-6} Torr) show two distinct peaks at 2θ = 34.75 ± 0.02° and 73.54 ± 0.03°, which I identify as 111 and 222 reflections, respectively of B1-TaC,[45] indicative of the growth of 111-oriented B1-TaC films. I note that each of these film peaks is broad, spanning a few degrees, and the presence of weaker intensity peaks at 2θ values around 36° cannot be ruled out. I show later that there exist secondary phases in, for example, the films deposited at T_s = 1273 K using p_c = 5.0 $\times$ 10^{-6} Torr.

From the measured peak positions of B1-TaC 111 and 222 reflections, I extract lattice constant a = 0.446 nm for all the Ta-C/Al_2O_3(0001) samples except the one deposited at T_s = 1123 K using p_c = 5.0 $\times$ 10^{-6} Torr, for which I measure a = 0.445 nm. These a values are, within the experimental uncertainties, the same as a_o (= 0.4456 nm), the lattice constant of stoichiometric bulk B1-TaC.[45] Furthermore, among all the samples, I measure the highest intensity and smallest full width at half maximum (= 0.37°) of B1-TaC 111 peak in the XRD data of the film grown at T_s = 1273 K using p_c = 5.0 $\times$ 10^{-6} Torr, indicating that these deposition parameters yield primarily B1-TaC(111) thin films with superior crystallinity.

For the Ta-C/Al_2O_3(0001) film deposited at T_s = 1123 K with p_c = 5.0 $\times$ 10^{-6} Torr, I find four distinct peaks, two of which are at 2θ = 34.87° and 73.59°, corresponding to B1-TaC 111 and 222 reflections, respectively. The other two peaks are at 2θ = 36.16° and 76.89°. Among all the Ta-C compounds, I find the following three possible $Ta_{n+1}C_n$ (n = 1, 2, and 3) phases whose XRD 000l' reflections can be observed at similar 2θ values (see Table I): trigonal α-Ta_2C ($P\bar{3}m1$),[76] rhombohedral Ta_3C_2 ($R\bar{3}m$),[8] and rhombohedral ζ-Ta_4C_3 ($R\bar{3}m$).[90] Using the experimentally observed 2θ values (= 36.16° and 76.89°), I calculate the lattice parameters for each of the $Ta_{n+1}C_n$ phases and compare them with the expected c_o values. The data are presented in the last two columns in Table I. I find that the calculated c matches well with the c_o values for

Ta_3C_2 phase, based on which I suggest (and provide supporting evidence below) that it is the most likely phase present in this film.

To understand the development of these secondary phases, I focus on the Ta-C/Al_2O_3(0001) film grown at T_s = 1123 K with $p_c = 5.0 \times 10^{-6}$ Torr. I acquired XRD pole figures presented as polar plots in Figs. 5.2(b), (c), and (d) with 2θ set to 34.84°, 38.08°, and 57.50°, respectively corresponding to B1-TaC 111, Ta_2C $10\bar{1}1$ (or Ta_3C_2 $10\bar{1}5$, see Table I), and Al_2O_3 $11\bar{2}6$ reflections. I would like to point out that the 3-fold symmetric pattern at out-of-plane tilt χ = 38° in Fig. 5.2(b) and 4-fold symmetric set of spots at χ = 20° in Fig. 5.2(d) are measurement artefacts, respectively, due to Al_2O_3 $10\bar{1}4$ reflections (2θ = 35.15°) and Si 222 reflections (2θ = 58.85°) from a miscut Si(100) wafer that is used to mount the samples. In Fig. 5.2(b), the B1-TaC 111 pole figure, we observe an intense peak at the center (χ = 0°) and six-fold symmetric peaks, 60° apart along φ, at χ ≈ 70°. Given that there are four {111} planes in B1-TaC lattice, 111 pole figure of TaC single-crystal would consist of one peak at χ = 0° and three-fold symmetric peaks, 120° apart along φ, at χ = 70.5°, the angle between any two non-parallel 111 planes. The presence of a high-intensity peak at χ = 0° is indicative of highly 111-oriented TaC grains normal to the basal 0001 planes of the Al_2O_3 substrate, i.e. $(111)_{TaC} \parallel (0001)_{Al_2O_3}$. The observation of six-fold symmetric peaks at χ ≈ 70° implies that there are two sets of 111-oriented crystals (twins) oriented in-plane 60° with respect to each other.

The pole figures in both Figs. 5.2(c) and (d) also show six-fold symmetric peaks at χ ≈ 60° and 41 ± 1°, respectively. Among all possible Ta-C compounds, both Ta_2C $10\bar{1}1$ and Ta_3C_2 $01\bar{1}5$ can give rise to six peaks at χ values around 60°, at 61.4° and 58.8°, respectively, provided the crystals are 0001-oriented along the growth direction. That is, $(0001)_{Ta_{n+1}C_n} \parallel (0001)_{Al_2O_3}$, with n = 1 or 2. As I show below, $Ta_{n+1}C_n$ with n = 2 is the most likely phase in these films.

Furthermore, I find that the six-fold symmetric peaks in all the the pole figures in Figs. 5.2(b) - (d) are at the same φ values. That is, both the B1-TaC(111) and the $Ta_{n+1}C_n$(0001) crystals bear the same in-plane orientation with respect to the substrate. Based on these data, I determine the crystallographic relationships between TaC and the Al_2O_3 substrate as: $(111)_{TaC} \parallel (0001)_{Al_2O_3}$, $[\bar{2}11]_{TaC} \parallel [11\bar{2}0]_{Al_2O_3}$ and $(111)_{TaC} \parallel (0001)_{Al_2O_3}$, $[\bar{1}\bar{1}2]_{TaC} \parallel [11\bar{2}0]_{Al_2O_3}$ and between $Ta_{n+1}C_n$ crystals and Al_2O_3 as $(0001)_{Ta_{n+1}C_n} \parallel (0001)_{Al_2O_3}$, $[10\bar{1}0]_{Ta_{n+1}C_n} \parallel [11\bar{2}0]_{Al_2O_3}$.

I now focus on understanding the microstructural evolution in the Ta-C layers. Figure 5.3 shows typical XTEM images obtained along Al_2O_3 $[10\bar{1}0]$ zone axis from Ta-C/Al_2O_3(0001) layer deposited at T_s = 1123 K and $p_c = 5.0 \times 10^{-6}$ Torr. Fig. 5.3(a) is a lower magnification TEM image of the film, which reveals porous microstructure with up to ~ 180-nm-tall columns along different directions and strongly facetted surfaces, consistent with the SEM data in Fig. 5.1(d). From the image, I measure the film thickness as ~ 130 nm, away from the taller columnar features. Fig. 5.3(b) is a higher magnification TEM image of the region bounded by a white-dotted square in Fig. 5.3(a) near the film/substrate interface. In Fig. 5.3(b), we observe domains with layered structure as indicated by white arrows. Figs. 5.3(c) and 5.3(d) are FTs of regions bounded by yellow and cyan dotted squares, respectively in Fig. 5.3(b). From Fig. 5.3(c), I identify the crystal structure within the region as B1-TaC, zone axis as $[\bar{1}10]$, and the crystal orientation, normal to the substrate-film interface, as 111, consistent with the XRD data in Fig. 5.2(a). From a similar FT (not shown) of the Al_2O_3(0001) substrate, I determine the substrate zone axis as Al_2O_3 $[10\bar{1}0]$, i.e. $[1\bar{1}0]_{TaC} \parallel [10\bar{1}0]_{Al_2O_3}$. Fig. 5.3(d) is an FT of the layered structure, which does not correspond to B1-TaC. From the FT, I measure in-plane and out-of-plane spacings, $d_{in\text{-}plane}$ ~ 0.27 nm and $d_{out\text{-}of\text{-}plane}$ ~ 0.76 nm, respectively, using the spots labeled

A and B. The $d_{in-plane}$ is nearly the same as the $(10\bar{1}0)$ interplanar spacings, $d_{10\bar{1}0}$ (≈ 0.27 nm), in trigonal α-Ta_2C,[76] rhombohedral Ta_3C_2,[8] and ζ-Ta_4C_3.[90] While none of the planes in α-Ta_2C lattice are separated by the experimentally measured $d_{out-of-plane}$ (~ 0.76 nm), I find that d_{0003} (≈ 0.75 nm) in Ta_3C_2 and d_{0004} (= 0.75 nm) in ζ-Ta_4C_3 are comparable. However, the structure factor of ζ-Ta_4C_3 0004 reflection is 0, i.e. it is a forbidden reflection,[90] and therefore I rule out ζ-Ta_4C_3 and suggest rhombohedral Ta_3C_2 as the likely phase with lamellar structure giving rise to the observed spot pattern. These results provide additional evidence in support of the XRD data in Fig. 2 suggesting the formation of Ta_3C_2 phase.

Figure 5.4 shows typical XTEM images obtained along Al_2O_3 $[10\bar{1}0]$ zone axis from the Ta-C layers deposited at T_s = 1273 K and p_c = 5.0 × 10^{-6} Torr. Fig. 5.4(a) is a lower magnification TEM image of the film. I find that the microstructure is qualitatively similar to that of the layers deposited at lower T_s = 1123 K [see Fig. 5.3(a)] with multi-directional columnar growth and facetted surfaces. However, the film is relatively smoother and thicker compared to the lower-T_s sample with ~ 224-nm-tall columns and ~ 198-nm-thick away from the columns. Figs. 5.4(b) and 5.4(c) are higher magnification TEM images acquired from areas labeled b and c, respectively in Fig. 5.4(a), near the film/substrate interface. Within the film, we observe B1-TaC grains and lamellar structures. For example, Fig. 5.4(d) shows a HRTEM image and its FT (as inset) of black square region in Fig. 5.4(b). From the image along with the observed spot pattern in the FT, I identify this region as 111-oriented B1-TaC phase. Fig. 5.4(e) is a HRTEM image of the region highlighted by a green square in Fig. 5.4(b), which shows lamellar-like structures parallel to the film/substrate interface. The associated FT [inset in Fig. 5.4(e)] is similar to the FT in Fig. 5.3(d) and corresponds to rhombohedral Ta_3C_2. Fig. 5.4(f) is a HRTEM image of the region bounded by a red square in Fig. 5.4(c). We observe similar lamellar

structures oriented along different directions, indicated by white arrows in Fig. 5.4(f). From the corresponding FT shown as an inset in Fig. 5.4(f), I identify one set of reflections, highlighted by yellow rectangle, due to B1-TaC along with two additional sets of reflections, characteristic of the rhombohedral Ta_3C_2 phase, due to the two lamellae, whose orientations with respect to the TaC lattice are shown by the cyan and pink arrows. From this data, I determine that the lamellar structures are oriented along 111 and $\bar{1}11$ of B1-TaC. The observation of Ta_3C_2 phase in this sample is consistent with the observation of weaker intensity peaks at 2θ around 36° in the XRD scans shown in Fig. 5.2(a).

The observation of $Ta_{n+1}C_n$ phases, Ta_3C_2 in particular, is not common. $Ta_{n+1}C_n$ phases can be considered as C-deficient B1-TaC with ordered stacking faults (SFs) resulting from removal of carbon layers from 111-oriented TaC bilayers (see Fig. 5.5).[78] The observation of the oriented lamellar structure along ⟨111⟩ of B1-TaC phase agrees with this expectation. Compared to B1-TaC, α-Ta_2C, and ζ-Ta_4C_3, the synthesis of Ta_3C_2 phase is rarely reported, e.g. Ref. [91]. *Ab initio* calculations suggest that the enthalpy of formation of Ta_3C_2 ($R\bar{3}m$) phase is slightly higher than both Ta_2C and Ta_4C_3 and this may explain why Ta_3C_2 is not observed experimentally.[8] While my studies suggest the possible existence of Ta_3C_2 phase, additional growth and characterization experiments are necessary to accurately identify the structure and to understand the mechanisms leading to the formation of seemingly metastable Ta_3C_2 structure.

Conclusion

In this chapter, I focus on understanding the microstructural evolution of TaC_x thin film grown on a single crystal Al_2O_3(0001) substrates via UHV magnetron sputter-deposition of a stoichiometric TaC target in Ar/C_2H_4 mixed gas atmosphere (the total pressure is 5 mTorr) with ethylene partial pressure $p_c = 5.0 \times 10^{-5}$ Torr and 5.0×10^{-6} Torr at two substrate temperature T_s

= 1073 K and 1273 K. We obtain the highly 111-oriented B1-TaC films with two types of in-plane orientation rotated for 60° with respect to each other. The two crystallographic orientation with respect to a $Al_2O_3(0001)$ substrate are identified as (a) $[\bar{2}11]_{TaC} \parallel [11\bar{2}0]_{Al_2O_3}$ and (b) $[\bar{2}11]_{TaC} \parallel [2\bar{1}\bar{1}0]_{Al_2O_3}$. The films deposited with $p_c = 5.0 \times 10^{-6}$ Torr exhibit facetted surfaces morphologies while the films deposited with $p_c = 5.0 \times 10^{-6}$ Torr show irregular porous surfaces. The HRTEM images and corresponding FT patterns suggests the existence of nano-lamellar, presumably of rhombohedral Ta_3C_2, oriented to {111} of B1-TaC crystals. I believe that the results on the growth of highly-oriented B1-TaC thin films coupled with nano-lamellar oriented to specific direction provide fundamental understandings to design carbide-based materials with enhanced strength and ductility, which lead to reliable structural components used in extreme environments.

Table

Table 5.1: List of Ta-C structures, rocksalt (B1) TaC, trigonal α-Ta_2C,[76] rhombohedral Ta_3C_2,[8] and rhombohedral ζ-Ta_4C_3,[90] with in-plane and out-of-plane lattice parameters, a_o and c_o, respectively of bulk stoichiometric crystals. Third column shows the strongest intensity *hkil* and 000*l* reflections and the expected XRD peak positions (2Θ), calculated with the same λ (= 0.154056 nm) used in the experiments. Fourth column lists relative intensities (I_{hkil}) expected for those reflections in a powder XRD. Fifth column shows *c* values determined using experimentally-measured 2θ values (= 36.16° and 76.89°), assuming that they correspond to the 000*l* reflections. Sixth column lists percentage differences in *c* with respect to the bulk c_o values.

	a_o (nm) **c_o (nm)**	***hkil*** **[2Θ]**	**I_{hkil}**	***c*** **(nm)** [2θ]	**(c_o-c)/c_o**
α-Ta_2C (P$\bar{3}$m1)	0.310 0.494	$10\bar{1}1$ [38.08°]	100	--	--
		0002 [36.36°]	23.5	0.4964 [36.16°]	-1.2%
		0004 [77.23°]	2.8	0.4955 [76.89°]	-1.0%
Ta_3C_2 (R$\bar{3}$m)	0.314 2.245	$10\bar{1}\bar{5}$ [38.68°]	100	--	--
		0009 [35.97°]	45.4	2.2337 [36.16°]	+0.5%
		00018 [76.28°]	5.8	2.2298 [76.89°]	+0.7%
ζ-Ta_4C_3 (R$\bar{3}$m)	0.312 3.000	$10\bar{1}7$ [39.20°]	100	--	--
		00012 [35.89°]	46.3	2.9782 [36.16°]	+0.7%
		00024 [76.08°]	5.9	2.9731 [76.89°]	+0.9%

Figures

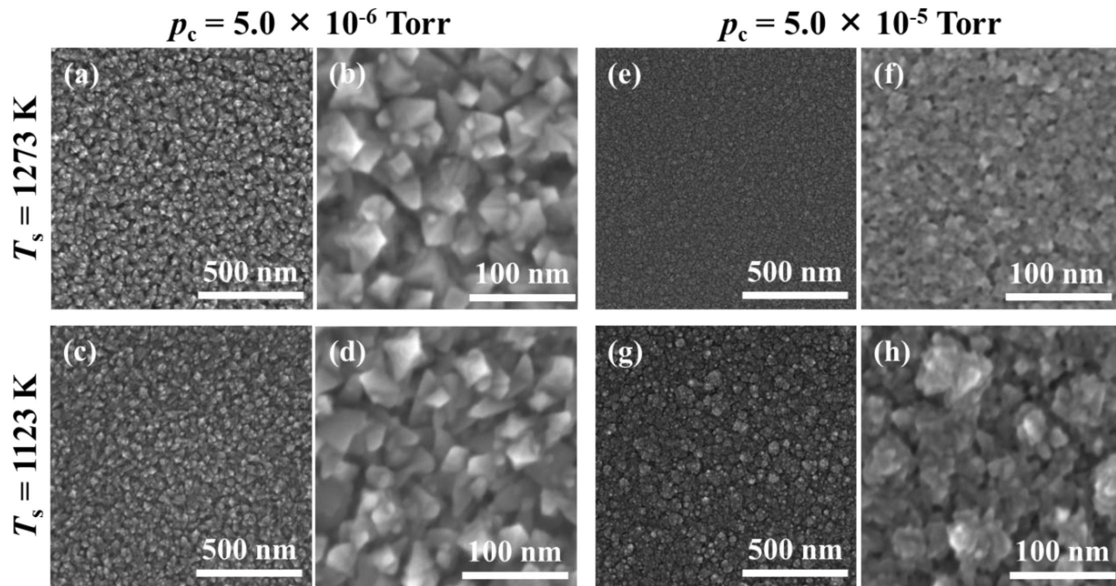

Figure 5.1: Typical SEM images obtained from Ta-C/Al_2O_3(0001) thin films sputter-deposited for 2 h using 5 mTorr total Ar/C_2H_4 gas mixtures with: (a-d) $p_c = 5.0 \times 10^{-6}$ Torr at (a, b) T_s = 1273 K and (c, d) T_s = 1123 K and (e-h) with $p_c = 5.0 \times 10^{-5}$ Torr at (e, f) T_s = 1273 K and (g, h) T_s = 1123 K.

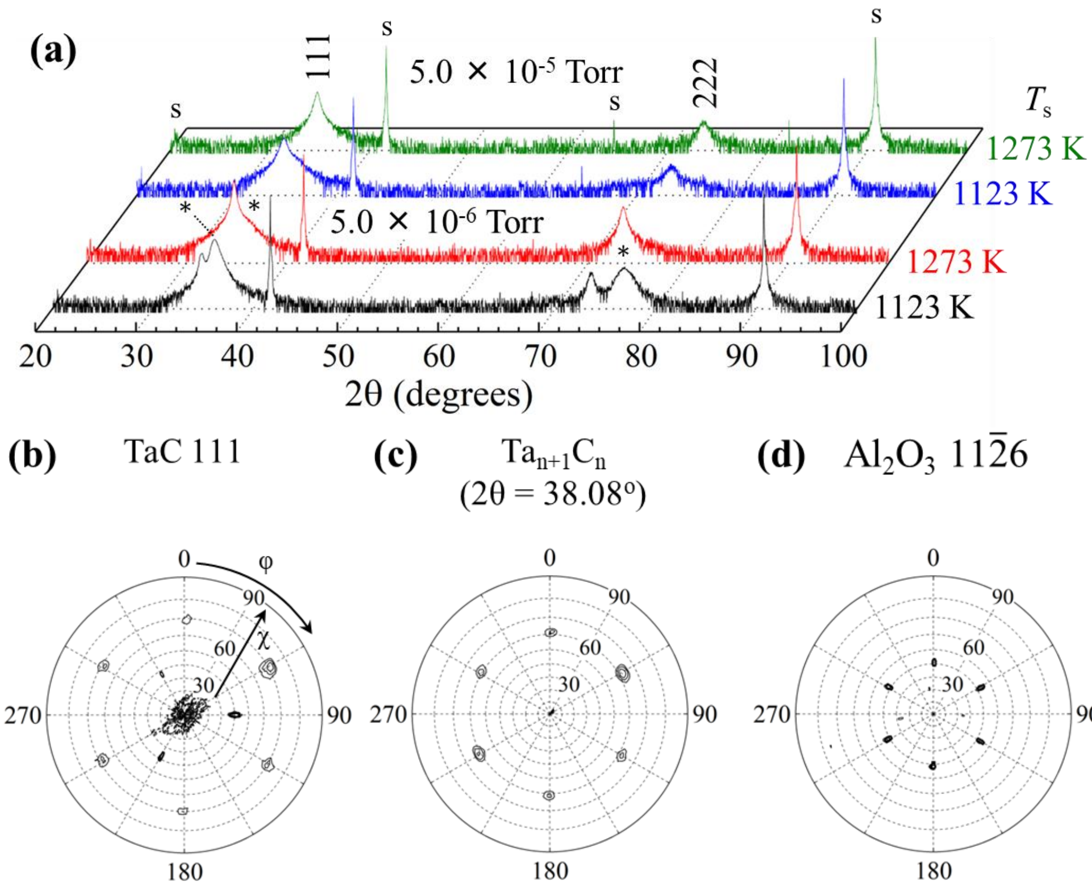

Figure 5.2: (a) Typical 2θ-ω XRD data, with intensities plotted on logarithmic scale, obtained from the same set of Ta-C/Al_2O_3(0001) samples as in Fig. 5.1 grown at T_s = 1123 K and 1273 K with $p_c = 5.0 \times 10^{-5}$ Torr (blue and green curves) and 5.0×10^{-6} Torr (black and red curves). For direct comparison across the samples, intensities in each of the curves are normalized with respect to those of Al_2O_3 00012 reflections. Labels **s** indicate the peaks due to Al_2O_3 000*l* (*l* = 3, 6, 9, and 12) reflections. Peaks due to B1-TaC 111 and 222 reflections are labeled as shown. Peaks with asterisks are likely due to $Ta_{n+1}C_n$ 000*l'* reflections. XRD pole figures of (b) TaC 111, (c) $Ta_{n+1}C_n$ with 2θ = 38.08°, and (d) Al_2O_3 $11\bar{2}6$ reflections obtained from the Ta-C/Al_2O_3(0001) layer sputter-deposited for 2 h with $p_c = 5.0 \times 10^{-6}$ Torr and T_s = 1123 K.

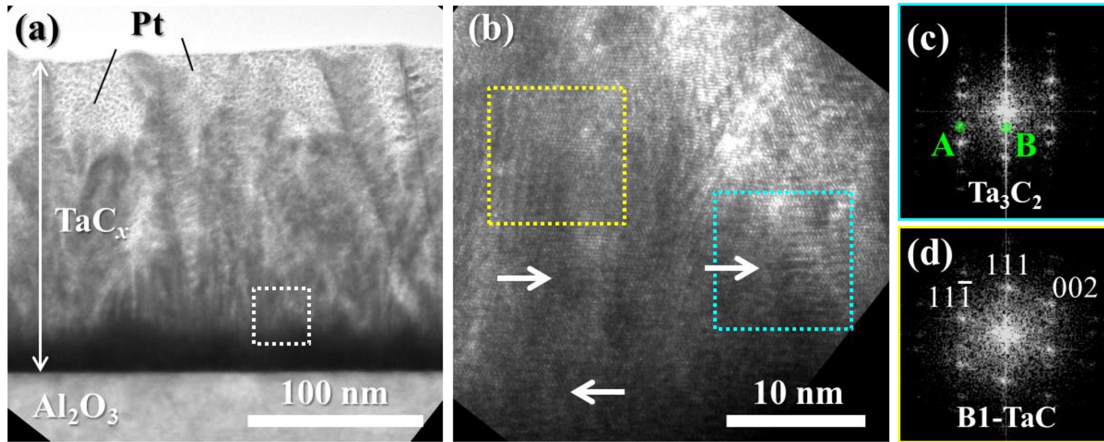

Figure 5.3: (a) Representative XTEM image obtained from Ta-C/Al_2O_3(0001) film deposited at T_s = 1123 K and p_c = 5.0 × 10^{-6} Torr. (b) Higher magnification TEM images of regions bounded by white dotted square in (a). (c and d) FTs of the regions bounded by (c) yellow and (d) cyan dotted squares in (a), respectively. In the FT of (c), indices refer to B1-TaC with zone axis [$\bar{1}$10].

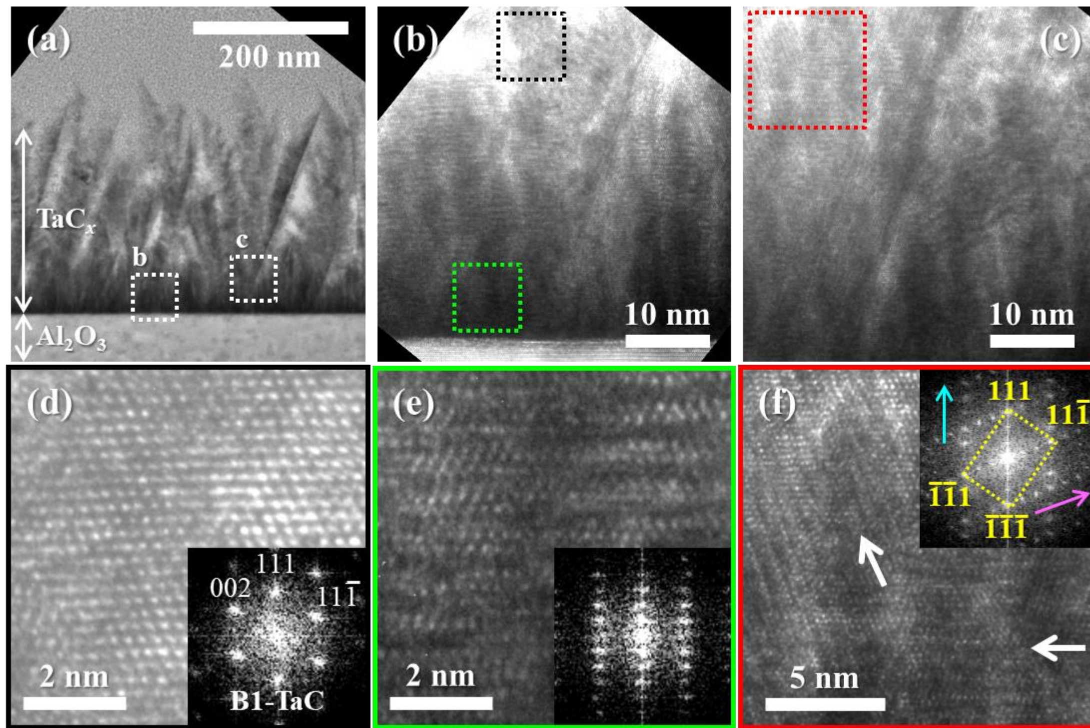

Figure 5.4: (a) Representative XTEM image obtained from Ta-C/Al_2O_3(0001) film deposited at T_s = 1273 K and p_c = 5.0 × 10^{-6} Torr. (b and c) Higher magnification TEM images of regions bounded by dotted squares labeled b and c, respectively in (a). (d-f) HRTEM images of (d) black, (e) green, and (f) red dotted square regions in (b) and (c). White arrows in (f) highlight lamellar structures. Insets in (d-f) are FTs of the images (d), (e), and (f), respectively. In the FT of (f), yellow indices refer to B1-TaC with zone axis [1$\bar{1}$0]. Pink and cyan arrows indicate orientations of the lamellar structures with respect to B1-TaC 11$\bar{1}$ and 111 reflections, respectively.

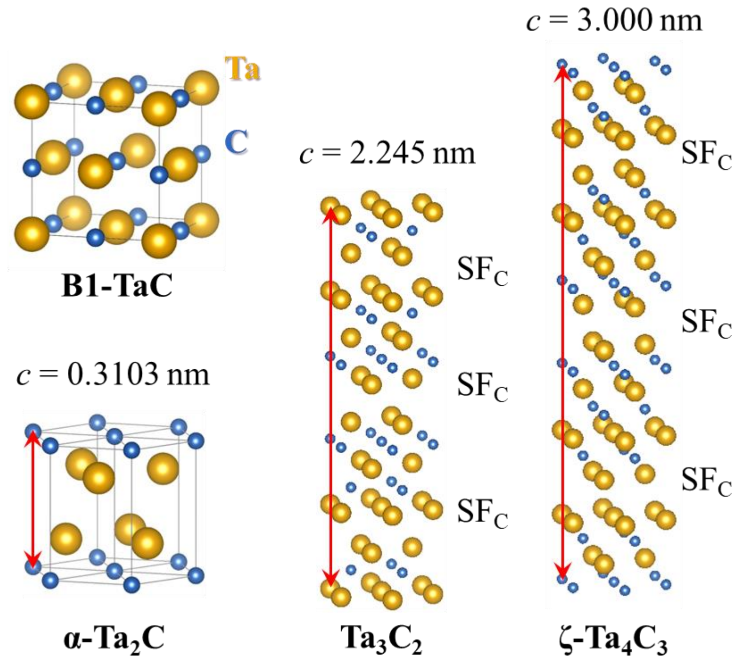

Figure 5.5: Schematics of Ta-C unit cells[56]: B1-TaC, trigonal α-Ta_2C ($P\bar{3}m1$, a = 0.3103 nm, c = 0.4938 nm),[76] rhombohedral Ta_3C_2 ($R\bar{3}m$, a = 0.314 nm, c = 2.245 nm),[8] and rhombohedral ζ-Ta_4C_3 ($R\bar{3}m$, a = 0.3116 nm, c = 3.000 nm).[90] SF_C stands for stacking faults formed via removal of carbon layers.

CHAPTER 6. Van der Waals layer promoted heteroepitaxial growth of α-$Ta_2C/Al_2O_3(0001)$ thin films

Introduction

In the previous chapters, I have shown that epitaxial growth of TaC and Ta_2C thin films can occur on single-crystalline substrates under appropriate growth conditions. However, my studies revealed that the critical thickness of these epitaxial films is limited to a few tens of nanometers, beyond which the films are polycrystalline.[35, 89]

Crystallinity is one of the most critical characteristics that determine the properties and hence performance of materials. Crystalline quality of a solid is typically determined by processing parameters used during its synthesis. For the vapor phase deposition of thin crystalline solid films onto substrates, temperature T and deposition flux are generally considered the two critical parameters determining the crystallinity of the material. Deposition at higher T using lower flux generally yields higher quality crystals, while increasing the flux and decreasing the T result in poorer quality crystals. This is because increasing the temperature leads to enhanced surface adatom mobility together with slower deposition rate increases the adatom diffusion lengths and result in depositing atoms arranging in thermodynamically favorable configurations, i.e. crystalline lattice. The temperatures at which the mobility of adatoms is enhanced is generally discussed in relation to the melting point T_m of the solid,[92] because T_m is a measure of cohesive energy of the solid. For high-melting temperature materials such as TMCs, with a mixture of strong ionic, covalent, and metallic bonds, the homologous temperature (T/T_m) can be quite high (e.g. $0.3T_m = 1275$ K for TaC),[7] indicative of high activation barriers for mass transport. As a result, the temperatures required to enhance the mobility of adatoms are significantly higher than those sufficient for materials with lower melting points. However, increasing the temperature may affect the thermal stability of the material. For example, group 3-

5 semiconductors are made of volatile species (e.g., N, P, As), which decompose upon increasing the temperature. In case of TMCs, C-vacancy concentration increases with T as carbon atoms desorb from the surface. Therefore, one has to rely on alternate approaches to promote crystal growth of such materials. One such approach involves the use of van der Waals (vdW) surfaces as the growth substrates.

In addition to temperature, the mobility of adatoms on surfaces is affected by the adatom-surface interactions. On conventional 3D solid surfaces, the existence of dangling bonds results in strong interaction between adatoms and surface, and results in reduced adatom mobilities. In contrast, on surfaces with vdW bonding, adatoms move relatively freely. Studies[24, 25] conducted nearly three decades ago have shown that layered materials, owing to weak vdW bonding across the layers, can aid in heteroepitaxial growth of layered as well as non-layered materials. Ohuchi *et al.*[24] coined the term 'van der Waals epitaxy' and demonstrated that deposition of a vdW layered material ($NbSe_2$) onto another vdW material (MoS_2) results in heteroepitaxial growth without lattice strain despite a large mismatch of 9%. Since then, several groups have applied vdW epitaxy for the growth of, for example, antimony thin films on single-crystalline graphene;[93] heteroepitaxy of Cu thin films on monolayer graphene covered Al_2O_3(0001) substrate.[94] In the recent years, 2D layered materials have been shown to promote 'remote epitaxy', where the 2D layer present at the substrate-film interface does not hinder the epitaxial registry between the film and the substrate.[26-28] This unique feature of 2D layered materials with vdW bonding can aid the crystal growth of refractory materials such as transition metal carbides. In my studies, I choose hBN as the 2D layered material.

Previous studies have demonstrated the growth of 2D hBN ($P6_3mmc$, a = 0.251 nm and c = 0.666 nm) via CVD primarily on metallic surfaces: Pd(111),[31, 32] Rh(111),[95] Cu(111),[96]

Ru(0001),[97] and Ni(111)[98] using borazine ($B_3N_3H_6$),[31, 32, 95, 96, 99, 100] and ammonium borane (BH_3-NH_3)[99, 101] as the precursors. Bresnehan *et al.*[102] reported the CVD of 2 ~ 25-nm-thick hBN layers on Al_2O_3(0001) using polyborazylene ($B_3N_3H_x$) as the precursor. Chen *et al.* revealed that the hBN layers grown on single-crystalline Al_2O_3(0001) using ammonium borane results in 0002 oriented hBN layer with a thickness of ~ 40 nm at T_s = 1643 K.[103]

In this chapter, I demonstrate the hBN-promoted heteroepitaxial growth of Ta_2C(0001)/Al_2O_3(0001) thin films. First, hBN layers are grown via CVD using borazine on bare Al_2O_3(0001) substrates. Using a combination of *in situ* AES and LEED techniques, I confirm the formation of hBN. Next, I sputter-deposited Ta_2C thin films on hBN-covered Al_2O_3(0001) substrates. I discovered that the Ta_2C layers grown on hBN-covered substrates are significantly more crystalline and oriented than those deposited on bare Al_2O_3(0001). Furthermore, inserting hBN layers at regular intervals during the growth of Ta_2C layers yields better quality thin films than those grown without any interruptions, suggesting that hBN promotes homoepitaxial growth as well.

Results and discussion

First, I focus on the formation hBN layer on Al_2O_3(0001). To this purpose, I carried out *in situ* AES and LEED characterizations of Al_2O_3(0001) substrate surface before and after exposure to borazine vapor. Fig 6.1(a) shows typical AES spectra obtained *in situ* from the same Al_2O_3(0001) substrate before and after 120000 L borazine exposure (with $p_{\text{borazine}} = 2.0 \times 10^{-4}$ Torr for 600 s) at T_s = 1373 K and (b) and (c) show corresponding LEED patterns obtained from the sample surface. In the AES scan obtained prior to borazine CVD step (Fig. 6.1(a)), I find only oxygen (O) peak at 503 eV. The absence of carbon (C) peak at 272 eV is indicative of a clean surface free of organic impurities. A LEED pattern obtained from the bare substrate

surface shows bright spots with hexagonal symmetric pattern. I identify the LEED pattern as Al_2O_3(0001)-(1×1) unreconstructed surface, from which I calculate the sample-screen distance to calibrate LEED patterns acquired at similar incident electron energies. In the AES spectrum obtained from the *same* Al_2O_3(0001) surface after exposure to borazine vapor, we observe boron (B) and nitrogen (N) peaks at 172 eV and 381 eV, respectively, indicative of the presence of these elements on the Al_2O_3 surface after the borazine exposure. LEED pattern obtained from the surface after borazine deposition process reveals hexagonal pattern as shown in Fig. 6.1(c). From the image, I measure inter-columnar spacing of hBN as $d_{10} = 0.217 \pm 0.006$ nm, which is, within experimental uncertainties, in reasonable agreement with the reported value of d-spacing of hBN $(10\bar{1}0)$ $d_{10\bar{1}0} = 0.216$ nm. Based on these results, I conclude that the formation of crystalline hBN layer(s) on Al_2O_3(0001). However, I do not know the exact thickness and the surface coverage of the hBN. I have observed similar LEED and AES data from regions that are ~ 1 mm apart, based on which I expect uniform distribution of hBN islands over millimeter length scales on the sample. Furthermore, based on the LEED patterns, I determined that in my experiments the hBN layers are oriented in-plane with respect to the Al_2O_3(0001) substrate as $(11)_{\mathrm{hBN}} \parallel (21)_{\mathrm{Al_2O_3}}$.

In the following sections, I will compare and contrast the growth of Ta_2C films on bare and hBN-covered Al_2O_3(0001) substrates. In these experiments, all the Ta_2C layers are sputter-deposited in pure 2.0×10^{-2} Torr Ar at $T_s = 1373$ K following the procedure described in Chapter 2 and the hBN layers are grown via CVD using borazine at $T_s = 1373$ K. Figures 6.2(a) and (b) show LEED patterns obtained *in situ* from 6-nm-thick Ta_2C/Al_2O_3(0001) and Ta_2C/hBN/Al_2O_3(0001) samples sputter-deposited for $t = 2$ min., respectively on bare and hBN-covered Al_2O_3(0001) ($p_{\mathrm{borazine}} = 2.0 \times 10^{-4}$ Torr, $t = 300$ s) substrates. I do not observe any LEED spots [see Fig. 6.2(a)] for the Ta_2C film grown on bare Al_2O_3(0001) without hBN. Interestingly,

Ta_2C film grown on hBN-covered $Al_2O_3(0001)$ reveals 6-fold symmetric pattern as seen in Fig. 6.2(b), indicative of highly-ordered surface. From the LEED pattern, I calculate inter-columnar spacing of Ta_2C as $d_{10} = 0.231 \pm 0.006$ nm, which is 13% smaller than the reported value of *d*-spacing of α-Ta_2C $(10\bar{1}0)$ $d_{10\bar{1}0} = 0.269$ nm.

Representative BF XTEM and HAADF STEM images of the $Ta_2C/hBN/Al_2O_3(0001)$ (t = 2 min.) sample are shown in Figs. 6.2(c) and (d), respectively. The image in Fig. 6.2(c) reveals highly ordered atomic columns parallel to the substrate. Inset is a FT obtained from a portion of the image bounded with a cyan dotted square. As seen in previous study on Ta_2C films grown on $Al_2O_3(0001)$ surface,[89] we observe coherency of lattice in the Ta_2C film for the ultra-thin films. From the FTs of the film and the substrate (not shown), I determine the orientation relation as $(0001)_{Ta_2C} \parallel (0001)_{Al_2O_3}$ and $[10\bar{1}0]_{Ta_2C} \parallel [11\bar{2}0]_{Al_2O_3}$. Furthermore, HAADF STEM image in Fig. 6.2(d) reveals uniform contrast across the thickness of the film, suggestive of little compositional variations in the film. Electron energy loss spectra (EELS) and EDS data (not shown) acquired from the sample are inconclusive regarding the exact composition of the film. From the data, I am unable to confirm the presence of hBN layers at the interface. The lack of direct evidence in support of the hBN layer in my TEM characterization could be due to 1) the growth of monolayer-thick hBN islands sporadically distributed on the substrate or 2) decomposition/reaction of the hBN during sputter-deposition.

Fig. 6.2(e) shows a typical 2θ-ω XRD scans obtained from the Ta_2C thin films deposited on hBN-covered and bare $Al_2O_3(0001)$ substrates at $T_s = 1373$ K for $t = 2$ min. In the data, the intensities in each of the curves are normalized with respect to the highest intensity Al_2O_3 0006 peaks labeled s at $2\theta = 41.68^{o}$ and are plotted on logarithmic scale. Inset in Fig. 6.2(e) shows the same set of data with intensities plotted on linear scale. In the scan obtained from the sample

grown on bare Al_2O_3, I observe one peak at $2\theta = 36.46^o$, which I attribute to 0002 reflection of α-Ta_2C ($P\bar{3}m1$, $a_o = 0.3103$ nm, $c_o = 0.4938$ nm).[76] The normalized intensity I_{0002} of the peak (measured as a ratio of the α-Ta_2C 0002 and Al_2O_3 0006 peak intensities) is 4.5×10^{-6}. I would like to note that the same peak is not visible when plotted on linear scale as shown in the inset. In comparison, the XRD data obtained from the Ta_2C/hBN/Al_2O_3(0001) sample shows two significantly higher intensity peaks due to α-Ta_2C 0002 and 0004 reflections at $2\theta = 36.61^o$ and 77.68^o, respectively with $I_{0002} = 1.7 \times 10^{-3}$, over 3× higher than the value measured for the Ta_2C film without hBN. I would like to point out that the peak due to 0002 reflections appears broad with satellite peaks. As seen in the TEM data in Figs. 6.2(c,d), the Ta_2C layer on hBN/Al_2O_3(0001) is single-crystalline and the observed satellite peaks are likely Laue oscillations associated with high-quality layers with abrupt interfaces. For the Ta_2C layers grown on bare and hBN-covered substrates, from the peak positions of 000*l* reflections, I measure out-of-plane lattice constants $c = 0.492$ nm and 0.491 nm, respectively, ~ 0.2% and 0.6% smaller than the literature value.

2θ-ω XRD scans obtained from Ta_2C film deposited on hBN-covered ($p_{borazine} = 1.0 \times 10^{-6}$ Torr, $t = 600$ s) and bare Al_2O_3(0001) surfaces for $t = 5$ min are shown in Fig. 6.2(f). I measure I_{0002} values of 1.7×10^{-3} and 2.9×10^{-2} for the films on bare and hBN-covered substrates. For the film grown on hBN, I find the I_{0002} to be 17-fold higher than for the film grown on bare substrate. Furthermore, we observe fringes around 0002 reflection indicative of abrupt and/or high-quality substrate-film interfaces. XTEM image [not shown] of the sample reveals wavy pattern parallel to the substrate interface. From the FT of the image, I determine that the layer is single-crystalline; however, the spots are relatively more diffuse compared to those seen in the FT of image in Fig. 6.2(c). While the differences in sharpness of the spots in these two FTs are to some

extent due to differences in the image resolutions, I suggest that the thicker film [seen in Fig. 6.2(f)] is not as highly oriented as the thinner film in Fig. 6.2(c). In the following sections, I focus on the crystallinity of thicker films.

Figure 6.3(a) shows typical XRD 2θ-ω scans obtained from three Ta_2C samples, A, B, and C, sputter-deposited for the *same* total time t = 30 min. on hBN-covered Al_2O_3(0001) substrates. Sample A is a nanolaminate made of six sets of Ta_2C/hBN bilayer stacks, with each bilayer grown via sputter-deposition of Ta_2C for t = 5 min. followed by CVD of hBN using borazine with $p_{\text{borazine}} = 1.0 \times 10^{-6}$ Torr for 10 min. I note that the time taken to switch (including evacuation of one gas and filling up the other to the desired pressure) between borazine and Ar is 5 min. That is, the total time elapsed between each Ta_2C deposition is 15 min. Sample B is sputter-deposited without any interruptions for t = 30 min. Sample C is prepared by sputter-depositing Ta_2C six times, with each layer grown for t = 5 min. followed by annealing for 15 min. (the same time as required for the hBN growths in sample A). Fig. 6.3(b) shows schematics of the three samples A, B, and C. The XRD data for sample A shows primarily α-Ta_2C 0002 and 0004 reflections at 2θ = 36.27° and 77.03°, respectively, which suggests that inserting hBN layers at regular intervals yields highly 0001-oriented α-Ta_2C film. We also observe weaker intensity peaks at 2θ around 34° and at ~73.2°, which are likely due to 111 and 222 reflections of B1-TaC.[45] A pole figure of $10\bar{1}1$ reflection (2θ = 38.08°) of α-Ta_2C measured on the Ta_2C/hBN multilayered stack is shown in Fig. 6.3(c). We observe strong 6-fold symmetric patterns at out-of-plane tilts $\chi = 59 \pm 1°$. I also find weak 6-fold symmetric spots at $\chi = 32°$, origin of which is unknown. From the lattice constants, theoretical interplanar angle between (0002) and ($10\bar{1}1$) of a bulk α-Ta_2C is calculated as 61.4°. Comparing the pole figure with the one obtained for Al_2O_3 $11\bar{2}6$ (not shown), I find in plane orientation of Ta_2C with respect to Al_2O_3(0001) as:

$(0001)_{Ta_2C} \parallel (0001)_{Al_2O_3}$ and $[10\bar{1}0]_{Ta_2C} \parallel [11\bar{2}0]_{Al_2O_3}$, which is consistent with my previous observations (see Fig. 4.3) on ultra-thin Ta_2C film grown on $Al_2O_3(0001)$ in Chapter 4. Interestingly, I also observe weak arcs around the intense six spots, suggesting the existence of grains that are rotated from the main orientation angles with respect to χ.

XRD data of sample B reveals multiple peaks at 2θ = 36.30°, 38.35°, 55.72°, 59.62°, 77.11°, and 82.20°, which I attribute to α-Ta_2C 0002, $10\bar{1}1$, 0003, $2\bar{1}\bar{1}0$, 0004, and $20\bar{2}2$ reflections, respectively. For sample C, I find all the above reflections at nearly the same 2θ values and an additional peak at 2θ = 33.28° due to α-Ta_2C $10\bar{1}0$ reflection. That is, the Ta_2C films that are sputter-deposited either continuously for t = 30 min. or intermittently without the insertion of hBN layers are polycrystalline.

These results are interesting given that in all the samples A-C, the $Al_2O_3(0001)$ substrates are covered with hBN. My experiments have shown that Ta_2C grows heteroepitaxially on hBN/$Al_2O_3(0001)$ under these deposition conditions for t up to 20 min., corresponding to thicknesses of 40 nm. That is, the presence of hBN increased the thicknesses up to which highly-oriented Ta_2C layers can be grown. However, there exists a limit to which such growth can occur. I find that the disruption of heteroepitaxial growth occurs at times t between 20 and 30 min. What is surprising, however, is the development of polycrystallinity in Ta_2C films deposited with interruptions (sample C). I would like to point out that in this experiment, the thickness of each Ta_2C layer (deposited for t = 5 min.) is well within the limits of heteroepitaxial growth; the first such layer is deposited on hBN-covered $Al_2O_3(0001)$ and is expected to be epitaxial. That is, Ta_2C films deposited on $Ta_2C(0001)$/hBN/$Al_2O_3(0001)$ are polycrystalline, suggesting that homoepitaxial growth of $Ta_2C(0001)$ is not favored under these particular deposition conditions. However, inserting hBN layers promote the growth of α-$Ta_2C(0001)$ planes, the close-packed

and likely the lowest energy planes. My experiments have shown that highly oriented films are obtained on the hBN-coated $Al_2O_3(0001)$ substrates while polycrystalline and less oriented films are likely to be obtained on bare substrates. I speculate that this is due to a degree of interaction between adatoms and sample surfaces during sputter-deposition. As recently reported,[26] vdW layered materials can reduce the strength of interaction of the 3D materials surfaces while maintaining the epitaxial registry during vapor phase deposition. Inserting hBN layers within the films, e.g. Ta_2C/hBN multilayered stack, can enhance the adatom mobilities on the surface decoupling adatoms from the surface and hence lead to highly-oriented growth of thick (~ 70 nm) films. However, it is still unclear whether the role of hBN is to facilitate remote epitaxy or to promote vdW epitaxy. For the fundamental understanding of the role of hBN, and 2D layered materials in general, on the growth of highly-oriented thin films, further investigation is needed.

Conclusion

In this study, I investigated the effect of hBN on the crystallinity and orientation of sputter-deposited Ta_2C films. hBN layers are first grown via CVD using borazine as the precursor. Using a combination of *in situ* AES and LEED and *ex situ* XRD and TEM, I determined the crystallinity and microstructure of the thin films grown on bare and hBN-covered $Al_2O_3(0001)$ and Ta_2C surfaces. My results show that 0001-oriented growth of Ta_2C is promoted on hBN-covered surfaces for thicknesses considerably greater than those observed in the layers deposited on bare single-crystalline surfaces. I attribute these observations to enhanced surface mobilities during sputter-deposition on hBN-covered surfaces. Based on these observations, I expect that the crystalline quality of thin films can be improved by depositing them on vdW layered materials.

Figures

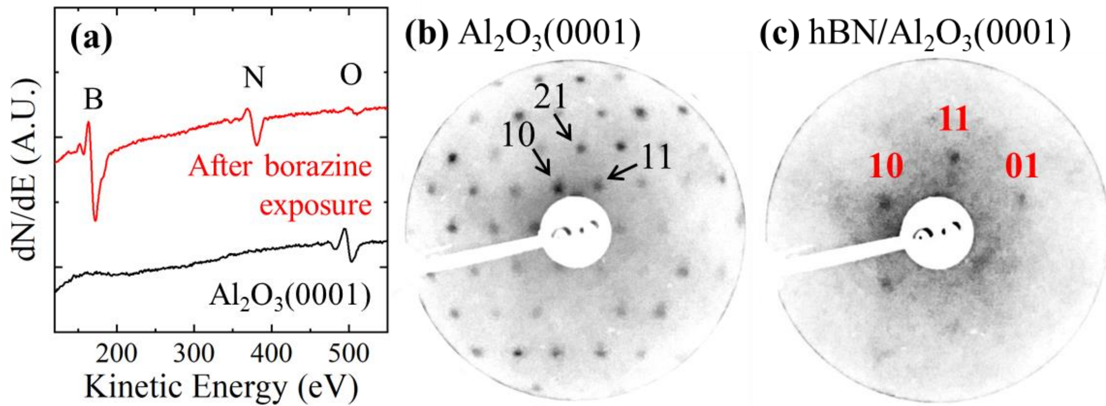

Figure 6.1: (a) *In situ* Auger electron spectra (AES) obtained from a 'clean' $Al_2O_3(0001)$ substrate before (black curve) and after (red curve) exposure to 120000 L of borazine with pressure $p_{borazine} = 2.0 \times 10^{-4}$ Torr for $t = 10$ min. at $T_s = 1373$ K. Auger peaks due to boron (KVV), nitrogen (KVV), and oxygen (KVV) at 172, 381, and 503 eV, respectively, are labeled as B, N, and O. I do not detect Al in our system, which is observed at 66 eV. Corresponding low energy electron diffraction (LEED) patterns obtained *in situ* from (b) the bare $Al_2O_3(0001)$ and (c) after borazine exposure. Incident beam energy E_0 is set to 274 eV and 250 eV for (b) and (c), respectively. Reflections due to unreconstructed $Al_2O_3(0001)$-(1×1) and hBN(0001) are labeled as shown.

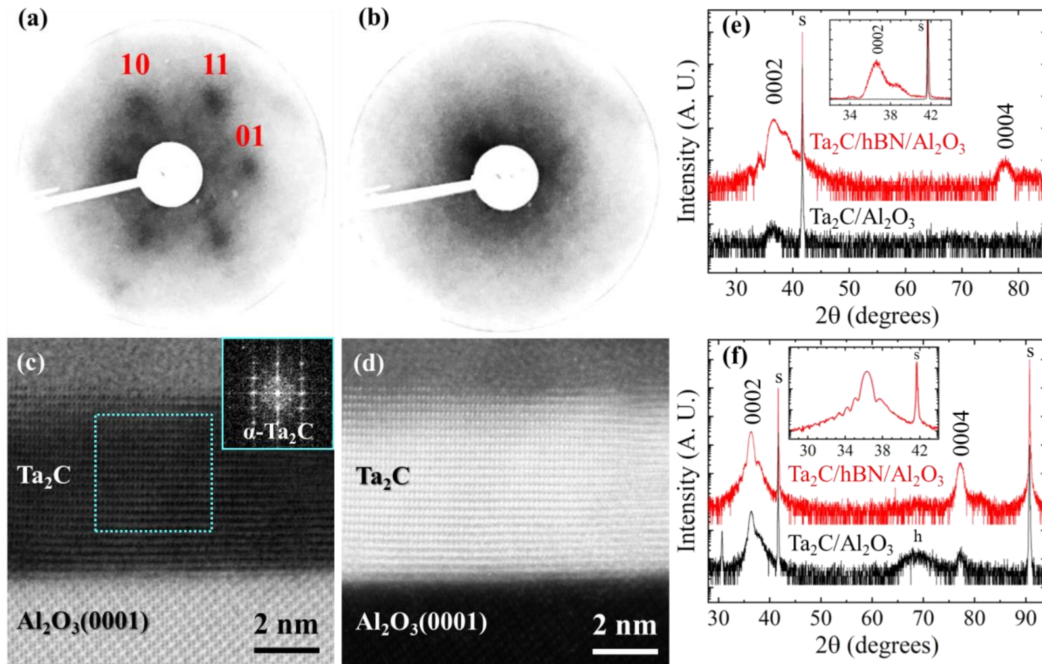

Figure 6.2: (a and b) *In situ* LEED patterns obtained from Ta_2C films sputter-deposited for $t = 2$ min. on (a) on hBN-covered and (b) bare $Al_2O_3(0001)$ substrates at $T_s = 1373$ K. Typical (c) bright field XTEM and (d) HAADF STEM images acquired from the same $Ta_2C/hBN/Al_2O_3(0001)$ sample as in (b). Inset in (c) is an FT of the cyan square region in (c). (e and f) 2θ-ω XRD scans obtained from (red curve) $Ta_2C/hBN/Al_2O_3(0001)$ and (black curve) $Ta_2C/Al_2O_3(0001)$ samples grown for $t =$ (e) 2 min. and (f) 5 min. at $T_s = 1373$ K. Curve intensities are normalized with respect to those of Al_2O_3 0006 reflections and plotted on a logarithmic scale. Inset in (e) shows the same data in (e) plotted with intensities on linear scale. Inset in (f) shows higher-resolution 2θ-ω XRD scan of the $Ta_2C/hBN/Al_2O_3(0001)$ sample acquired with 0.5 mm size slits for 2θ and the detector, 0.05° step size, and 20 s dwell time per step. Laue oscillations around Ta_2C 0002 reflection are visible in this plot. hBN layers for the $t =$ 2 and 5 min. samples are grown with $p_{borazine} = 2.0 \times 10^{-4}$ Torr and 1.0×10^{-6} Torr, respectively for $t = 10$ min. at 1373 K. s indicates peaks due to Al_2O_3 000*l* reflections. The Ta_2C film reflections are labeled as shown.

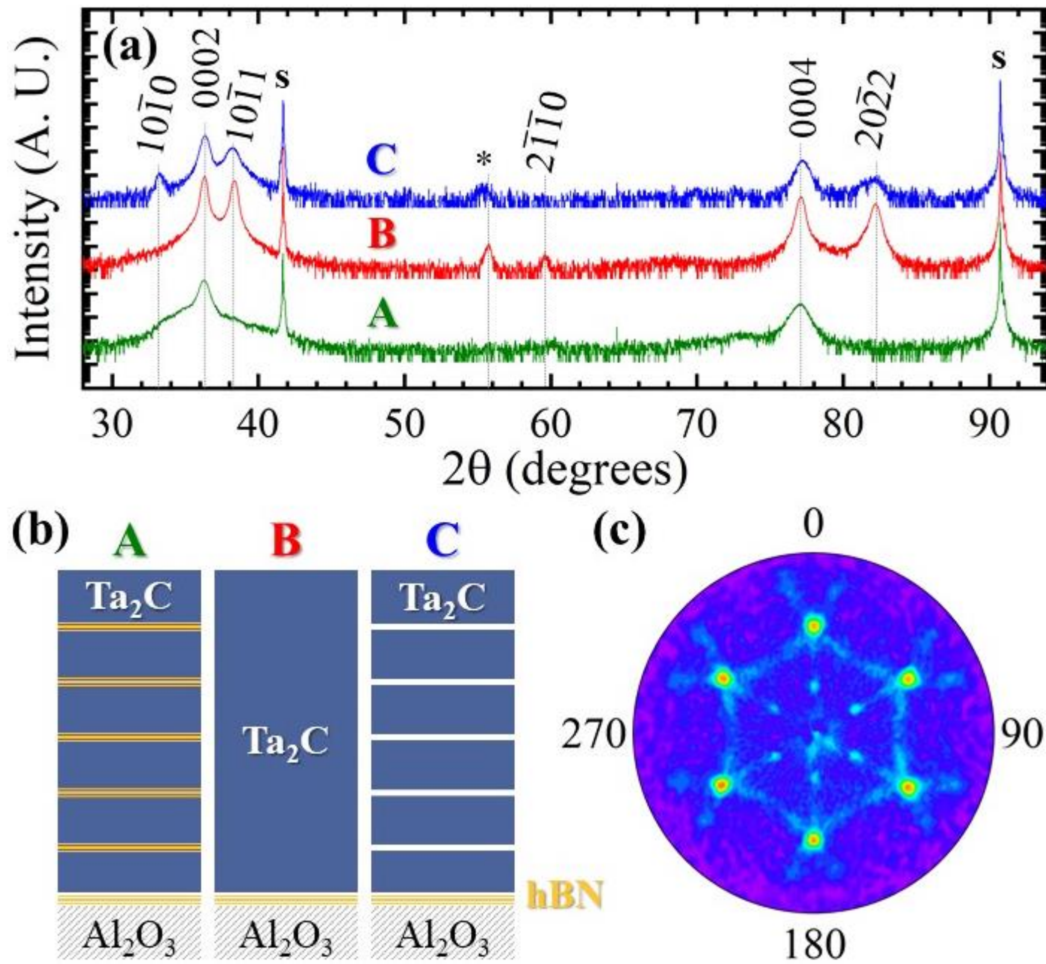

Figure 6.3: (a) XRD 2θ-ω scans, with intensities normalized to that of the Al_2O_3 0006 reflection and plotted on a logarithmic scale, obtained from a (A, green curve) nanolaminate made of 6 Ta_2C/hBN bilayer stacks, (B, red curve) Ta_2C film grown continuously for t = 30 min., and (C, blue curve) Ta_2C film deposited with six 15 min. interruptions, during which the sample is annealed in Ar. All the samples are grown on hBN-covered $Al_2O_3(0001)$. In A and C, each of the 6 Ta_2C layers is sputter-deposited for t = 5 min., with the total time = 30 min., the same as in B. The interruption time in C is the same as the time taken to grow hBN layers in A. The hBN layers are grown with $p_{borazine} = 1.0 \times 10^{-6}$ Torr for t = 10 min. **s** denotes Al_2O_3 0006 and 00012 reflections. Asterisk indicates an unidentified peak, likely due to α-Ta_2C 0003 reflection. (b) Schematics of the A, B, and C. (c) XRD pole figure of Ta_2C $10\bar{1}1$ reflection obtained from A.

Summary and future work

Summary

Ta-C has attracted considerable attention for various potential applications, and its crystallinity and orientation are fundamentally quite important factors to improve the mechanical behavior of these compounds. My dissertation focused on tailoring composition and microstructure of Ta-C films grown via UHV dc magnetron sputtering of TaC target using ultra-low ethylene gas pressures and 2D layered materials. Below, I summarize my most important contributions to the field.

- I investigated the effects of small-amounts of ethylene gas (0.0025 to 2.5% of total pressure) on the compositional and microstructural evolution of Ta-C thin films sputter-deposited on single-crystalline MgO(001) and Al_2O_3(0001) substrates.
    - My results indicate that the sputter-deposited Ta-C film composition and microstructure are highly sensitive to the reactive gas fraction.
    - On MgO(001), I demonstrate tunability of Ta-C phases from trigonal-structured α-Ta_2C to B1-$TaC_{0.76}$ and B1-TaC + free-C two-phase mixture with increasing partial pressures of ethylene from 0 to 2.5% of total pressure. All the films are polycrystalline with C_2H_4 pressure dependent microstructures and surface morphologies. The Ta_2C layers and the TaC + C are relatively smooth while the sub-stoichiometric TaC_x films are porous with highly facetted surfaces. I observed coherent cube-on-cube heteroepitaxy with orientational relationships $(100)_{TaC} \parallel (100)_{MgO}$ and $\langle 010\rangle_{TaC} \parallel \langle 010\rangle_{MgO}$ near the film-substrate interface and the development of 111 twins and polycrystallinity away from

the interface. In contrast, the film deposited using higher C_2H_4 partial pressure (5×10^{-4} Torr) consists of nanoscale TaC crystallites embedded in free carbon.

- On $Al_2O_3(0001)$, I demonstrate tunability of Ta-C phases from α-Ta_2C to B1-TaC + rhombohedral Ta_3C_2 and B1-TaC with increasing ethylene gas fraction from 0 to 1% of the total pressure. In pure Ar discharges, I obtain 0001-textured trigonal-Ta_2C films. In the presence of 0.1% and higher ethylene partial pressures, I observe 111-oriented B1-TaC phase, with ethylene pressure-dependent rough morphologies. With lower ethylene partial pressures (=0.1% total pressure), I observed highly-oriented growth of B1-TaC(111) twins and $Ta_3C_2(0001)$, both of whch are oriented with respect to the $Al_2O_3(0001)$ substrate as: $(111)_{TaC} \parallel (0001)_{Al_2O_3}$, $[\bar{2}11]_{TaC} \parallel [11\bar{2}0]_{Al_2O_3}$ and $(111)_{TaC} \parallel (0001)_{Al_2O_3}$, $[\bar{1}\bar{1}2]_{TaC} \parallel [11\bar{2}0]_{Al_2O_3}$ and $(0001)_{Ta_3C_2} \parallel (0001)_{Al_2O_3}$, $[10\bar{1}0]_{Ta_3C_2} \parallel [11\bar{2}0]_{Al_2O_3}$.

* I investigated the effects of substrate temperature ($1073 \text{ K} \leq T_s \leq 1373 \text{ K}$) and deposition time on microstructural evolution of Ta-C/$Al_2O_3(0001)$ thin films in pure Ar atmospheres.
  - I observed 0001-oriented, α-Ta_2C films that are increasingly smoother and thinner with increasing T_s. The 0001-texture improves with increasing T_s up to 1273 K. At $T_s = 1373$ K, we observe highly coherent 0001-oriented growth with the following orientation relationship: $(0001)_{Ta_2C} \parallel (0001)_{Al_2O_3}$ and $[10\bar{1}0]_{Ta_2C} \parallel [11\bar{2}0]_{Al_2O_3}$ during the early stages of deposition followed by the formation of anti-phase domains and misoriented grains at the later times yielding polycrystalline layers with reduced 0001-texture. I attribute the improvement in film smoothness, crystallinity, and the 0001-texture with increasing T_s to increased surface adatom mobilities and the decrease in film thickness

and the disruption in heteroepitaxial growth to the reduced incorporation of C leading to the formation of structural defects.

- I investigated the role of 2D hBN layers on the crystallinity of sputter-deposited Ta_2C layers.
  - I demonstrated the CVD of hBN using borazine on Al_2O_3(0001) and Ta_2C surfaces. I determined the surface structure and composition using *in situ* AES and LEED techniques. My studies revealed that Ta_2C layers grown on hBN-covered surfaces are highly 0001-oriented compared to those deposited on bare Al_2O_3(0001) substrates and, surprisingly, on Ta_2C(0001) surfaces.

The ability to reduce the reactive gas pressures down to microTorr during sputter-deposition can open up opportunities for designing materials with potentially new properties. I expect that a similar approach can be used to controllably tune the growth characteristics of other reactively deposited thin films. My studies provided new insights into the factors influencing the crystallinity of sputter-deposited Ta-C, and TMC, thin films. I expect that my results will facilitate the growth of high crystalline quality TMCs and other materials. My studies have also opened up the possibility of direct synthesis of MXene-like $TM_{n+1}C_n$ layered structures.

Future work

Based on the results obtained in this research, I propose the following directions for further investigations in the growth and structure of Ta-C/2D materials composites and their applications:

1. Mechanical evaluation on highly oriented Ta-C ultra-thin films and Ta-C/hBN laminated composites, e.g. single-phase TaC, TaC/Ta_2C multilayer stacks, TaC/hBN multilayer

stacks, and TaC:hBN nanocomposites, as a function of thickness and hence determine the film architecture with ultra-high toughness.

2. Investigation of the effect of hBN and other 2D vdW layered materials on the growth of other material systems, e.g. nitrides, sulfides, and high-entropy alloys.

References

1. W. S. Williams, Prog. Solid State Chem. **6**, 57-118 (1971).
2. W. S. Williams, Science **152** (3718), 34-42 (1966).
3. A. Kelly and D. J. Rowcliffe, J. Am. Ceram. Soc. **50** (5), 253-256 (1967).
4. S. Kiani, C. Ratsch, A. M. Minor, J. M. Yang and S. Kodambaka, Scripta Materialia **100**, 13-16 (2015).
5. T. Dinh, H.-P. Phan, T. Kozeki, A. Qamar, T. Namazu, N.-T. Nguyen and D. V. Dao, RSC Advances **5** (128), 106083-106086 (2015).
6. M. Gillinger, T. Knobloch, M. Schneider and U. Schmid, Proceedings of Eurosensors **1** (4) (2017).
7. A. I. Gusev, A. S. Kurlov and V. N. Lipatnikov, J. Solid State Chem. **180** (11), 3234-3246 (2007).
8. X.-X. Yu, C. R. Weinberger and G. B. Thompson, Acta Mater. **80**, 341-349 (2014).
9. A. I. Gusev, A. A. Rempel and A. J. Magerl, *Disorder and Order in Strongly Nonstoichiometric Compounds: Transition Metal Carbides, Nitrides and Oxides*, 2nd ed. (Springer Science and Business Media, Berlin - Heidelberg, 2013).
10. B. Anasori, M. R. Lukatskaya and Y. Gogotsi, Nature Reviews Materials **2** (2), 16098 (2017).
11. S. Wang, Y. L. Du, J. X. Li, Y. Y. Ou and C. Cui, Materials Research Innovations **19** (sup4), S264-S266 (2015).
12. M. Naguib, O. Mashtalir, J. Carle, V. Presser, J. Lu, L. Hultman, Y. Gogotsi and M. W. Barsoum, ACS Nano **6** (2), 1322-1331 (2012).

13. Y. Zhong, X. Xia, F. Shi, J. Zhan, J. Tu and H. J. Fan, Advanced Science **3** (5), 1500286 (2016).

14. G. Håkansson, I. Petrov and J. E. Sundgren, J. Vac. Sci. Technol. A **8** (5), 3769-3778 (1990).

15. R. D. Vispute, S. Hullavarad, A. Luykx, D. Young, S. Dhar, T. Venkatesan, K. A. Jones, T. S. Zheleva, M. Ervin and M. Derenge, Appl. Phys. Lett. **90** (24), 241917 (2007).

16. D. Ham and J. Lee, Energies **2** (4), 873-899 (2009).

17. S. Kiani, K. W. K. Leung, V. Radmilovic, A. M. Minor, J. M. Yang, D. H. Warner and S. Kodambaka, Acta Mater. **80** (0), 400-406 (2014).

18. S. Kiani, C. Ratsch, A. M. Minor, S. Kodambaka and J. M. Yang, Philosophical Magazine **95** (9), 985-997 (2015).

19. S. Kiani, J.-M. Yang and S. Kodambaka, J. Am. Ceram. Soc. **98** (8), 2313-2323 (2015).

20. T. Naiki, M. Ninomiya and M. Ihara, Japan. J. Appl. Phys. **11**, 1106 (1972).

21. R. Teghil, L. D'Alessio, M. Zaccagnino, D. Ferro, V. Marotta and G. D. Maria, Appl. Surf. Sci. **173**, 233-241 (2001).

22. D. Kim, S. M. Jeong, S. G. Yoon, C. H. Woo, J. I. Kim, H.-G. Lee, J. Y. Park and W.-J. Kim, Journal of the Korean Ceramic Society **53** (6), 597-603 (2016).

23. M. Vargas, H. A. Castillo, E. Restrepo-Parra and W. De La Cruz, Appl. Surf. Sci. **279**, 7-12 (2013).

24. F. S. Ohuchi, B. A. Parkinson, K. Ueno and A. Koma, J. Appl. Phys. **68** (5), 2168-2175 (1990).

25. A. Koma, Thin Solid Films **216**, 72-76 (1992).

26. W. Kong, H. Li, K. Qiao, Y. Kim, K. Lee, Y. Nie, D. Lee, T. Osadchy, R. J. Molnar, D. K. Gaskill, R. L. Myers-Ward, K. M. Daniels, Y. Zhang, S. Sundram, Y. Yu, S. H. Bae, S. Rajan, Y. Shao-Horn, K. Cho, A. Ougazzaden, J. C. Grossman and J. Kim, Nat Mater **17** (11), 999-1004 (2018).

27. Y. Kim, S. S. Cruz, K. Lee, B. O. Alawode, C. Choi, Y. Song, J. M. Johnson, C. Heidelberger, W. Kong, S. Choi, K. Qiao, I. Almansouri, E. A. Fitzgerald, J. Kong, A. M. Kolpak, J. Hwang and J. Kim, Nature **544** (7650), 340-343 (2017).

28. J. Kim, C. Bayram, H. Park, C. W. Cheng, C. Dimitrakopoulos, J. A. Ott, K. B. Reuter, S. W. Bedell and D. K. Sadana, Nat Commun **5**, 4836 (2014).

29. J. Fankhauser, M. Sato, D. Yu, A. Ebnonnasir, M. Kobashi, M. S. Goorsky and S. Kodambaka, J. Vac. Sci. Technol. A **34** (5), 050606 (2016).

30. K. Tanaka, J. Fankhauser, H. Zaid, A. Aleman, M. Sato, D. Yu, A. Ebnonnasir, C. Li, M. Kobashi, M. S. Goorsky and S. Kodambaka, Acta Mater. **152**, 34-40 (2018).

31. P. Arias, A. Abdulslam, A. Ebnonnasir, C. V. Ciobanu and S. Kodambaka, ECS Meeting Abstract **MA2018-01**, 839 (2018).

32. P. Arias, A. Abdulslam, A. Ebnonnasir, C. V. Ciobanu and S. Kodambaka, 2D Materials **5** (4) (2018).

33. P. Arias, J. Tesar, A. Kavner, T. Sikola and S. Kodambaka, ACS Nano (2020).

34. A. Aleman, C. Li, H. Zaid, H. Kindlund, J. Fankhauser, S. V. Prikhodko, M. S. Goorsky and S. Kodambaka, J Vac Sci Technol A **36** (3), 030602 (2018).

35. K. Tanaka, A. Aleman, M. E. Liao, Y. Wang, M. S. Goorsky and S. Kodambaka, Thin Solid Films **688**, 137440 (2019).

36. A. Cimino, P. Porta and M. Valigi, J. Am. Ceram. Soc. **49** (3), 152 (1966).

37. M. von Schwarz and O. Summa, Metallwirtschaft, Metallwissenschaft, Metalltechnik **12**, 298 (1933).

38. R. M. Hazen, American Mineralogist **61**, 266-271 (1976).

39. S. Kodambaka, C. Ngo, J. Palisaitis, P. H. Mayrhofer, L. Hultman and P. O. Å. Persson, Appl. Phys. Lett. **102** (16), 161601 (2013).

40. I. Jouanny, J. Palisaitis, C. Ngo, P. H. Mayrhofer, L. Hultman, P. O. Å. Persson and S. Kodambaka, Appl. Phys. Lett. **103** (12), 121601 (2013).

41. H. D. Bhatt, R. Vedula, S. B. Desu and G. C. Fralick, Thin Solid Films **342**, 214-220 (1999).

42. R. D. Evans, J. Y. Howe, J. Bentley, G. L. Doll and J. T. Glass, J. Mater. Res. **20** (09), 2583-2596 (2011).

43. D. Nilsson, F. Svahn, U. Wiklund and S. Hogmark, Wear **254** (11), 1084-1091 (2003).

44. H. Lasfargues, T. Glechner, C. M. Koller, V. Paneta, D. Primetzhofer, S. Kolozsvári, D. Holec, H. Riedl and P. H. Mayrhofer, Surf. Coat. Technol. **309**, 436-444 (2017).

45. A. L. Bowman, Journal of Physical Chemistry **65** (9), 1596-1598 (1961).

46. A. J. Perry, Thin Solid Films **170**, 63-70 (1989).

47. C. M. Kube, AIP Advances **6**, 095209 (2016).

48. H. Högberg, J. Birch, M. P. Johansson, U. Jansson and L. Hultman, Journal of Crystal Growth **219**, 237-244 (2000).

49. J. W. Matthews and A. E. Blakeslee, Journal of Crystal Growth **27**, 118-125 (1974).

50. L. López-de-la-Torre, B. Winkler, J. Schreuer, K. Knorr and M. Avalos-Borja, Solid State Communications **134** (4), 245-250 (2005).

51. M. Dynna and A. Marty, Acta Mater. **46** (4), 1087-1101 (1998).

52. D. Lahiri, V. Singh, G. R. Rodrigues, T. M. H. Costa, M. R. Gallas, S. R. Bakshi, S. Seal and A. Agarwal, Acta Mater. **61** (11), 4001-4009 (2013).

53. H. W. Werner and N. Warmoltz, Surf. Sci. **57**, 706-714 (1976).

54. O. Y. Khyzhun, Journal of Alloys and Compounds **259**, 47-58 (1997).

55. J. Neidhardt, S. Mráz, J. M. Schneider, E. Strub, W. Bohne, B. Liedke, W. Möller and C. Mitterer, J. Appl. Phys. **104** (6) (2008).

56. K. Momma and F. Izumi, J. Appl. Crystallogr. **44**, 1272-1276 (2011).

57. A. L. Giorgi, E. G. Szklarz, E. K. Storms and A. L. Bowman, Phys. Rev. **129** (4), 1524-1525 (1963).

58. N. De Leon, B. Wang, C. R. Weinberger, L. E. Matson and G. B. Thompson, Acta Mater. **61** (11), 3905-3913 (2013).

59. M. Desmaison-Brut, N. Alexandre and J. Desmaison, J. Euro. Ceram. Soc. **17**, 1325-1334 (1997).

60. O. Y. Khyzhun, Journal of Alloys and Compounds **259** (1-2), 47-58 (1997).

61. N. Alexandre, M. Desmaison-Brut, F. Valin and M. Boncoeur, Key Engineering Materials **132-136**, 868-871 (1997).

62. D. J. Rowcliffe and G. E. Hollox, J. Mat. Sci. **6**, 1261-1269 (1971).

63. N. De Leon, X. X. Yu, H. Yu, C. R. Weinberger and G. B. Thompson, Phys. Rev. Lett. **114** (16), 165502 (2015).

64. A. I. Gusev, Journal of Experimental and Theoretical Physics **109** (3), 417-433 (2009).

65. V. N. Lipatnikov and A. I. Gusev, Physics of the Solid State **48** (9), 1634-1645 (2006).

66. N. De Leon, B. Wang, C. Weinberger and G. Thompson, Microscopy and Microanalysis **17** (S2), 1898-1899 (2011).

67. B. Wang, N. De Leon, C. R. Weinberger and G. B. Thompson, Acta Mater. **61** (11), 3914-3922 (2013).

68. Y. Z. Tuleushev, V. N. Volodin, E. A. Zhakanbaev and B. Alimzhan, The Physics of Metals and Metallography **117** (8), 789-794 (2016).

69. H. Riedl, T. Glechner, T. Wojcik, N. Koutná, S. Kolozsvári, V. Paneta, D. Holec, D. Primetzhofer and P. H. Mayrhofer, Scripta Materialia **149**, 150-154 (2018).

70. S. Z. Chang, H. Y. Yu, C. Adelmann, A. Delabie, X. P. Wang, S. Van Elshocht, A. Akheyar, L. Nyns, J. Swerts, M. Aoulaiche, C. Kerner, P. Absil, T. Y. Hoffmann and S. Biesemans, IEEE Electron Device Letters **29** (5), 430-433 (2008).

71. E. Simoen, A. Akheyar, E. Rohr, A. Merch and C. Claeys, ECS Trans. **25**, 237-245 (2009).

72. F. Crupi, P. Magnone, E. Simoen, L. Pantisano, G. Giusi, C. Pace and C. Claeys, ECS Trans. **19** (2), 87-99 (2009).

73. B. J. O'Sullivan, G. Pourtois, V. S. Kaushik, T. Schram, J. A. Kittl, L. Pantisano, S. De Gendt and M. Heyns, Appl. Phys. Lett. **91** (3) (2007).

74. A. A. Anderson, R. W. Eason, M. Jelinek, C. Grivas, D. Lane, K. Rogers, L. M. B. Hickey and C. Fotakis, Thin Solid Films **300**, 68-71 (1997).

75. H. Wang, K. Su, S. Huang, D. Huo and W. Tan, Journal of Materials Science: Materials in Electronics **28** (15), 11275-11278 (2017).

76. A. L. Bowman, T. C. Wallace, J. L. Yarnell, R. G. Wenzel and E. K. Storms, Acta Crystallographica **19**, 6 (1965).

77. T. Lee, H. Seo, H. Hwang, B. Howe, S. Kodambaka, J. E. Greene and I. Petrov, Thin Solid Films **518** (18), 5169-5172 (2010).

78. H. Yu, M. Guziewski, G. B. Thompson and C. R. Weinberger, Modelling and Simulation in Materials Science and Engineering **24** (5), 055004 (2016).

79. S. Kodambaka, V. Petrova, A. Vailionis, P. Desjardins, D. G. Cahill, I. Petrov and J. E. Greene, Surface Review and Letters **7** (5-6), 589-593 (2000).

80. S. Kodambaka, N. Israeli, J. Bareno, W. Swiech, K. Ohmori, I. Petrov and J. E. Greene, Surface Science **560** (1-3), 53-62 (2004).

81. X.-X. Yu, C. R. Weinberger and G. B. Thompson, Computational Materials Science **112**, 318-326 (2016).

82. L. E. Toth, *Transition Metal Carbides and Nitrides*. (Academic Press, New York City, New York, 1971).

83. L. Liu, H. Liu, F. Ye, Z. Zhang and Y. Zhou, Ceram. Int. **38** (6), 4707-4713 (2012).

84. H. Holleck, J. Vac. Sci. Technol. A **4** (6), 2661-2669 (1986).

85. H. L. Brown, P. E. Armstrong and C. P. Kempter, J. Chem. Phys. **45** (2), 547-549 (1966).

86. T. Dumitrica, S. Kodambaka and S. Jun, J. Nanophotonics **6**, 064501-064521 (2012).

87. K. Hackett, S. Verhoef, R. A. Cutler and D. K. Shetty, J. Am. Ceram. Soc. **92** (10), 2404-2407 (2009).

88. S. Kiani, C. Ratsch, A. M. Minor, S. Kodambaka and J.-M. Yang, Philos. Mag. **95** (9), 985-997 (2015).

89. K. Tanaka, A. Aleman, H. Zaid, M. E. Liao, K. Hojo, Y. Wang, M. S. Goorsky and S. Kodambaka, To be published (2020).

90. K. Yvon and E. Parthe, Acta Cryst. **B26**, 149 (1970).

91. S. A. Shiryaev, M. V. Atamanov, M. I. Guseva, Y. V. Martynenko, A. V. Mitin, V. S. Mitin and P. G. Moskovkin, Technical Physics **47** (2), 238-243 (2002).

92. J. E. Greene, Critical Reviews in Solid State and Materials Sciences **11** (3), 189-227 (1983).

93. X. Sun, Z. Lu, Y. Xiang, Y. Wang, J. Shi, G. C. Wang, M. A. Washington and T. M. Lu, ACS Nano **12** (6), 6100-6108 (2018).

94. Z. Lu, X. Sun, W. Xie, A. Littlejohn, G. C. Wang, S. Zhang, M. A. Washington and T. M. Lu, Nanotechnology **29** (44), 445702 (2018).

95. G. Dong, E. B. Fourre, F. C. Tabak and J. W. Frenken, Phys Rev Lett **104** (9), 096102 (2010).

96. S. Joshi, D. Ecija, R. Koitz, M. Iannuzzi, A. P. Seitsonen, J. Hutter, H. Sachdev, S. Vijayaraghavan, F. Bischoff, K. Seufert, J. V. Barth and W. Auwarter, Nano Lett **12** (11), 5821-5828 (2012).

97. Q. Zhang, Y. Chen, C. Zhang, C. R. Pan, M. Y. Chou, C. Zeng and C. K. Shih, Nat Commun **7**, 13843 (2016).

98. A. Nagashima, N. Tejima, Y. Gamou, T. Kawai and C. Oshima, Phys Rev B Condens Matter **51** (7), 4606-4613 (1995).

99. K. Zhang, Y. Feng, F. Wang, Z. Yang and J. Wang, Journal of Materials Chemistry C **5** (46), 11992-12022 (2017).

100. M. T. Paffett, R. J. Simonson, P. Papin and R. T. Paine, Surf. Sci. **232**, 286-296 (1990).

101. Q. Wu, W. Wongwiriyapan, J.-H. Park, S. Park, S. J. Jung, T. Jeong, S. Lee, Y. H. Lee and Y. J. Song, Curr. Appl. Phys. **16** (9), 1175-1191 (2016).

102. M. S. Bresnehan, M. J. Hollander, M. Wetherington, K. Wang, T. Miyagi, G. Pastir, D. W. Snyder, J. J. Gengler, A. A. Voevodin, W. C. Mitchel and J. A. Robinson, J. Mater. Res. **29** (3), 459-471 (2013).

103. Y. Chen, H. Liang, X. Xia, H. Zhang, J. Shi, Q. Abbas and G. Du, Journal of Materials Science: Materials in Electronics **28** (19), 14341-14347 (2017).